國 立 交 通 大 學

機 械 工 程 學 系

博 士 論 文

有限元素生物力學分析:表面網格最佳化及

納氏漏斗胸手術之力學分析

**Finite element biomechanical analysis: surface mesh optimization
and analysis for Nuss pectus excavatum repair**

研 究 生: 徐振予

指導教授: 陳大潘 教授

中華民國九十六年 十月

有限元素生物力學分析:表面網格最佳化及

納氏漏斗胸手術之力學分析

研究生:徐振予　　　　　　　　　指導教授:陳大潘 教授

摘 要

　　本論文之目的,在於研究有限元素法於生物力學分析上之應用,研究內容包括了表面網格最佳化以及納氏漏斗胸手術之生物力學分析。對於生物力學分析研究而言,建立一個合適之有限元素網格,是一個非常重要的步驟,其中又以表面網格的建立最為重要,一般而言,表面網格乃建立於預先定義之模型表面上,但對於大部分之生物力學分析研究而言,其分析模型通常經由量測或斷層掃描資料建立而成,因此無法利用數學模式完整定義整個模型表面,例如脛骨、脊椎以及胸腔模型等研究,為了改善上述分析模型之表面網格品質,我們提出了一套表面網格最佳化方法,其中包括了三角形網格與四邊形網格之轉換、C^1連續之表面方程式建立,以及微基因演算法表面網格平滑化處理,本方法可應用於模型表面網格之最佳化,而不需預先提供模型之表面方程式,因此可適用於生物力學分析模型之應用。

　　漏斗胸是一項常見的先天性胸廓畸形,其病症為患者之胸骨,以及肋軟骨向患者體內凹陷,而於患者前胸形成漏斗狀之變形。納氏手術為目前常用之漏斗胸微創手術,它的手術方式為,將矯形金屬板植入於漏斗胸患者之胸骨凹陷處,將患者前胸之凹陷處頂高,以達到矯正之目的。在手術過程當中,患者之胸廓會隨著胸骨之頂高而變形,然而,經由該變形所引發之應力,也同時產生並作用於患者胸腔骨骼上。在本論文中,我們利用半自動化方式,建立了五個漏斗胸患者之胸腔模型,並分析它們在經過納氏手術矯正之後,患者胸腔骨架上之應力與應變之分佈情形。根據分析結果發現,患者於手術後,其背部靠近脊椎附近,有大量的應力產生,其中大多集中在第三到第七對肋骨上,這個現象可用來解釋,某些漏斗胸病患,於納氏手術後產生背痛之原因,並且可能與少部分患者,於手術後發生脊柱側彎之原因有關。此外,我們利用有限元素分析結果,建立兩套肺容積估測方法,藉由量測患者胸腔容積之變化,可用來估測肺容積之變化,根據量測結果發現,這五位患者之胸腔容積,分別增加了 2.72%到 8.88%不等的容積。

Finite element biomechanical analysis: surface mesh optimization and analysis for Nuss pectus excavatum repair

Student: Zhen-Yu Hsu   Advisor: Da-Pan Chen

Abstract

The purposes of this thesis are focused on the finite element biomechanical analysis, which contains surface mesh optimization and biomechanical analysis of Nuss pectus excavatum repair. For a biomechanical research, one of the significant problems is to create an appropriate finite element volume mesh and the surface mesh generation plays a crucial role in finite element volume mesh generation. Usually surface meshing methods in three dimensions generate meshes relying on prescribed patch interpolation. For some biomechanical researches, the analyzed models, which were usually reconstructed based on measured data or computer tomography scan data, do not have well defined surface function, such as tibia, spine and rib cage models. In order to improve the surface mesh quality of the reconstructed geometrical models, an approach of surface meshing optimization procedure is developed, which consists of a conversion scheme for primary triangular and quadrilateral surface meshes, a C^1 continuous surface function reconstruction and a micro-genetic algorithm (MGA) mesh smoothing procedure. This procedure performs surface mesh optimization without pre-defined surface function. The practical cases are given to demonstrate its successful performance and its versatility.

Pectus excavatum (PE) is one of the commonly found congenital chest wall deformity. It is characterized by depression of the sternum and the lower costal cartilages, producing a concave appearance to the anterior chest wall. The Nuss procedure is a minimal invasion technique that corrects pectus excavatum by inserting a pre-bent bar under the depressed sternum to elevate the sternum. After the Nuss procedure, the chest wall is deformed with the raised sternum and a reasonable amount of stress is induced on the chest wall. In this thesis, five patient-specific finite element models were generated to analyze the stress and the strain distributions induced on the chest wall after the Nuss procedure. The finite element models were reconstructed by applying a semiautomatic procedure based on patients' computer tomography slices. The simulation results show that there are greater stresses occurred over the back and concentrated on the third through seventh ribs bilaterally, near the vertebral

column. These phenomena might explain back pain on some patients after insertion of pectus bar and sporadically reported thoracic scoliosis after Nuss procedure. Moreover, we developed two thoracic volume measurement procedures to estimate the thoracic volume change of postoperative PE patients. The thoracic volume measurement procedure was performed based on the finite element analysis results and the increase of lung volume is estimated by measuring the increase of thoracic volume. The estimated results shown that the thoracic volume is increased about 2.72% to 8.88%.

致謝

Table of contents

List of tables

List of figures

Chapter 1. Introduction

1.1 Overview

Finite element analysis (FEA) is a popular numerical method which is widely used in science and engineering. In a finite element biomechanical analysis, the structural system is first modeled by a set of appropriate subdivisions called elements and then calculated with assigned material properties and applied boundary conditions. The FEA provides a convenient way to investigate the biological phenomena of an object without practical experiment. In this thesis, we employ the finite element analysis to perform the biomechanical analysis of pectus excavatum (PE) patients after a Nuss procedure.

It is well known that a quality mesh is imperative to enhance the accuracy of a finite element simulation. In engineering practice, meshes can be generated on the boundary and/or in the interior of the object, which correspond to surface meshing and volume meshing, respectively. Usually, a well defined geometrical model is requested before the mesh generation. The geometrical model can be defined with algebraic form or defined by patches. However, for some biomechanical researches, the geometrical models were reconstructed from measuring data or computer tomography (CT) scan data [1,2], and it was difficult to provide a pre-defined surface function. In this thesis, we present a different approach that surface meshing is on a set of unorganized points in which the surface function is yet to be defined [3].

1.2 Surface mesh optimization

For surface meshing, most existing methods [4] generate the surface mesh based on pre-defined surface functions, either in parametric patches or in algebraic form, by using existing mesh generation schemes such as Delaunay Triangulation [5] or Advancing Front Methods [6]. However, in many real cases, the given data may just be a set of unorganized points, in which its surface function cannot be devised in a usual fashion. It is often encountered in the applications of biomechanics, which require a geometrical reconstruction from a set of sampling points that is extracted from a sequence of scanned images, e.g. histological sections in tomography. An immediate way to generate a surface mesh for this application is to triangulate the given points [7-10]. However, some sets of such sampling

points can be scattered and irregular, and results in locally ill-posed meshes, which may not acceptable for finite element analysis. In this study, a posteriori approach is adopted to tackle this problem: The given points are first triangulated to generate a triangular mesh and/or convert to the quadrilateral mesh and then an additional procedure is introduced to enhance the quality of the mesh. For finite element meshes, the common used procedure for this enhancement is mesh smoothing.

The most popular mesh smoothing method is Laplacian smoothing [11], in which every internal grid node is repositioned at the geometrical center of the adjacent nodes. Generally, for surface mesh smoothing, Laplacian smoothing is first employed on a parametric plane and then maps the result onto the physical surface domain. It is well known that the mapping between a reconstructed surface and its parametric plane for Laplacian smoothing strongly affects the resultant mesh quality. A given unorganized point set is usually lack of geometrical regularity in distribution. It cannot guarantee to form a proper primary mesh for the mapping of the Laplacian smoothing.

Optimization-based mesh smoothing technique is another way to smooth the finite element mesh, in which the new location of node is found by using the optimization algorithms [12-15]. Freitag [12] presented several articles described about the finite element mesh smoothing techniques, which contained smart Laplacian smoothing, optimization-based smoothing and the combination of both, in two-dimensional plane mesh and three-dimensional tetrahedral mesh. For the combination method, the smart Laplacian smoothing is used to adjust every internal node and is followed by the optimization-based algorithm, the steepest decent method [16], in only the poorest-quality elements [12]. The steepest decent method searches an optimal solution by a given initial step along a search direction, which is calculated from the gradients of the object function, i.e. mesh quality measurement. However, the calculating of gradients according to the real coordinates is inconvenient for this application, in which the surface function is yet to be defined. Besides, the search direction may let the nodes to deviate from the original surface.

Garimella et al. [14] presented a surface mesh quality optimization procedure that the nodes are repositioned based on element-based local parametric spaces. They employ the conjugate gradient method [16], whose search direction is estimated by computing the gradients of the mesh quality measurement with respect to the local parametric spaces, to reposition the nodes to enhance the mesh quality. It is beneficial that mesh smoothing based on local parametric spaces can remain the nodes close to the original surface. The calculation of the gradients of object function, which is based on the local parametric spaces and without

the need of surface functions, is suitable for this application. However, two problems will be arisen: (1) the repositioned points are re-allocated on the planes of corresponding elements, that are not projected onto the original surface, and this will affect the geometrical accuracy of model. (2) The gradient search methods as a local search method may encounter local optimum problem.

In this study, we propose an innovation surface mesh smoothing procedures that mesh nodes were repositioned by using the micro-genetic algorithm (MGA) based on local reconstructed surface. The MGA [17-20] is similar to the genetic algorithms (GA) [21,22], which is a global search method that searches optimal solution by employing natural evolution without calculating search direction and step size. The MGA works with small population size and reaches new optimal regions much earlier than the conventional GA implementation [17]. It has been successfully applied to many fields [17-20]. Moreover, in order to ensure the geometrical accuracy of the analytical model, we projected the repositioned nodes onto the original surface based on an interpolation surface function [23], which is reconstructed from the primary triangular elements. The one drawback of our approaches is that the computational cost of MGA is larger than the gradient search methods [16] but it is feasible by applying parallel computation algorithms [24] to accelerate its computational efficiency.
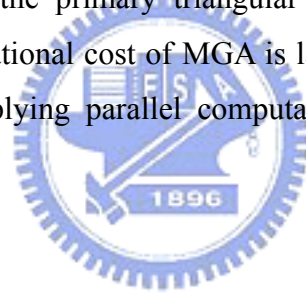
1.3 Pectus excavatum

Pecuts excavatum (PE), also known as sunken or funnel chest, is one of the most commonly congenital chest wall deformity, occurring in approximately 8 per 1,000 live births, with males afflicted 5 times more often than females [25,26]. PE deformities are about 6 times more common than pectus carinatum. Figure 1-1 illustrates a typical appearance of PE deformity in a 7-year-old boy. The cause of this defect is thought to be the excessive growth of the costal cartilage, which produces a concave anterior chest wall [27]. Approximately 40% of PE patients are aware of one or more members of the family constellation who have pectus deformities.

Symptoms are infrequent during early childhood, but become increasingly severe during adolescent years with easy fatigability, dyspnea with mild exertion, decreased endurance, pain in the anterior chest and tachycardia [25]. Scoliosis is one of the coexistent malformations for pestus excavatum patients. The deformations of pectus excavatum not only affect the shape of front chest but also affect the pulmonary and cardiac function. The depressed sternums of PE

patients decrease in the intrathoracic volume and induce the effects on pulmonary and cardiac function. In some serious PE patients, the decreasing intrathoracic volume induces the pressure in the lung and heart, and results in the shortness of breath and increasing the heart rate. The severity of pectus excavatum can be calculated by a pectus index [28], which is calculated by dividing the transverse diameter of the chest by the anterior-posterior diameter (Fig. 1-2). The mean pectus index for normal persons is 2.52, and mean pectus index of patients who underwent PE repair in the large series reported by Haller et al was 4.4 [28].

In 1949, Ravitch presented a technique of pectus excavatum repairing [29]. It is a classic surgical repair of pecuts excavatum, which involves bilateral costal cartilage resection and sternal osteotomy technique. In 1998, a minimal invasive technique for repairing pectus excavatum without costal cartilage resection and sternal osteotomy was presented by Nuss et al. [30]. In this procedure, one pre-bent metal bar (pectus bar) is placed under the depressed sternum through bilateral thoracic incisions and then forcibly turned around to elevate the sternum. Since the bilateral costal cartilage is not resected, the chest wall of PE patients will deform with the raised sternum and suffer from stresses. The generated stresses on the chest wall may be the cause for some complications, such as pain [31] and scoliosis [32]. Until recently, most research focused on improving the Nuss procedure [33,34] and demonstrating the embedded complications [31,35,36]. The analysis of biomechanical effects of the chest wall of the PE patient after a Nuss procedure was rarely mentioned [37]. It is essential, for the cure of pectus excavatum, to understand the effects of the pectus bar implantation. In this study, we developed a finite element analysis (FEA) procedure to analyze the stress and the strain distributions induced on the chest wall after a Nuss procedure.

Force requirement to raise the sternum of pectus excavatum was presented by Fonkalsrud and Reemtsen [38] and Weber et al. [39]. According to their researches, the raising force was measured by a spring scale through an anterior incision during PE repair. However, the Nuss procedure performed PE repair through bilateral thoracic incisions, which were two small openings on the sides of the chest, the forces of pectus bar applied to the chest wall can not be measured directly. Awrejcewicz and Łuczak [37] presented a finite element model of the human rib cage, contains rib, costal cartilage, sternum and Nuss implant, to investigate stress distributions of the human thorax with Nuss implant for an impact load.

Finite element analysis is a versatile technique for engineering simulation. It had been extensively applied to many biomechanical analysis researches of biomedical researches, such as the tibia [40], the femur [41] and the rib cage [37,42]. In the previous works [37,42], the finite element analysis procedures were performed with simplified finite element models.

However, the finite element biomechanical analysis for PE patient is not presented before. In order to ensure the accuracy and to recognize the validity of the FEA results, five patient-specific finite element rib cage models were crested in this study based on individual computer tomography (CT) slices.

Geometrical model reconstruction based on CT slices was commonly used to obtain a biomechanical model [37,40]. However, since the grayscale value of costal cartilage is similar to some of other human tissues, the image of costal cartilage is difficult to be observed form CT slices. In this thesis, a semiautomatic procedure was developed to reconstruct a rib cage model, which was consisted of rib, costal cartilage and sternum. Moreover, according to clinical observation, the lung volumes of PE patients were indeed increased after the Nuss procedure. However, it is difficult to measure the increase of lung volume due to that the PE patients can not receive CT scan after the implant of Nuss procedure. To conquer this problem, we present two thoracic volume measurement procedures to estimate the increase of lung volume with the FEA models. The increase of lung volume is estimated by measuring the variation of intrathoracic volume.

Fig. 1-1 A 7-year-old boy with pectus excavatum.
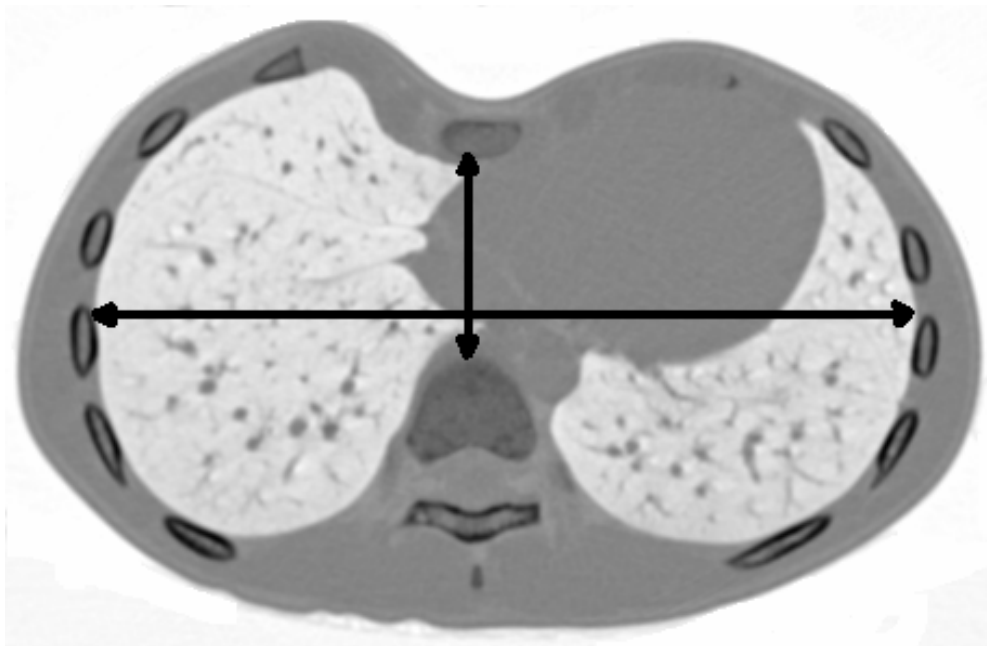
Fig. 1-2 Pectus index.

Chapter 2. Genetic algorithm

2.1 Genetic algorithm

The genetic algorithm is one of the popular evolutionary algorithms. It is a programming technique that mimics natural evolution to solve optimization problem. The GA begins with a set of initial individuals called the population that represent the potential solutions of the given problem. The population is used to represent the chromosomes and the potential solutions are the individuals. During the evolutionary process, the potential solutions were encoded as a bit string to simulate the gene of nature. At the beginning, several strings are created randomly to form an initial population and a fitness function was defined to allow each candidate to be quantitatively evaluated. As Darwin's theory of evolution, the population is evolved generation after generation to search an optimal solution and historical information is then exploited to speculate on new search points with expected performance during the iteration [21]. Fig. 2-1 showed the flowchart of the traditional genetic algorithm.

GA searches an optimal solution based on the mechanics of natural selection and natural gene. Before the GA procedure, several design parameters were created to characterize the optimization problem and a fitness function was defined to evaluate the solution. The potential solutions were created with the design parameters and coded as binary string to form the initial population. Then the GA was performed to search a global optimal solution by using several genetic operators, which were described below.

2.1.1 Coding

In order to perform the GA evolution with computational calculation, the population was coded as binary string, suggested by Holland in his pioneering efforts [43], to simulate the gene of nature. The length of each substring can be determined according to the interval of each design parameter and the solution accuracy. Let a be a interval of design variable and the solution accuracy is 0.001, then the length of each substring can be calculated as fellows

$$2^{nl-1} < a \times 1000 < 2^{nl} \tag{1-1}$$

where *nl* is the length of substring.

2.1.2 Initialization

At the beginning, several strings of individuals were created randomly to form an initial population. The population size is always problem dependent. The usual choice of population size is based on the conception that bigger population relates to better schema processing, lesser chance of premature convergence, and better optimal results [17]. However, the computational loading is increased in proportion to the population size. The general choice of population size for conventional GA can range from 100 to 1000.

2.1.3 Selection

Selection operator is a process of deciding which chromosomes in the current population will pass their solution information to the next generation. For a genetic algorithms optimization process, the selection operator selects not only the currently best chromosomes but also some other chromosomes to avoid a local optimal solution. There are two popular selection strategies, roulette wheel selection and tournament selection [44].

The roulette wheel selection (Fig. 2-2) is the classical and simple selection scheme. As shown in Fig. 2-2, the roulette wheel selection selected chromosomes based on their probability. The probability was estimated as

$$P_{selection} = \frac{Fj}{\sum_{i=1} Fi} \tag{1-2}$$

where Fi is the fitness value of ith individual. For the roulette wheel selection, individuals with high fitness value will be selected more often than less fitness individuals, but it does not guarantee that the fittest member goes through to the next generation.

For tournament selection (Fig. 2-3), a subpopulation of N individuals is chosen randomly from the current population. Then the highest fitness of individual in the subpopulation wins the tournament and becomes the selected individual. The tournament size (N) can be changed to adjust the selection pressure. If the tournament size is larger, weak individuals have a smaller chance to be selected. The benefits of the tournament selection are (1) efficient to

code and (2) easy to adjust the selection pressure.

Moreover, a so called "elitism" process was commonly adopted to select the better individuals to pass to the next generation. The elitism process allows the better information to pass to next generation to get better solutions over times. It is essential, mainly for small population size.

2.1.4 Crossover

Crossover is a principal genetic operator for a genetic algorithm optimization procedure. The selection operator selects several individuals to be the parents and the crossover operator accepts a pair of parents' solutions to generate two new individuals for the next generation population (Fig. 2-4). Many variations of crossover have been developed and the simplest one is one point crossover. As shown in Fig. 2-4(a), a cutting point was randomly selected in the parents' chromosomes and the portion of the chromosomes of parents following the cutting point was changed to form two children. The cutting point can be one or more than one point (Fig. 2-4(b)). The selection of cutting point number is always depended on the optimization problem and population size.
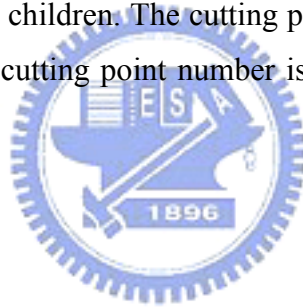
2.1.5 Mutation

Mutation operator is analogous to biological mutation to avoid the loss of some important genes and increase the variation of the individuals. The individuals of new population were generated either directly copied or produced by crossover. In order to ensure that the individuals are not all exactly the same, a mutation operator is adopted to add new information into individuals occasionally. As shown in Fig. 2-5, one gene was selected randomly and flipped (0 becomes 1, 1 become 0).

A very small mutation rate may lead to a premature convergence of the genetic algorithm in a local optimum. A mutation rate that is too high may lead to loss of good solutions. In order to avoid the premature or the loss of good solutions, a fluctuated mutation rate was developed. A very small mutation rate was set in the beginning of optimization procedure to avoid the loss of good information and the mutation rate was increased when the candidate solution was convergenced to an optimal solution to avoid the premature.

2.2 Micro-genetic algorithm

The standard genetic algorithm is successfully applied to many different applications [21,22]. However, one major drawback is that the iterative global searching of the algorithm is time consuming. It will be deteriorating when additional iterations are needed in the smoothing procedure. There are many approaches to tackle this problem. For the genetic algorithm practice, reduction of the population size is an effective way. For conventional GA, the general choice of population size can range from 100 to 1000. This imposes a considerable loading on the computational time. To trade-off, the micro-genetic algorithm [17,20] is particularly adopted to accelerate the convergence of the conventional GA. The MGA is similar to the GA that proceeds with binary coded population and employs the selection and crossover operations to evolve population for generations, but with smaller population size than conventional GA. It had been reported that MGA reaches near optimal regions much earlier than the standard GA does [17]. Fig. 2-6 showed the flowchart of the micro-genetic algorithm.

The micro-genetic algorithm is a small population genetic algorithm. MGA uses a micro-population of five individuals [17]. It is well known that the GA works poorly with small population size due to insufficient information processing, which results in premature convergence to local optimal solutions. For the MGA, the best individual is passed to the new generation to ensure that the good individual is held, and it requires multiple convergences. The best individual of the old is remained and the others are randomly generated after each convergence. This operation is used to add new information and avoid premature convergence, and the mutation rate is set to zero.
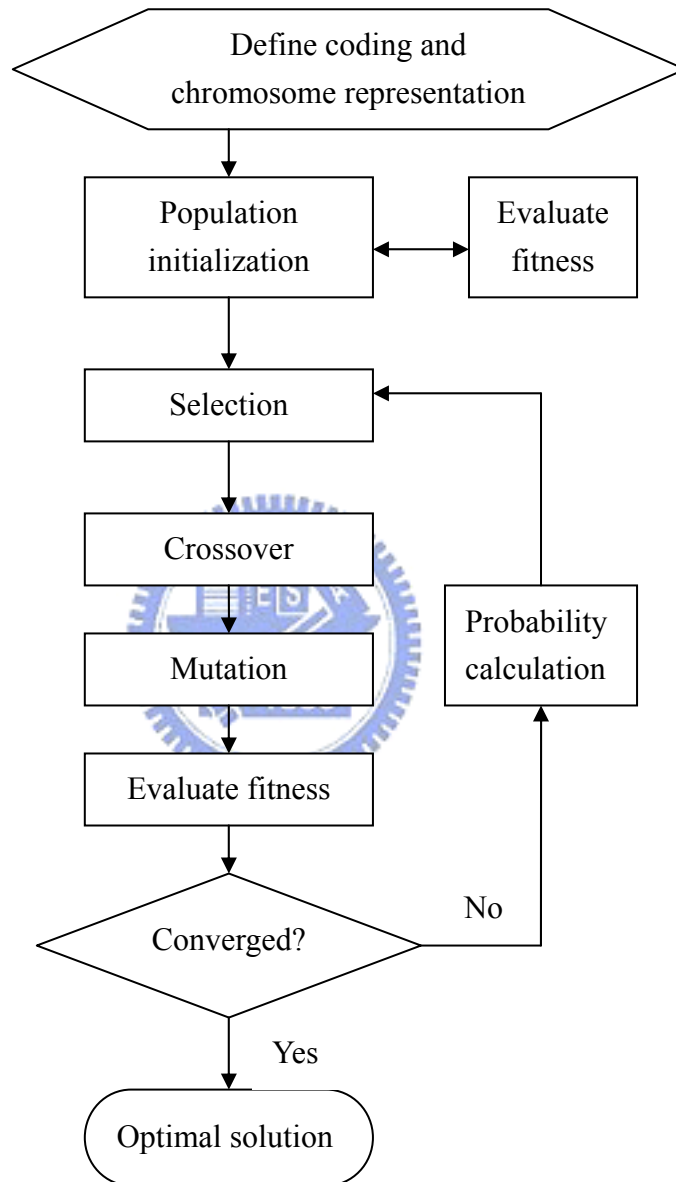
Fig. 2-1 Flowchart of the traditional genetic algorithm.
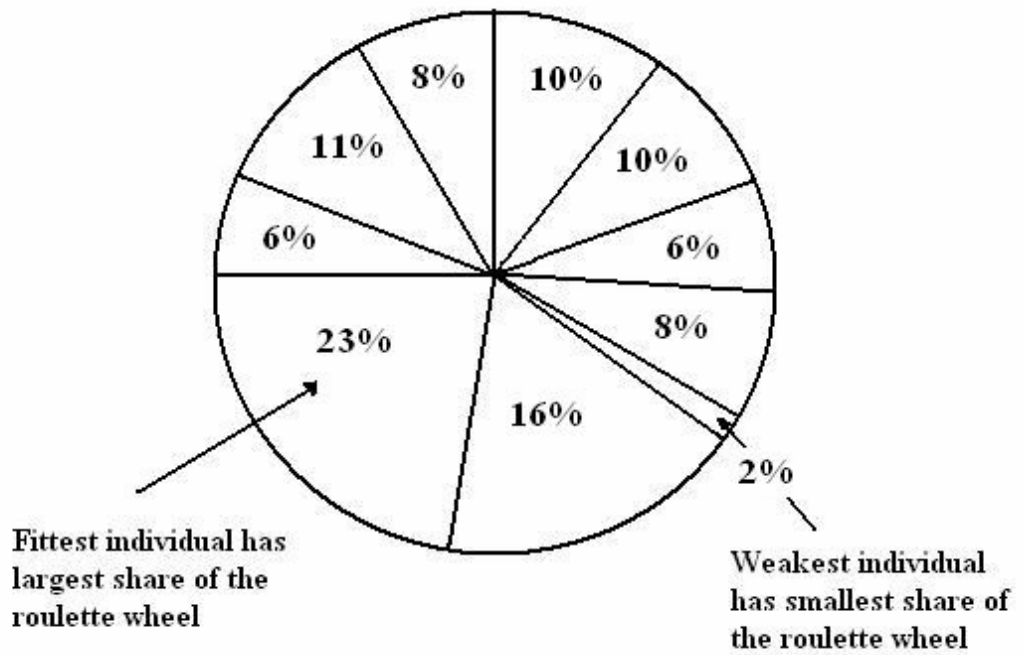
Fig. 2-2 Roulette wheel selection.
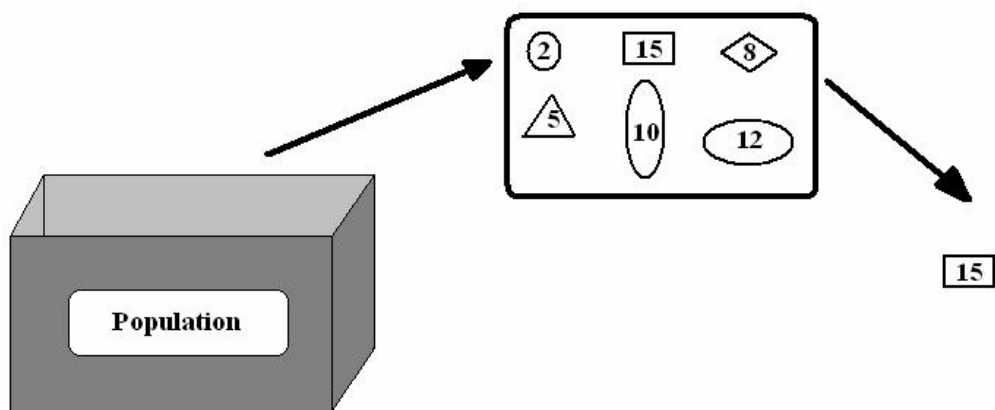
Fig. 2-3 Tournament selection.
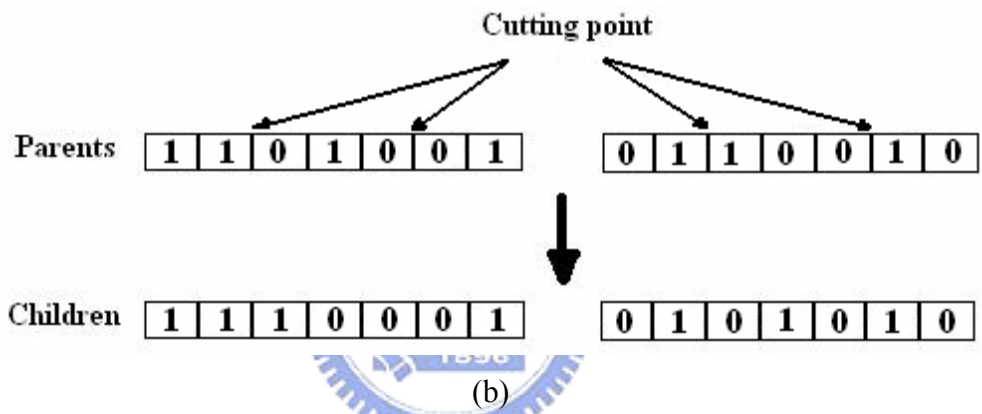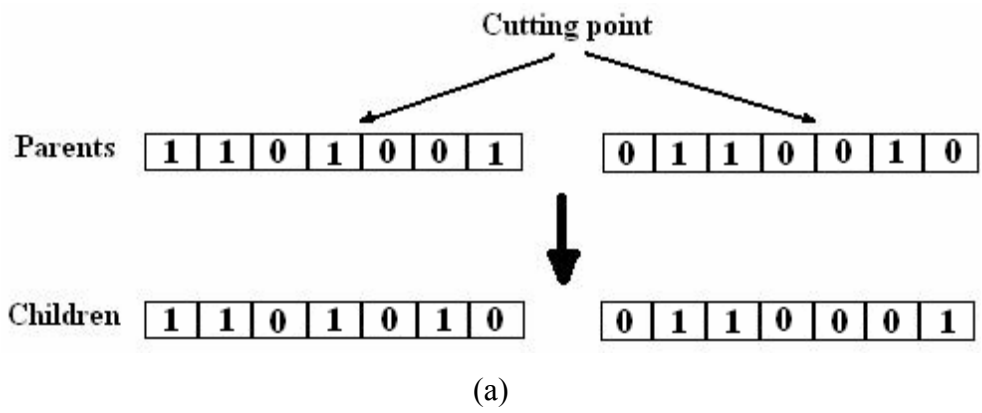
Fig. 2-4 Crossover: (a) one point crossover and (b) two point crossover.
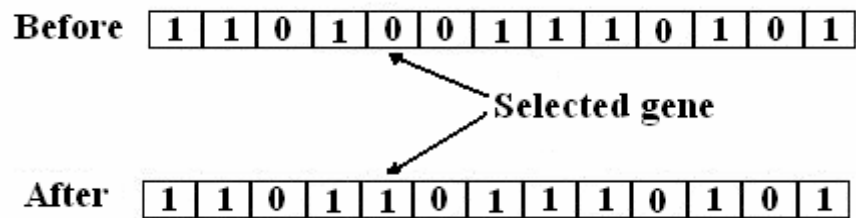
Fig. 2-5 Mutation.
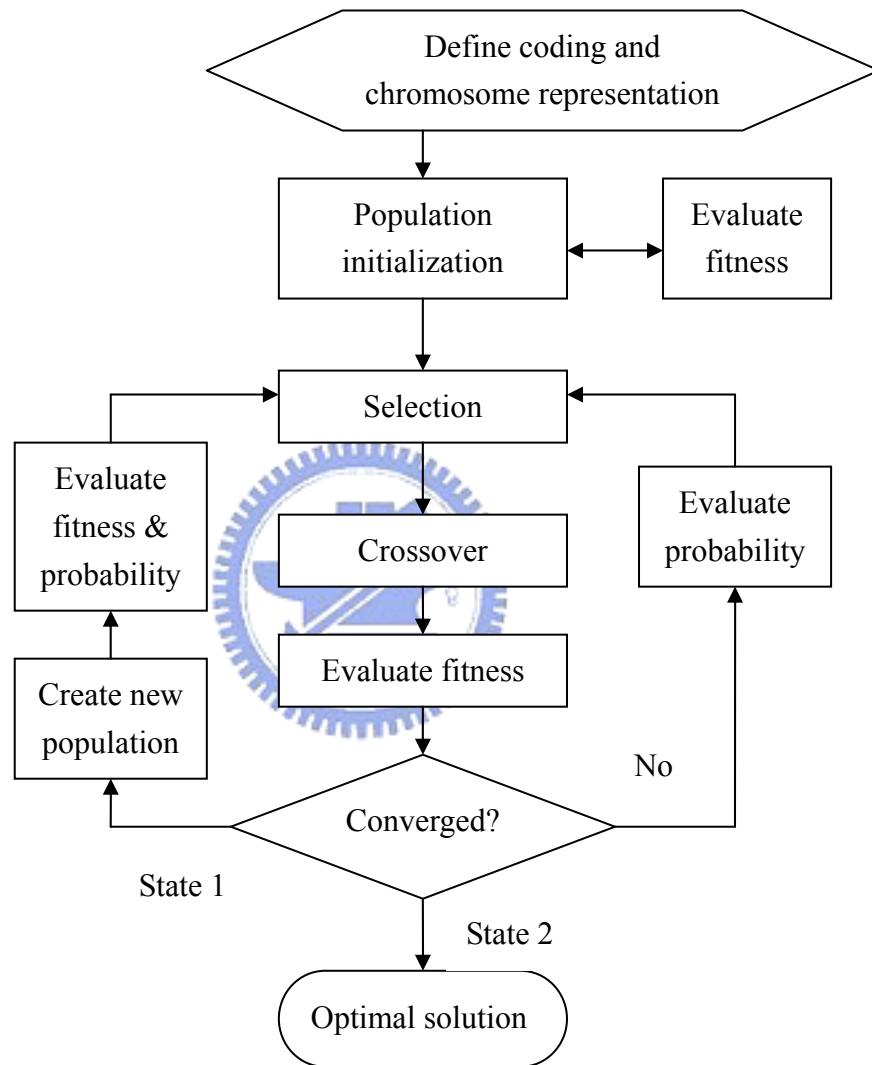
Fig. 2-6 Flowchart of the micro-genetic algorithm.

Chapter 3 Surface function reconstruction

In order to generate a proper surface mesh and ensure the geometrical accuracy of the analytical model, the surface function is necessary during the surface mesh smoothing procedures. In some previous articles, the mesh smoothing procedures were applied to reposition the internal nodes on the plane (or tangent plane) of the primary elements, which is C^0-continuous [14,45]. It is based on an assumption that the primary surface elements were well matched to the original surface. However, in this study, since the given data points may be chosen irregularly, the primary surface elements, which were triangulated directly from the given data points, may not match the original surface well. Therefore, in this study, a C^1 continuous surface function reconstruction algorithm was adopted to ensure the geometrical accuracy during the nodes repositioning.

There are many surface function reconstruction methods developed [23,46–51]. For a finite element analytical model, a C^1-continuous surface function is necessary for sufficient numerical accuracy. Here, a C^1 triangular patch interpolation method developed by Goodman and Said [23] was adopted to reconstruct the surface function. It is a simpler and efficient method for the surface function reconstruction. In this method, surface function is reconstructed by local cubic Bezier triangular patches. The gradients of vertices are necessary for this surface function reconstruction procedure. We adopted a local derivative estimation method, which is also developed by Goodman et al. [52], to calculate the gradients of vertices.

3.1 Gradient estimation

The gradients of surface nodes are calculated by the following approach: V is a vertex of a triangle and t_i, $i = 1,...k$ are the triangles around V (Fig. 3-1). We denote g_i as the gradient of the plane of t_i. The gradient D_v of the node V is

$$D_v = \sum_{i=1}^{k} \lambda_i g_i \Big/ \sum_{i=1}^{k} \lambda_i \qquad\qquad (3\text{-}1)$$

where λ_i is the inverse of the area of the triangle t_i. In (3-1) the node V is assumed to be in the interior of the domain. If the node V is on the boundary of a domain, such as that in Fig. 3-2, the gradient D_v of the node V is given by

$$D_v = \sum_{i=1}^{k} \lambda_i \left\{ \frac{(2/\lambda_i + 1/\lambda_i')g_i - g_i'/\lambda_i}{1/\lambda_i + 1/\lambda_i'} \right\} \Bigg/ \sum_{i=1}^{k} \lambda_i \tag{3-2}$$

which λ_i' is the inverse of the area of the triangle t_i', and t_i' is the triangle which shares the common edge of triangle t_i opposite to V.

The value of g_i can be estimated as the following: Let (x_j, y_j, z_j), $j = 1, 2, 3$ be the vertices of a triangle. Then the triangle can be written as

$$\alpha x + \beta y + \gamma z + \delta = 0 \tag{3-3}$$

where α, β and γ are the components of the normal vector of the triangle

$$\alpha = (y_2 - y_1)(z_3 - z_2) - (z_2 - z_1)(y_3 - y_2)$$
$$\beta = (z_2 - z_1)(x_3 - x_2) - (x_2 - x_1)(z_3 - z_2) \tag{3-4}$$
$$\gamma = (x_2 - x_1)(y_3 - y_2) - (y_2 - y_1)(x_3 - x_2)$$

Then the gradient can be calculated as

$$g_i = \left(\frac{\partial z}{\partial x}, \frac{\partial z}{\partial y} \right) = \left(-\frac{\alpha}{\gamma}, -\frac{\beta}{\gamma} \right) \tag{3-5}$$

3.2 Interpolation method

Consider a triangle T with vertices V_1, V_2, V_3 in barycentric coordinates u, v, w such that any point on the triangle can be expressed as

$$V = uV_1 + vV_2 + wV_3, \qquad u + v + w = 1 \tag{3-6}$$

We denote by e_i the side opposite the vertex V_i, from V_{i+1} to V_{i+2} (see Fig. 3-3). A cubic Bezier triangular patch is then defined as

17

$$P(u,v,w) = u^3 b_{3,0,0} + 3u^2 v b_{2,1,0} + 3u^2 w b_{2,0,1} + 3uv^2 b_{1,2,0} + 3uw^2 b_{1,0,2} + v^3 b_{0,3,0}$$
$$+ 3v^2 w b_{0,2,1} + 3vw^2 b_{0,1,2} + w^3 b_{0,0,3} + 6uvw b_{1,1,1} \tag{3-7}$$

where $b_{i,j,k}$ are the triangular Bezier control points of P. The derivative of P with respect to the direction $z = (z_1, z_2, z_3) = z_1 V_1 + z_2 V_2 + z_3 V_3$, $z_1 + z_2 + z_3 = 0$ is given by

$$\frac{\partial P}{\partial z} = \frac{\partial P}{\partial u} z_1 + \frac{\partial P}{\partial v} z_2 + \frac{\partial P}{\partial w} z_3 \tag{3-8}$$

We assume that function values $F(V_i)$ are given and its first partial derivatives can be calculated from Section 3.2.1. Then the derivative along the side e_i can be calculated by

$$F_{e_i} = \frac{\partial F}{\partial e_i} = (x_{i-1} - x_{i+1})\frac{\partial F}{\partial x} + (y_{i-1} - y_{i+1})\frac{\partial F}{\partial y} \tag{3-9}$$

From the equation given above, we can determine the coordinates of all the control points $b_{i,j,k}$ except $b_{1,1,1}$. For example, following Equation (3-9) the three control points at vertex V_1 can be decided as follows

$$b_{3,0,0} = F(V_1)$$
$$b_{2,1,0} = F(V_1) + \frac{F_{e_3}(V_1)}{3} \tag{3-10}$$
$$b_{2,0,1} = F(V_1) - \frac{F_{e_2}(V_1)}{3}$$

Similarly we can obtain another six control points.

Let n_i be the inward normal direction to the edge e_i (see Fig. 3-3). Then

$$n_1 = (1, h_1 - 1, -h_1)$$
$$n_2 = (-h_2, 1, h_2 - 1_1) \tag{3-11}$$
$$n_3 = (h_3 - 1, -h_3, 1)$$

where

$$h_i = \frac{-e_{i-1} \cdot e_i}{|e_i|^2} \quad , \qquad i = 1,2,3 \tag{3-12}$$

Hence, by using Equations (3-7) and (3-11) we can define the normal derivative on e_i as

$$\frac{\partial P}{\partial n_1} = 3(b_{1,2,0} - b_{0,3,0} - h_1(b_{0,2,1} - b_{0,3,0}))v^2$$

$$+ 6(b^1_{1,1,1} - b_{0,2,1} - h_1(b_{0,1,2} - b_{0,2,1}))vw \tag{3-13}$$

$$+ 3(b_{1,0,2} - b_{0,1,2} - h_1(b_{0,0,3} - b_{0,1,2}))w^2$$

From (3-13), the linear normal derivative on e_i is

$$2(b^1_{1,1,1} - b_{0,2,1} - h_1(b_{0,1,2} - b_{0,2,1})) = (b_{1,2,0} - b_{0,3,0} - h_1(b_{0,2,1} - b_{0,3,0}))$$

$$+ (1 - h_1)(2b_{0,2,1} - b_{0,3,0} - b_{0,1,2})) \tag{3-14}$$

Then

$$b^1_{1,1,1} = \frac{1}{2}(b_{1,2,0} + b_{1,0,2} + h_1(2b_{0,1,2} - b_{0,2,1} - b_{0,0,3})$$

$$+ (1 - h_1)(2b_{0,2,1} - b_{0,3,0} - b_{0,1,2})) \tag{3-15}$$

Similarly we can obtain $b^2_{1,1,1}$ and $b^3_{1,1,1}$. Finally, the interpolation function can be defined as

$$P(u,v,w) = u^3 b_{3,0,0} + 3u^2 v b_{2,1,0} + 3u^2 w b_{2,0,1} + 3uv^2 b_{1,2,0} + 3uw^2 b_{1,0,2}$$

$$+ v^3 b_{0,3,0} + 3v^2 w b_{0,2,1} + 3vw^2 b_{0,1,2} + w^3 b_{0,0,3} \tag{3-16}$$

$$+ 6uvw \frac{v^2 w^2 b^1_{1,1,1} + w^2 u^2 b^2_{1,1,1} + u^2 v^2 b^3_{1,1,1}}{v^2 w^2 + w^2 u^2 + u^2 v^2}$$

3.3 Geometrical accuracy comparison

The comparison of geometrical accuracy for the original C^0-continuous and our enhanced C^1-continuous surface can be shown as follows: thirty-six points and triangulation in Whelan [46] were chosen (Fig. 3-4) and two test functions (Fig. 3-5) were employed:

$$F_1(x, y) = 0.75 \exp(-((9x - 2)^2 + (9y - 2)^2)/4)$$

$$+ 0.75 \exp(-(9x + 1)^2/49 - (9y + 1)/10)$$

$$+ 0.5 \exp(-((9x - 7)^2 + (9y - 3)^2)/4)$$

$$- 0.2 \exp(-(9x - 4)^2 - (9y - 7)^2)$$

$$F_2(x, y) = (1.25 + \cos(5.4y))/(6 + 6(3x - 1)^2)$$

The interpolated values of the test functions at a 25×25 uniform mesh points in a unit square were computed and the maximum and mean errors. The computed surface errors were shown in Fig. 3-6 and Fig. 3-7 for test function 1 and test function 2 respectively. The surface errors, shown in Table 3-1, indicate that the C^1-continus surface is more accuracy than the C^0-continuous surface both on maximum and mean surface errors. Therefore, surface mesh smoothing based on the reconstructed C^1 surfaces is beneficial to enhance the geometrical accuracy of the analytical model.
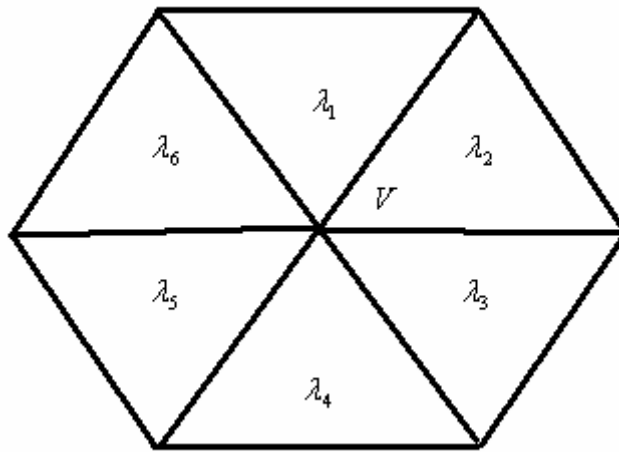
Fig. 3-1 Triangles in the triangulation.
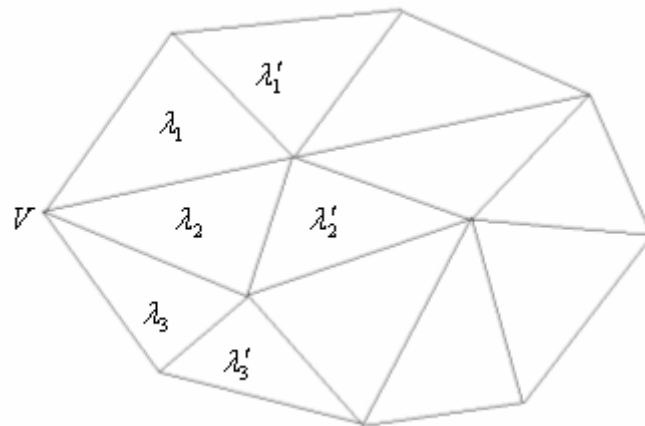
Fig. 3-2 Node V on the boundary.
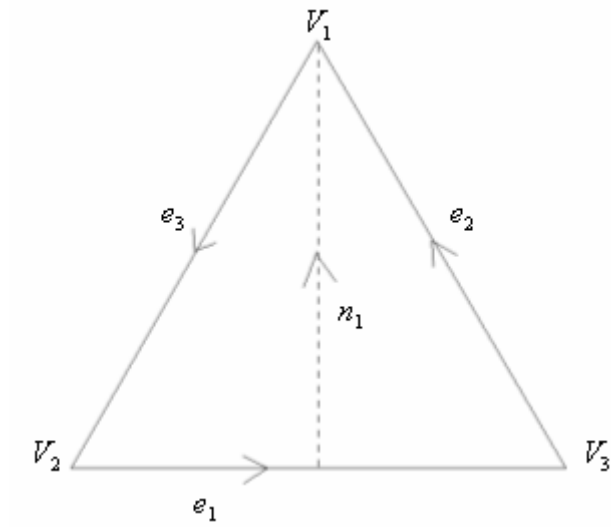
Fig. 3-3 Notation of a triangle.
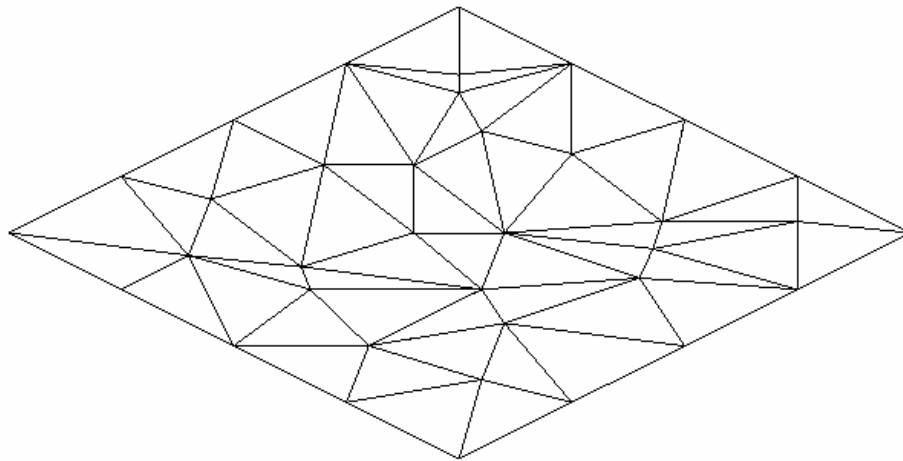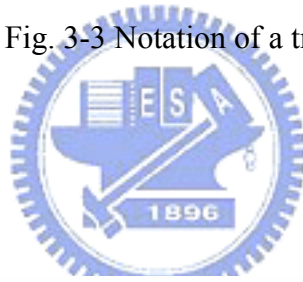
Fig. 3-4 Thirty-six points and triangulations.

(a)
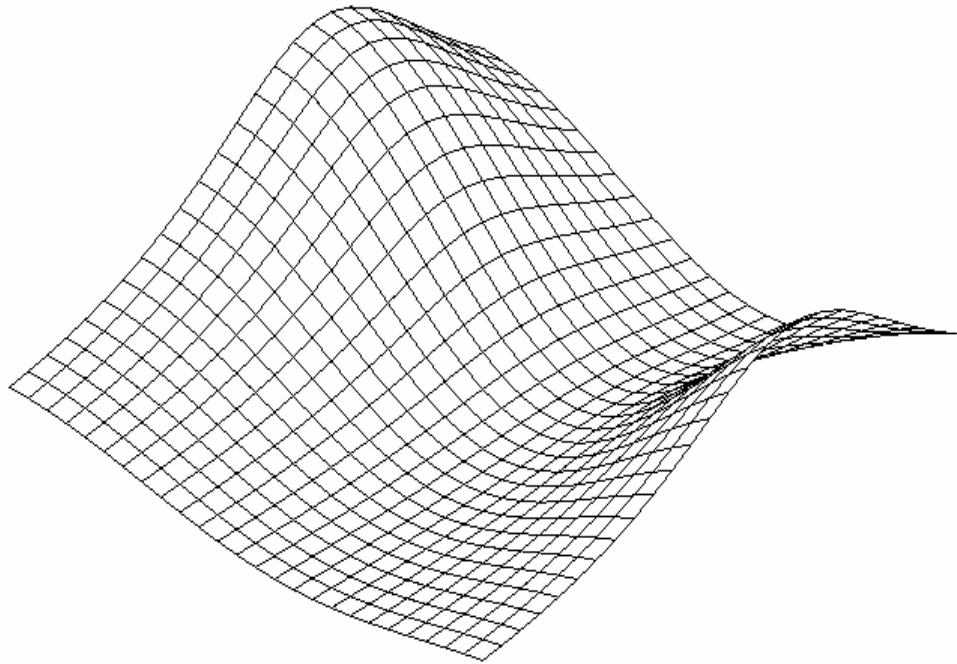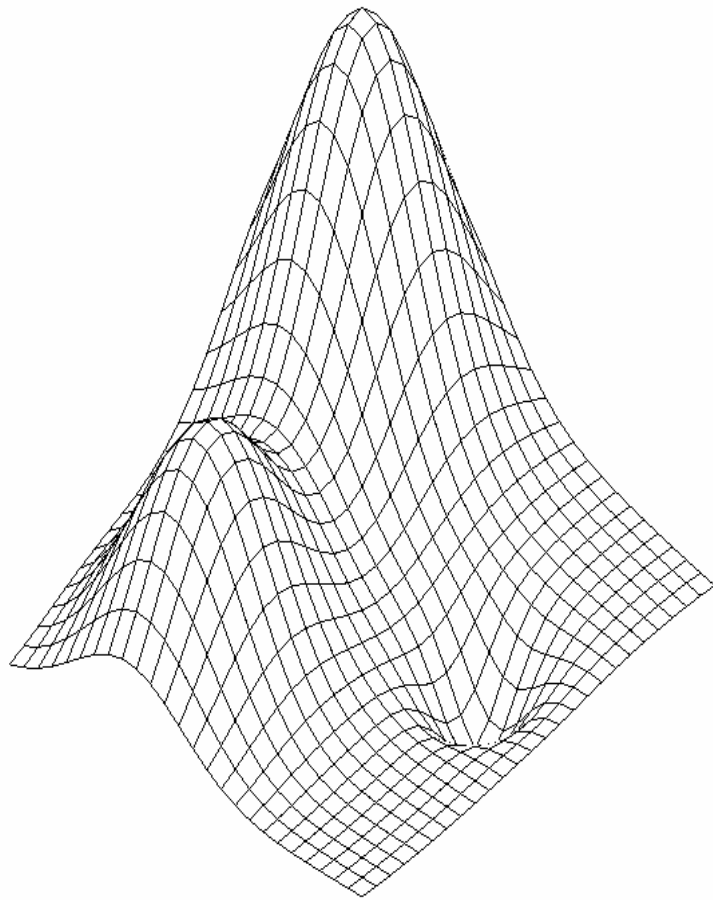
(b)

Fig. 3-5 (a) test function 1 and (b) test function 2.
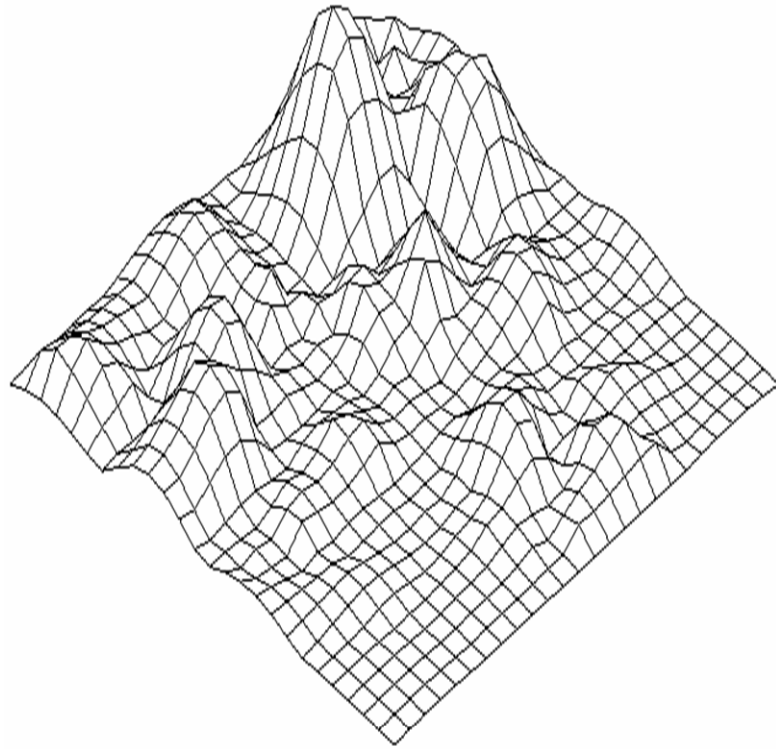
(a)
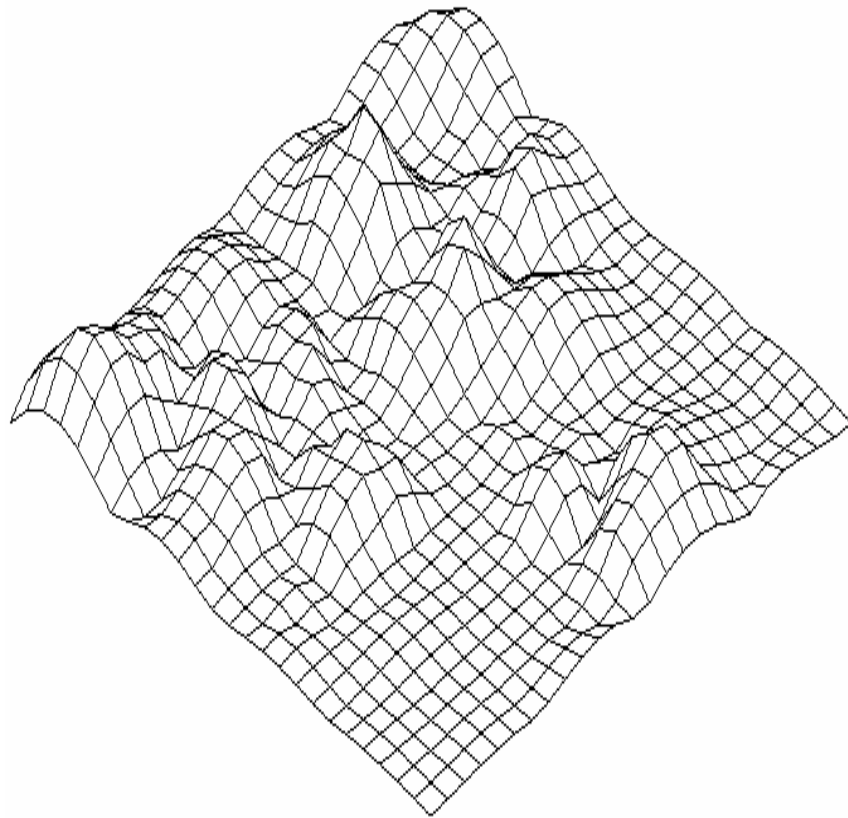
(b)

Fig. 3-6 Surface errors of test function 1: (a) C^0 surface and (b) C^1 surface.
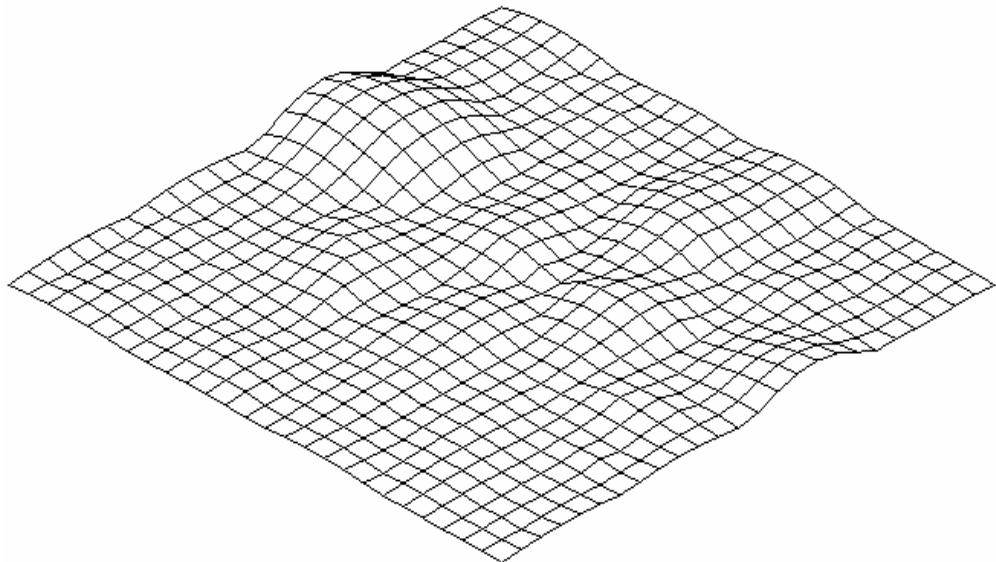
(a)
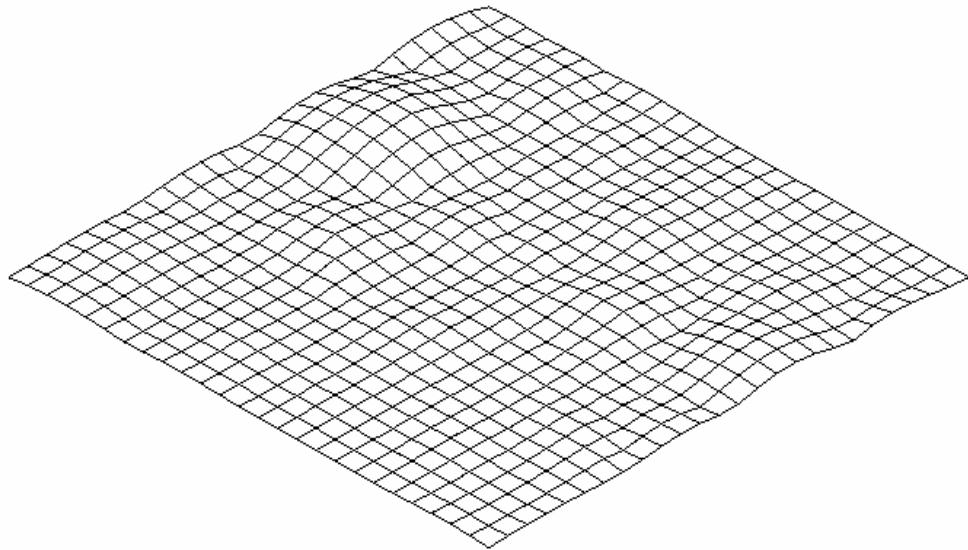
(b)

Fig. 3-7 Surface errors of test function 2: (a) C^0 surface and (b) C^1 surface.

Table 3-1 Surface errors of the test functions for

C^0 and C^1 surface reconstruction.

Test function	C^0 surface		C^1 surface	
	Max. error	Mean error	Max. error	Mean error
$F1(x, y)$	0.215184	0.027594	0.120067	0.022945
$F2(x, y)$	0.059769	0.008789	0.035420	0.005101

Chapter 4. Surface mesh smoothing

4.1 Mesh generation

4.1.1 Triangular mesh generation

In general, finite element surface mesh is generated based on prescribed patch interpolation by adopting the Delaunay Triangulation [5] or Advancing Front Methods [6]. However, the generation of surface mesh based on unorganized points set is necessary in some science and engineering fields, where geometrical data is often measured or generated at isolated and unorganized positions, such as mentioned earlier of the biomedical research. In this application, the given data is just the points set and the surface function is yet to be defined. Therefore, the surface mesh can not be generated based on its surface function directly. For this application, a common way to reconstruct the surface model is to triangulate the given points [7-10]. The triangulation procedure aims at generating a primary triangular surface mesh as well as creating background triangular patches for the use in surface function reconstruction procedure. Furthermore, since the distribution of the given points may be irregular over the surface of the model, the primary triangular meshes always contain some ill-posed triangles. Therefore, some mesh cleanup operations [53] were introduced to improve the topological connectivity of the triangular meshes, and then MGA approach was applied to enhance the mesh quality further.

4.1.2 Quadrilateral mesh generation

Once the primary triangular surface mesh was created, the quadrilateral surface mesh can be generated based on the triangular one. The conversion scheme [4,45,54-56] was employed to serve this purpose. It is a common and convenient way to generate an unstructured quadrilateral mesh. The quadrilateral mesh was created by a careful process to merge two adjoining triangles to form a quadrilateral element. However, the conversion scheme usually introduces plenty of ill-posed quadrilaterals. To improve the mesh quality, a two-stage procedure is required. First, mesh structure modification (topological improvement) operations [57,58], such as edge swapping, node elimination and edge dividing, were employed to refine the mesh connectivity. Then the mesh quality was further enhanced by

applying the MGA approach.

4.1.3 Mesh structure modification operations

For the finite element mesh generation, the ideal numbers of elements connected to a node are six and four for triangular and quadrilateral mesh respectively. Generally, the bad nodes, which were connected with more than or less than the ideal number of elements, were treated before mesh smoothing procedure. In this section, we presented three basic mesh structure modification operations to tackle these bad nodes.

1. Edge swapping

This operator swaps an edge adjacent to two elements. It is used to adjust the number of surrounding elements of the connected nodes. As shown in Fig. 4-1(a), the number of elements connected to node a (N_a) and node b (N_b) are seven, which are more than the ideal number of triangular elements. Therefore, the interior edge was swapped to improve this mesh structure. In Fig. 4-1(b), N_b and N_e are five, which are more than the ideal number of quadrilateral elements, and the interior edge (edge $\overline{be}$) was swapped (edge $\overline{cf}$) to modify this mesh structure.
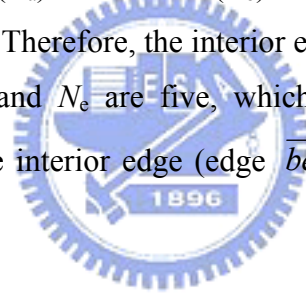
2. Node eliminating

This operator eliminates nodes whose number of surrounding elements is less than the ideal number. As shown in Fig. 4-2(a), N_d is three and it is an improper node. For this situation, the node d is eliminated to exclude the improper node. Figure 4-2(b) shows the improper node g with three surrounding quadrilateral elements and the mesh structure will be improved by eliminated the improper node g.

3. Edge dividing

This operator divides edge by inserting a new node on the center of a long edge. In Fig. 4-3(a), the edge $\overline{bd}$ is longer than others. Then a node f was inserted to the center of edge $\overline{bd}$ and the nearby edges were rearranged to improve the triangular mesh quality locally. Similarly, the longest edge $\overline{be}$ in Fig. 4-3(b) was divided by inserting a new node g on the

center and the elements connected to it were rearranged too.

There are many mesh structure modification operations presented in the previous articles [53,57,58]. These operations were based on the three basic operations, edge swapping, node elimination and edge dividing. Please refer to [53], [57] and [58] for the details of the mesh structure modification operations.

4.2 Micro-genetic algorithm surface mesh smoothing

In this thesis, the given surface mesh was triangular mesh and/or converted the triangular mesh into quadrilateral mesh. The surface mesh was first refined by the mesh structure modification operators [53,57,58], and then the MGA mesh smoothing procedures were applied to enhance the surface mesh quality further. The procedures of our surface mesh smoothing and the MGA adopted in our scheme were summarized as follows:

Step 1) Input data: Input the data of primary mesh, which includes surface function, node positions and element connectivity. If the surface function is not given, the gradients of nodes will estimated by the gradients estimation procedures [52].

Step 2) MGA mesh smoothing begins:

Step 3) Search the optimal solutions within each adjacent element by using Step 4 to Step 7 and then choose the best one to be the new position of the node.

Step 4) Initial population: The MGA requires multiple convergences. According to the reference [17], a population size of five is chosen in each convergence. The best individual of the previous generation will be held. The others are generated randomly.

Step 5) Decode the strings and calculate their node positions based on the reconstructed surface function (Section 3.2). Calculate their fitness values and then carry the best string to the next generation.

Step 6) Select four strings (contains the best string) for reproduction by employing the roulette wheel strategy [21]. Generate four individuals by employing the crossover operator with probability of one [17].

Step 7) Check the convergence criterion. If it is not convergence, go to step 5 or else go to step 3 or step 4.

Step 8) Go to step 2 to smooth next node until the end of the smoothing.

Step 9) Check the convergence of the whole mesh smoothing procedures. If it is not convergence, go to step 2 or else end off the smoothing procedures.

4.2.1 Design parameters

In the MGA mesh smoothing procedures, the design parameters were chosen to represent the nodes position. In order to avoid degenerate elements, the search space was restricted within a triangular area for each adjacent element in both triangular and quadrilateral mesh smoothing. To represent a node lay on a triangle, we choose two parameters r_1 and r_2, which relate to the barycentric coordinates as the following: Consider a triangle T (Fig. 4-4) with vertices V_1, V_2 and V_3 in barycentric coordinates u, v and w, such that any point on the triangle can be expressed as

$$V = uV_1 + vV_2 + wV_3, \qquad u + v + w = 1 \tag{3-17}$$

Now, with $0 < r_i < 1$, $i = 1, 2$, the barycentric coordinates can be given as

$$u = r_1(1 - r_2) + (1 - r_1)(1 - r_2) = 1 - r_2$$
$$v = r_2(1 - r_1) \tag{3-18}$$
$$w = r_1 r_2$$

Substituting (3-18) into (3-17), we get

$$V = (1 - r_2)V_1 + r_2(1 - r_1)V_2 + r_1 r_2 V_3 \tag{3-19}$$

As shown in Fig. 4-4, the vertices V_1, V_2 and V_3 are collinear when $r_2 = 1$. To avoid that, we let $0 < r_2 < 0.5$. After the position of point V is obtained, the exact position is calculated by mapping it to the original surface based on its corresponding triangular patch and the local reconstructed surface function (Section 3.2).

4.2.2 Fitness function

In this study, the fitness function is a criterion to judge the mesh quality and defined with the mesh quality measurement index. For the triangular mesh quality measurement, the common used quality index is

$$\alpha = 2\sqrt{3} \, \frac{\| AB \times AC \|}{\| AB \|^2 + \| BC \|^2 + \| AC \|^2} \tag{3-20}$$

where A, B, C are the vertices of a triangle. According to this mesh quality measurement, the fitness function for the triangular mesh smoothing F_t is defined as

$$F_t = \sum_{i=1}^{n} \alpha_i \tag{3-21}$$

where n is the number of adjacent triangular elements.

For the quadrilateral mesh quality measurement, Knupp [59] presented an algebraic mesh quality metrics from the Jacobian matrix. The definition of quadrilateral shape quality metric is as follows: for a plane quadrilateral element, let the coordinates of the four nodes be (x_k, y_k), $k=0,1,2,3$. The Jacobian matrices, A_k, one at each node of the quadrilateral:

$$A_k = \begin{pmatrix} x_{k+1} - x_k & x_{k+3} - x_k \\ y_{k+1} - y_k & y_{k+3} - y_k \end{pmatrix} \tag{3-22}$$

where the indices $k+1$ and $k+3$ are taken modulo four, for example, if $k=1$ then $k+3$ becomes 0. Four metric tensors are obtained by the combinations $A_k^T A_k$. Let $\lambda_{ij}^k, i, j=1,2$, be the ij th component of the k th metric tensor. Geometrically, at the k th node, λ_{11}^k is the square of the length of the side connecting nodes k and $k+1$, λ_{22}^k is the square of the length of the side connecting nodes k and $k+3$. Let θ_k be the angle between the two sides joined at the k th node, the quadrilateral shape quality metric can be expressed as

$$\beta = \frac{8}{\sum_{k=0}^{3}(1+r_k^2)/(r_k \sin \theta_k)} \tag{3-23}$$

where $r = \sqrt{\lambda_{22}/\lambda_{11}}$ is the length ratio of kth node. This concept can be extended to measure quadrilateral surface mesh quality directly. Then the fitness function for the quadrilateral mesh smoothing F_q is defined as

$$F_q = \sum_{i=1}^{n} \beta_i \qquad (3\text{-}24)$$

where n is the number of adjacent quadrilateral elements.

4.3 Surface mesh smoothing results

The proposed approach is tested in several unorganized point datasets. A simple geometry of saddle shape with prescribed surface function is used to validate the procedure and to compare the performance of our MGA approach and the conjugate gradient method (Table 4-1). It is then applied to complicated geometries, such as wing-fuselage, which is often used in preliminary aircraft design, and biological dataset of shapes of a foot and a rat, which are constructed from contours by a three dimensional laser scanning and from a sequence of segmented bio-images respectively. The geometrical reconstruction of bio-images is a crucial pre-processing for physical modeling in biology and biomechanics. So, the applications are used to demonstrate not only the effectiveness but also the practical use of our approach. In order to show the capability of our MGA mesh smoothing approach, all of the smoothed results are obtained by smoothing the primary meshes directly without any additional mesh treatment. The mesh quality is measured according to the Section 4.2 that the triangular mesh quality index is α and the quadrilateral mesh quality index is β. The results are summarized in Table 4-2 and 4-3 for triangular and quadrilateral surface meshes respectively. Significant enhancement is found by our approach. Furthermore, in the Table 3-4, the worst quadrilateral mesh quality is set as 0.0001, which represents that one of theinterior angle is greater than 179^0 and the codes are run in Linux PC with a dual core AMD 2 GHz CPU and 3 GHz RAM.

The first example is a basic mathematical function of saddle shape (Fig. 4-5), which allows us to scrutinize the performance of the approach. The surface function is denoted as the following:

$$z = x^2 \big/ 10 - y^2 \big/ 4 \qquad\qquad\qquad\qquad (3\text{-}25)$$

The saddle shape surface, unlike the usual well-behaved elliptic shape, has negative curvature, which is appealing to be used as a test case for the surface smoothing [60]. The triangular surface mesh is generated based on Delaunay triangulation and the quadrilateral surface mesh converted from the triangular mesh (Section 4.1). The performance of MGA can be observed by comparing with that of the conjugate gradient method in the saddle shape. The Table 4-2 shows that the improvement of the mean quality of triangular mesh reaches to 0.9562 and 0.9509 by both approaches, but the CPU time of our MGA approach is approximate five times of the conjugate gradient method. This is one drawback of GA, but can be easily tackled by parallelism and there are several parallel GA [24] developed with great success. The approach is similarly employed to the quadrilateral mesh. Our quadrilateral meshes are generated using a popular conversion scheme or fission scheme [4,45,54-56]. The conversion scheme essentially merges two neighboring triangles to form a new quadrilateral. This method may introduce ill-posed quadrilaterals, and needs further treatments [57,58] for practical use. The Table 4-3 shows that the improvement of mean quality of quadrilateral mesh reaches to 0.8736 and 0.9001 by employing the conjugate gradient method and our MGA approach respectively. It is clear that our performance as a global method achievement for mesh quality improvement is better than the conjugate gradient method. The enhancements of the mesh quality can be also visually observed from Fig. 4-5 and Fig. 4-6 for triangular and quadrilateral surface mesh respectively.

The following example is a complicated geometry of wing-fuselage configuration of NCKU-ILD-101 [61]. Such kind of geometrical model is often used in CFD simulation for aircraft preliminary design. The usual practice for generating a surface mesh for such a geometrical model is based on a pre-defined patch interpolation. The current data is prepared from a point datasets that is well generated by usual mesh generation methods of Delaunay triangulation. The point datasets are deliberately reduced from 9,962 points to 1,314 points, but the feature of the geometry is carefully preserved by using AMIRA [62]. The reduction makes mesh so coarse that it is difficult to maintain quality for simulation. However, it is well suited to test the performance of the current MGA procedure. The points at the edges and joints have to be marked and fixed to avoid singularity during the smoothing. The results are shown in Fig. 4-7 and Fig. 4-8 for triangular and quadrilateral meshes respectively. The improvement is significant, which can be seen from the quality indices measured in Table 4-2 and 4-3. The mean quality index of triangular mesh is enhanced from 0.8483 to 0.9046. It is

33

well known that quadrilateral mesh is less stiff than triangular mesh and allows more degrees of freedom to move the mesh to change the shape of elements. As a result, it needs more smoothing treatments after generating the surface mesh. Our results show significant improvement in terms of worst and average property measured within elements. The mean and worst qualities are enhanced from 0.6982 to 0.8580 and 0.0001 to 0.4215 respectively.

Due to the advance of image processing, geometry reconstruction and mesh generation, nowadays larger and more complicated geometry models can be reconstructed from a sequence of bio-medical images data set. The need for such reconstruction is immense and it has become a common practice for bio-medical and bioengineering study. By scrutinizing the reconstruction procedure for such geometry models, it can be found that the surface geometry is usually defined by a set of unorganized points, or at least by a sequence of un-associated contours, that is identified by pattern recognition methods on each image of interest. The surface triangulation is not straightforward. It is even more challenging for surface mesh quality enhancement in that the re-arrangement of the point distribution needs higher order interpolation methods for accuracy. Two test cases are given to demonstrate the capability of the proposed methods for tackling these challenging issues.

The first example is the foot shape model of Polhemus [63]. The original model was created by using FastSCAN with the FastRBF Extensions. The surface data points are measured by the laser scanner FastSCAN, and then the data points are reconstructed to form the geometrical model by the software FastRBF Extensions. It is a very convenient and efficient way to reconstruct a geometrical model, especially when the surface function is not pre-defined, by using a laser scanner system. In this study, the original foot model contains 25,845 nodes. Similarly the original data points are reduced to 4,039 and it contains 8,000 triangles on the surface. Our MGA approach constructs a high order interpolation and iteratively optimizes the point distribution in terms of local evolution. The triangular mesh quality was enhanced as expected from 0.8275 to 0.9192 (Fig. 4-9). The original surface mesh obtained is actually well defined. However, the current approach can still give further enhancement of the mesh quality. For systematical comparison, the quadrilateral mesh is generated and smoothed in a similar fashion. The results of obvious improvement are as expected that the surface quadrilaterals are more regular after the MGA approach (Fig. 4-10). This also can be readily observed from the mean quality, which is improved from 0.7049 to 0.8632 (Table 4-3).

The last case is a rat shape that is reconstructed from a sequence of image slices of histological sections from Ryutaro Himeno of RIKEN [64]. The original reconstructed model

contains skin, bone, organs and so on, and it can help people to observe the whole model of rat virtually without dissect a real rat. This approach can be used to reconstruct more models of biology. In this study, we extract the skin model and reduce it by using AMIRA. As shown in Fig. 4-11, this model contains 25,670 nodes and 51,354 elements. The reconstructed shape is rough and irregular and the primary surface mesh contains many poor triangles elements. Some of the nodes connect to 3 elements and others connect to more than 9 elements. The poor connectivity is treated first by the mesh structure modification operators [53,57,58]. To avoid interpolation error, the singular points, which locate at the boundary or contain large curvature variation, need be identified and fixed before the surface mesh smoothing. The MGA procedure is then used to re-construct surface interpolation function and to smooth the mesh by optimizing the point distribution. The result is shown in Fig. 4-11(b) and the mean mesh quality improved from 0.8963 to 0.9453. The similar improvement for quadrilateral mesh can be found in Fig. 4-12 and Table 4-3.
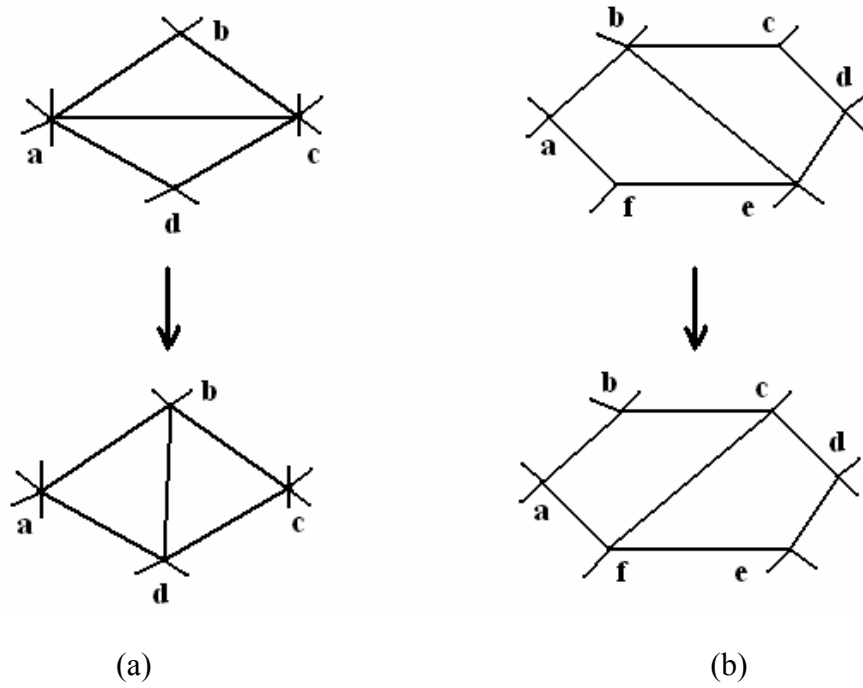
Fig. 4-1 Edge swapping: (a) triangular elements and (b) quadrilateral elements.
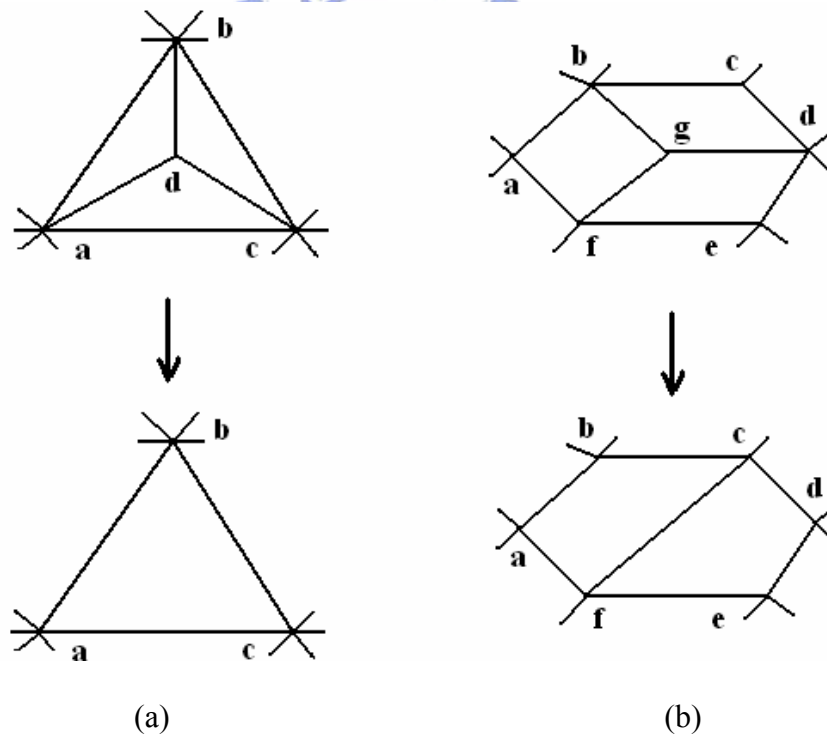
Fig. 4-2 Node eliminating: (a) triangular elements and (b) quadrilateral elements.
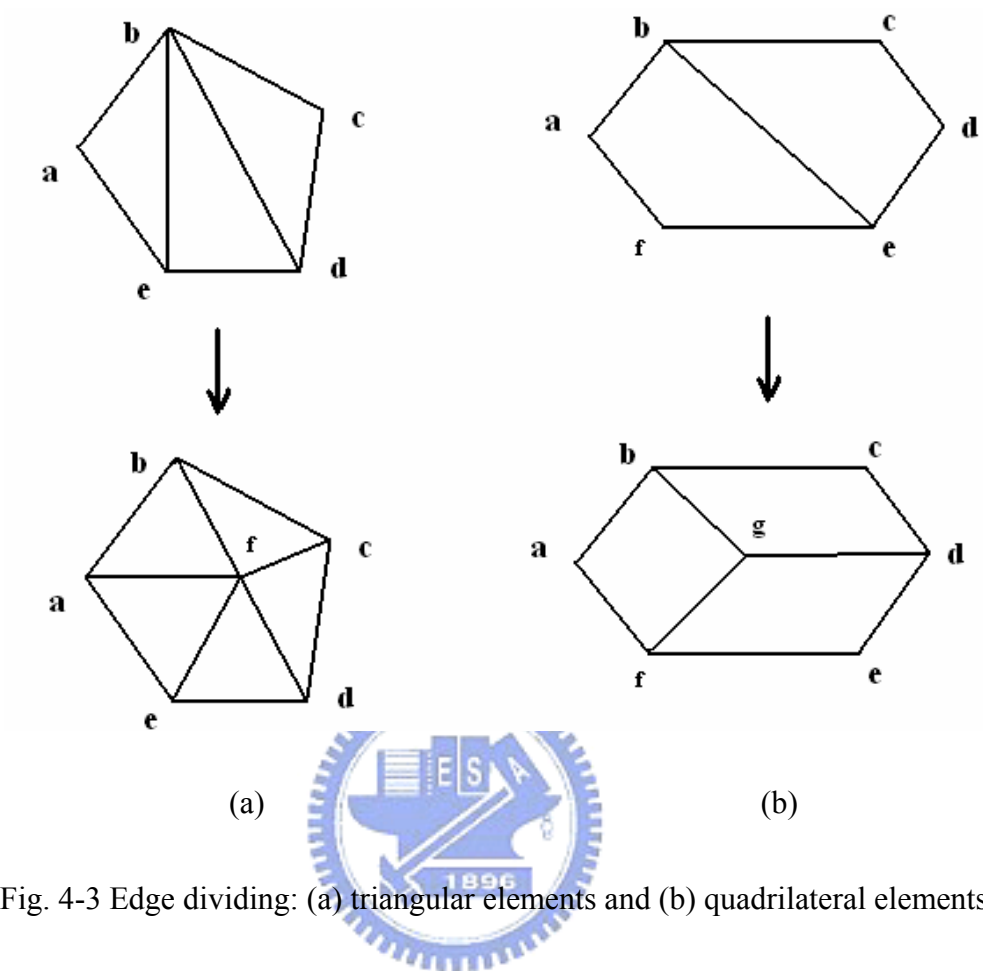
Fig. 4-3 Edge dividing: (a) triangular elements and (b) quadrilateral elements.
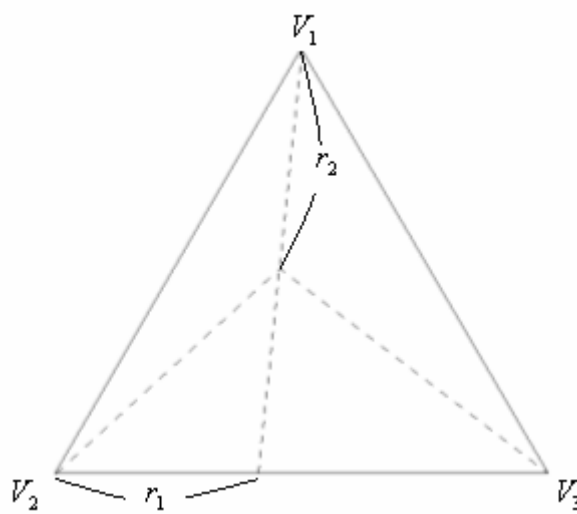
Fig. 4-4 Design parameters definition on a triangle.

Table 4-1. The comparison between conjugate gradient method and MGA method using the saddle geometry.

Method	Object	Number of node	Number of element	Worst quality	Mean quality	CPU time(sec)
Conjugate gradient	Triangular saddle mesh	601	1104	0.6834	0.9562	0.8000
MGA				0.4591	0.9509	3.8199
Conjugate gradient	Quadrilateral saddle mesh	597	548	0.4099	0.8736	0.8400
MGA				0.5696	0.9001	2.3199

Table 4-2. Mesh quality improvement for the triangular surface meshes.

	Object	Number of node	Number of element	Worst quality	Mean quality	CPU time(sec)
original	Wing-fuselage	1419	2432	0.2535	0.8483	3.0500
smoothed				0.2535	0.9046	
original	Foot	4039	8000	0.3803	0.8275	23.8200
smoothed				0.3469	0.9192	
original	Rat	25670	51354	0.2225	0.8963	150.0509
smoothed				0.2460	0.9453	

Table 4-3. Mesh quality improvement for the quadrilateral surface meshes.

	Object	Number of node	Number of element	Worst quality	Mean quality	CPU time(sec)
original	Wing-fuselage	1405	1200	0.0001	0.6982	4.1000
smoothed				0.4215	0.8580	
original	Foot	4010	3971	0.0001	0.7049	19.6400
smoothed				0.4111	0.8632	
original	Rat	25374	25383	0.0001	0.7568	88.8099
smoothed				0.2553	0.8899	
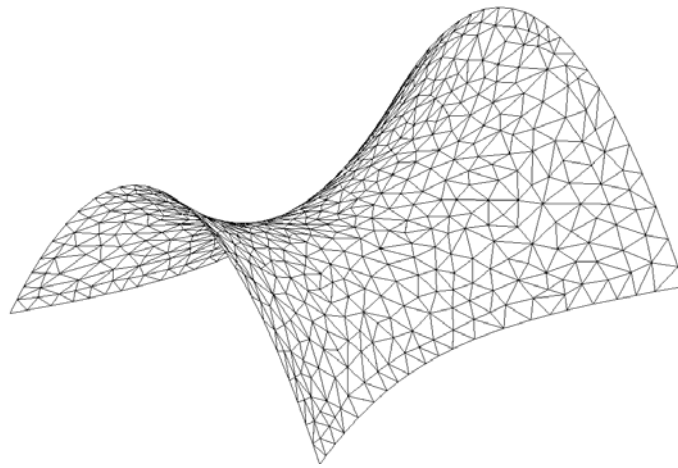
(a)
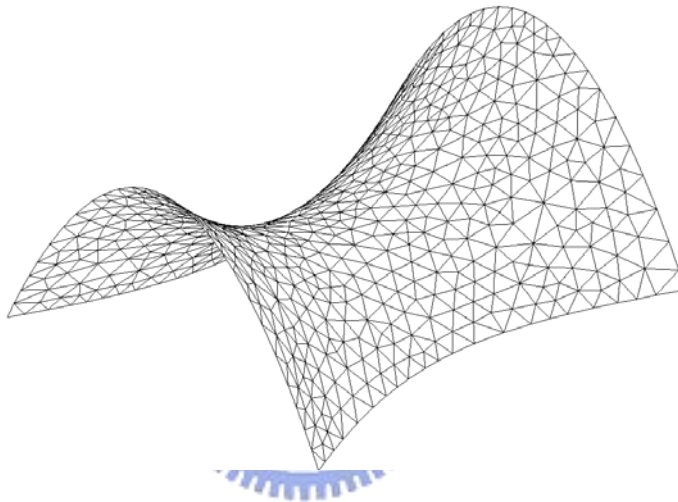
(b)
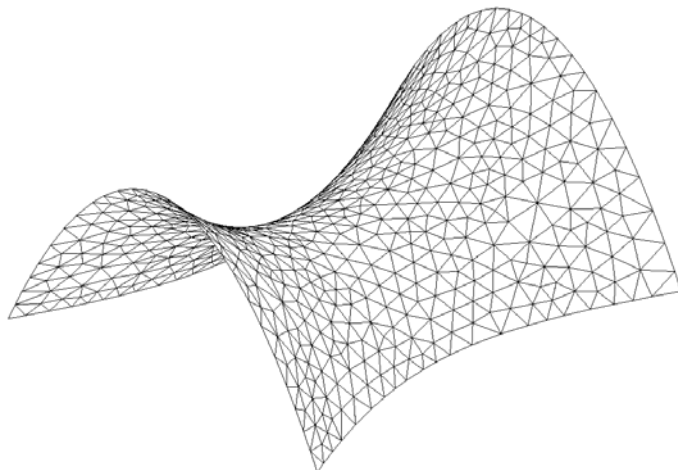
(c)

Fig. 4-5 Triangular surface mesh of saddle: (a) Original surface mesh; (b) Surface mesh after MGA smoothing; and (c) Surface mesh after conjugate gradient smoothing.
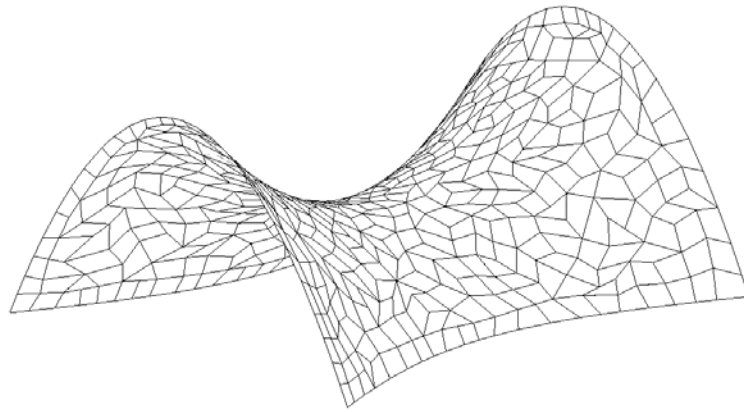
(a)
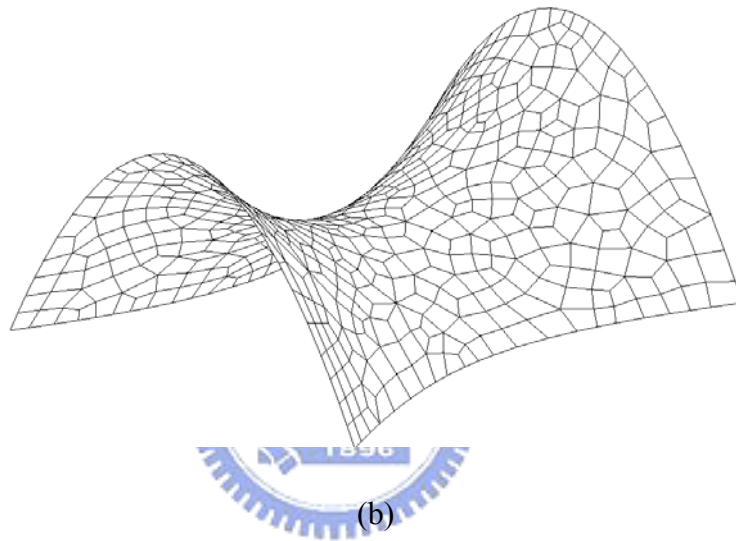
(b)
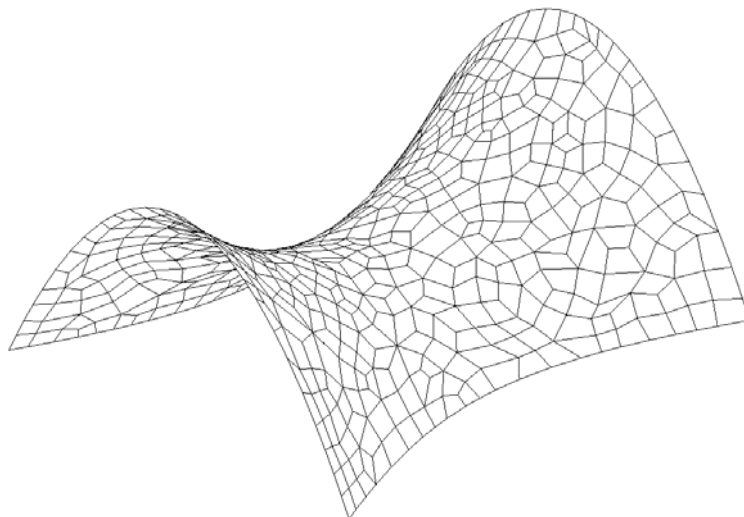
(c)

Fig. 4-6 Quadrilateral surface mesh of saddle: (a) Original surface mesh; (b) Surface mesh after MGA smoothing; and (c) Surface mesh after conjugate gradient smoothing.
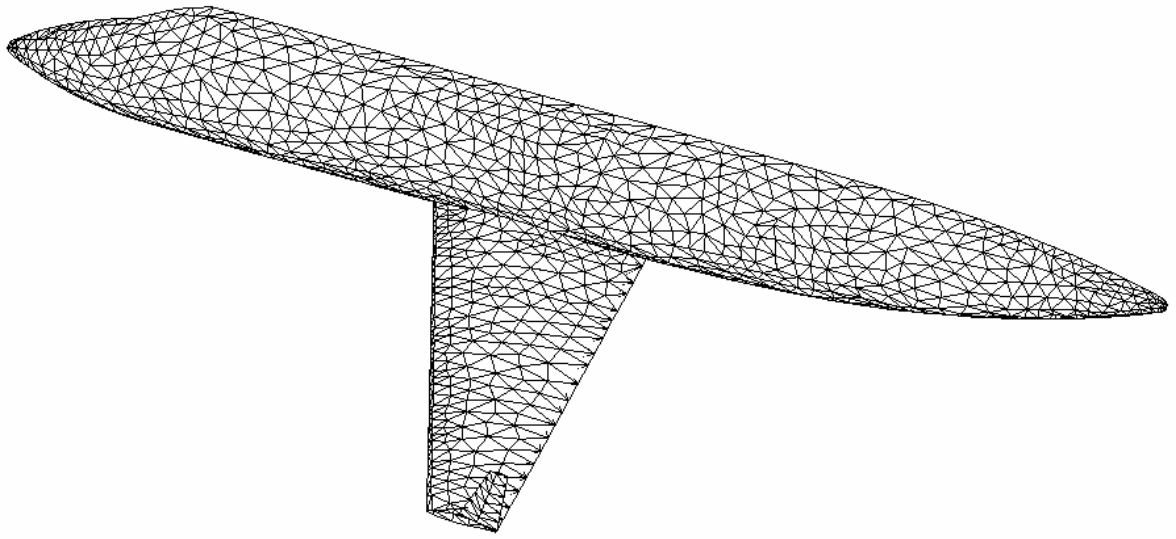
(a)
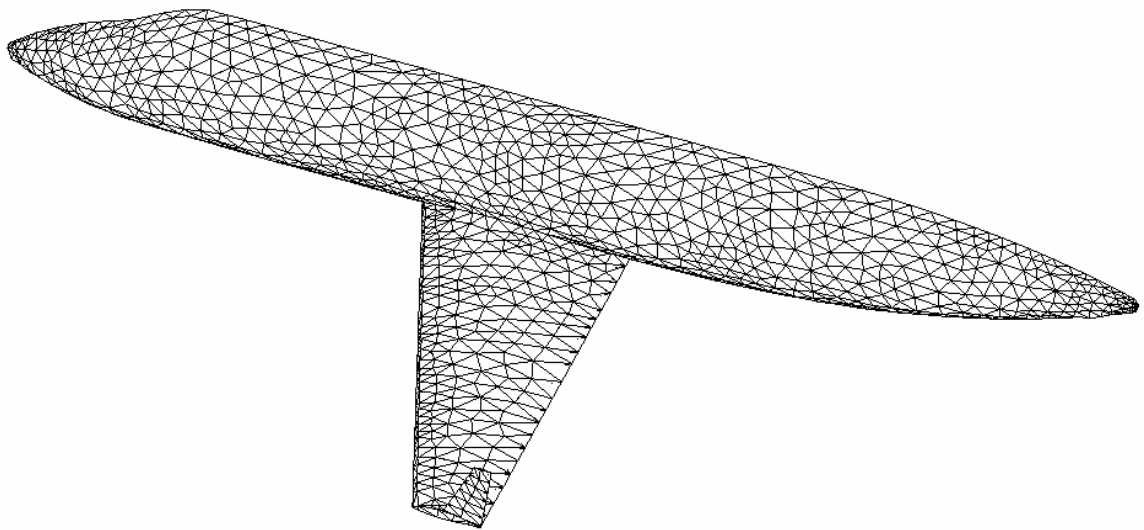
(b)

Fig. 4-7 Triangular surface mesh of wing-fuselage: (a) Original surface mesh and
(b) Surface mesh after smoothing.
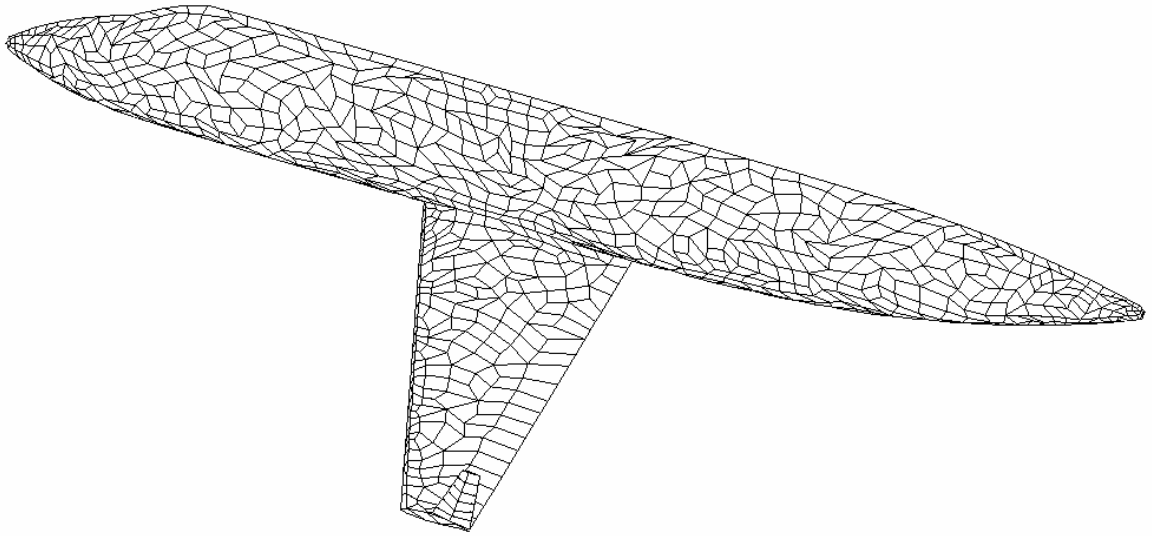
(a)
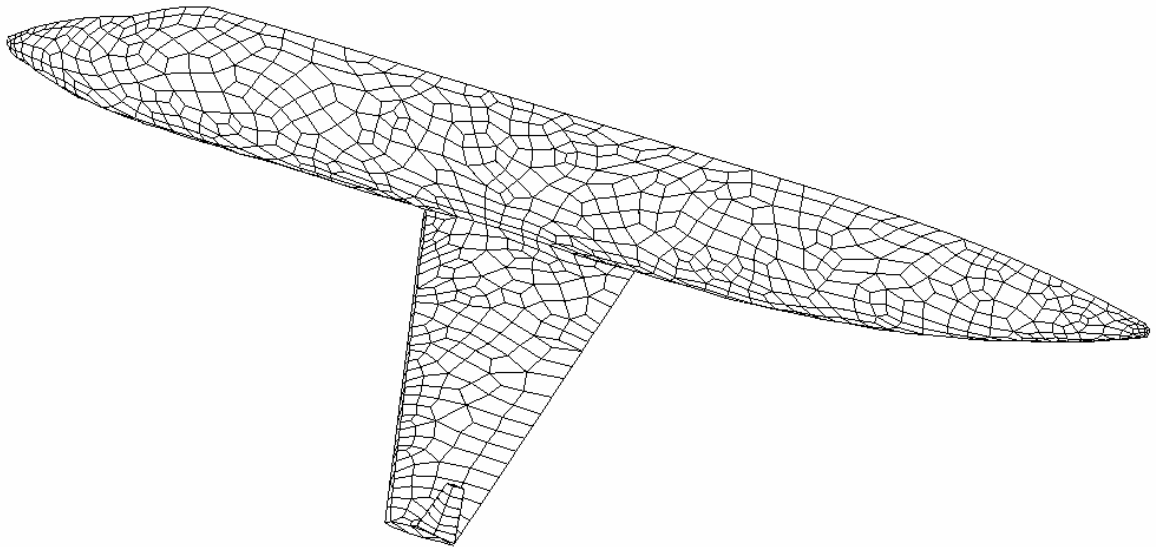
(b)

Fig. 4-8 Quadrilateral surface mesh of wing-fuselage: (a) Original surface mesh and
(b) Surface mesh after smoothing.

(a)   (b)
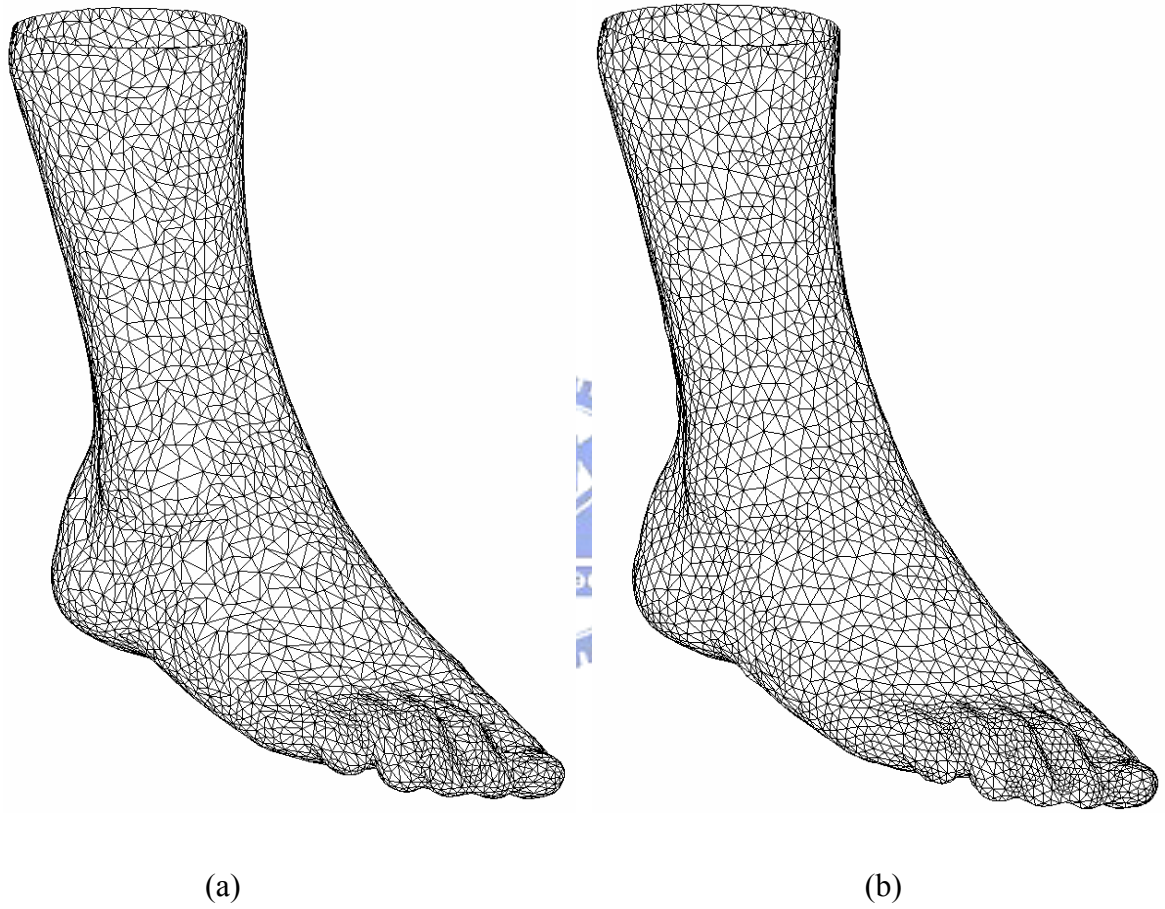
Fig. 4-9 Triangular surface mesh of foot: (a) Original surface mesh and

(b) Surface mesh after smoothing.

(a)   (b)
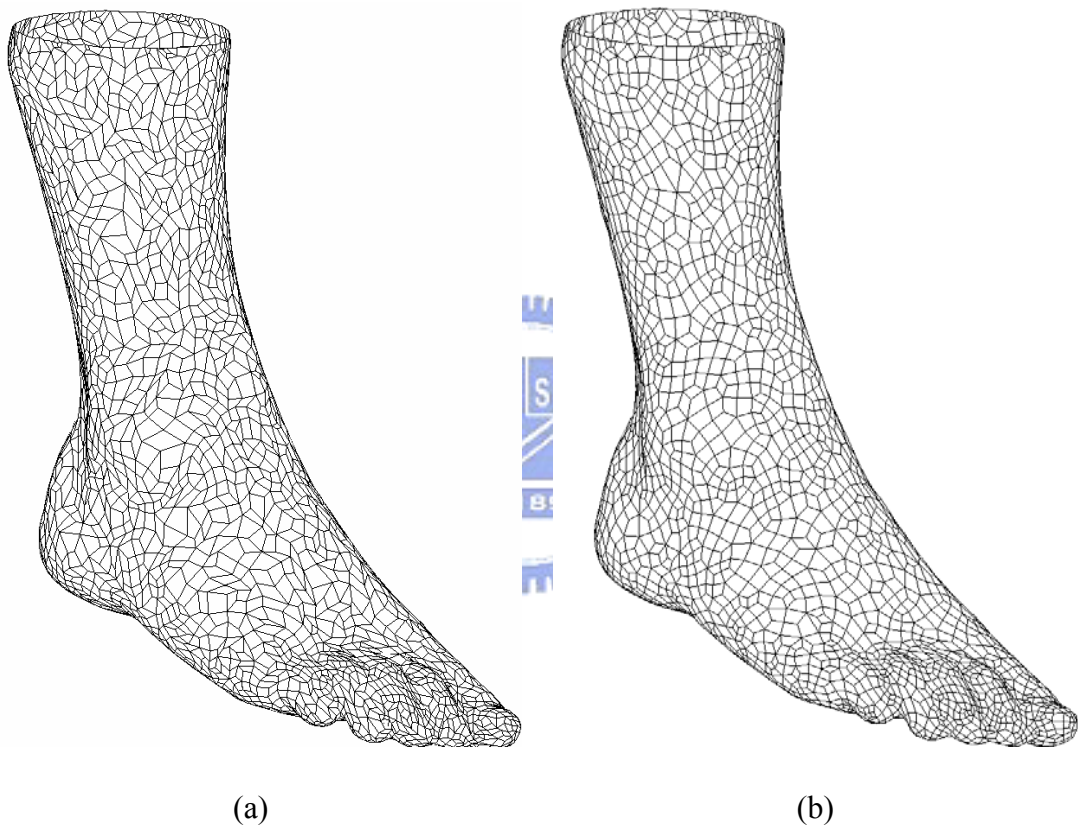
Fig. 4-10 Quadrilateral surface mesh of foot: (a) Original surface mesh and

(b) Surface mesh after smoothing.

(a)

(b)

(c)   (d)
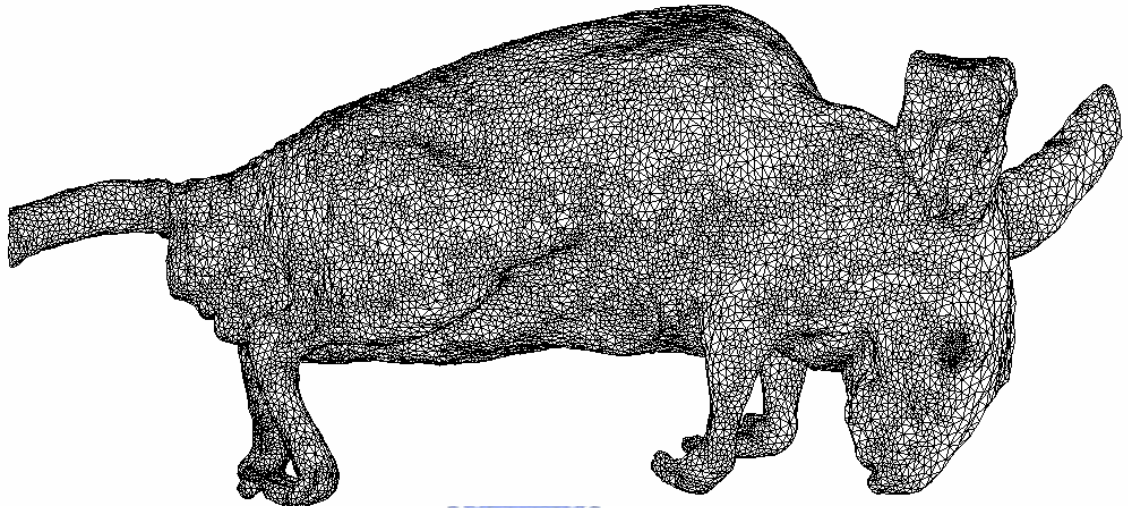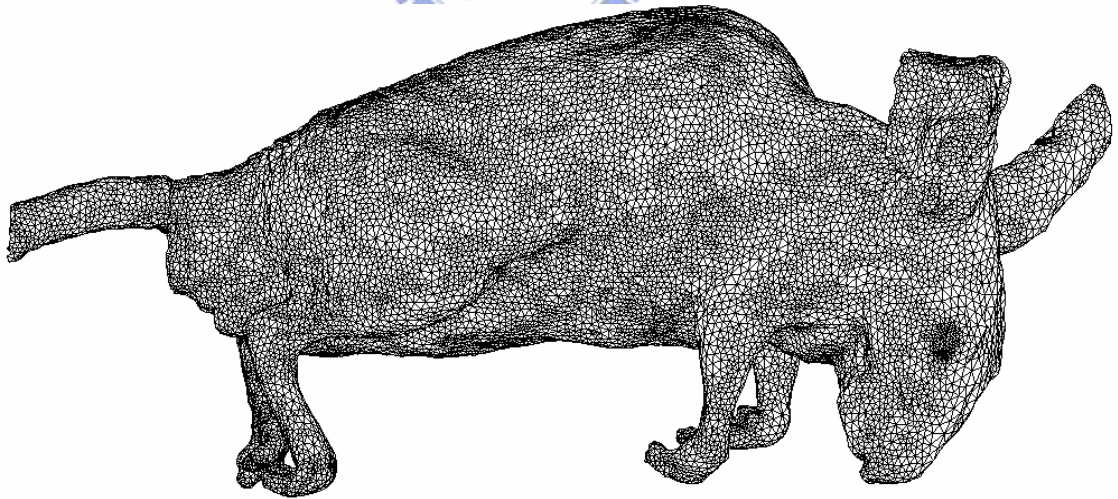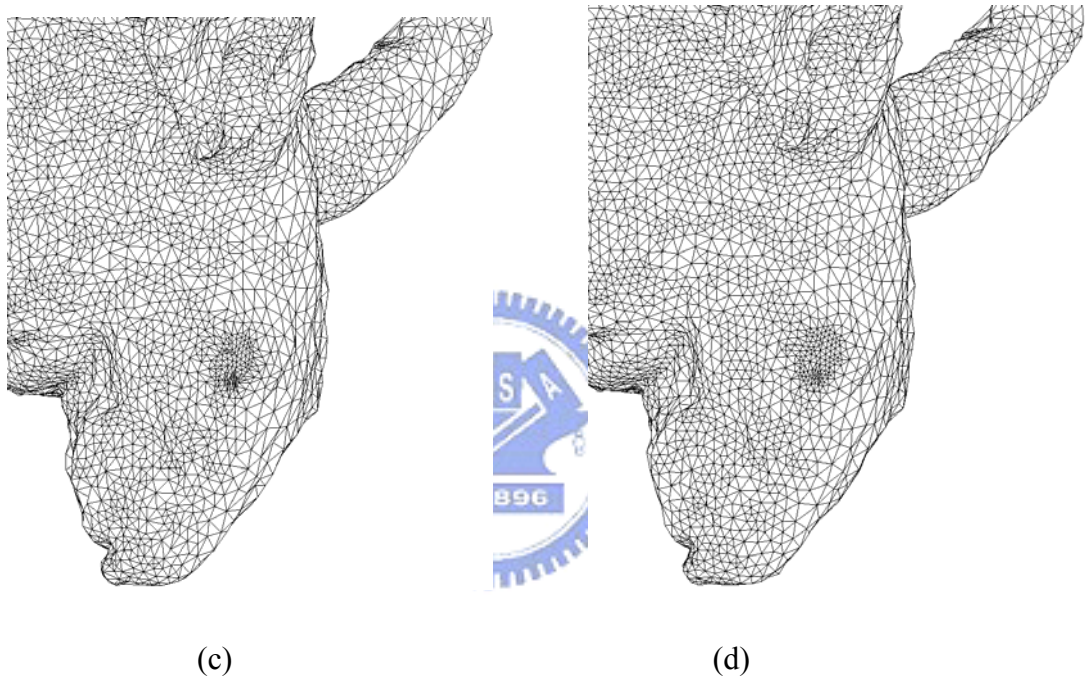
Fig. 4-11 Triangular surface mesh of rat: (a) Original surface mesh; (b) Surface mesh after smoothing; (c) Original surface mesh (enlarged); and (d) Surface mesh after smoothing (enlarged).

(a)

(b)

<center>(c)</center>

<center>(d)</center>
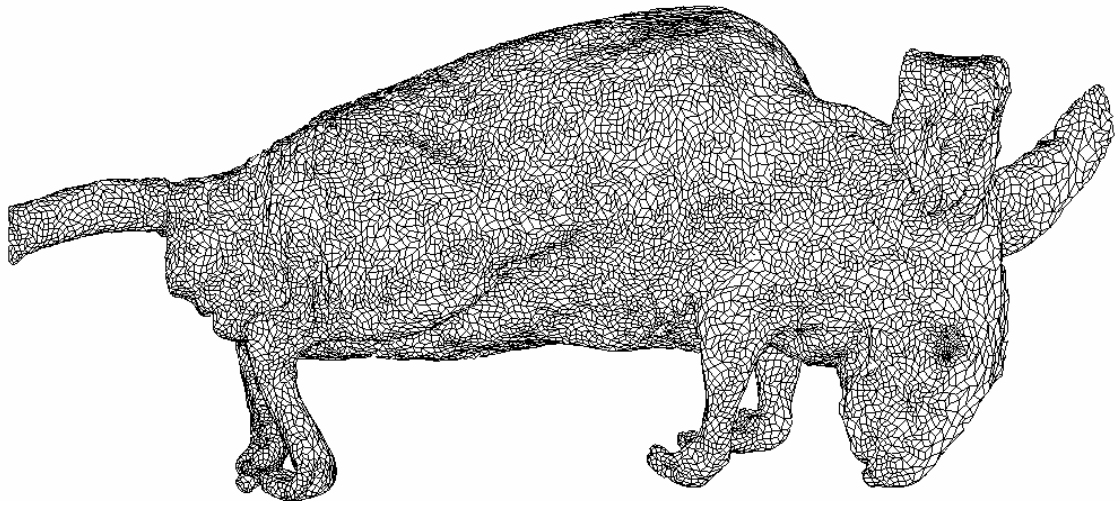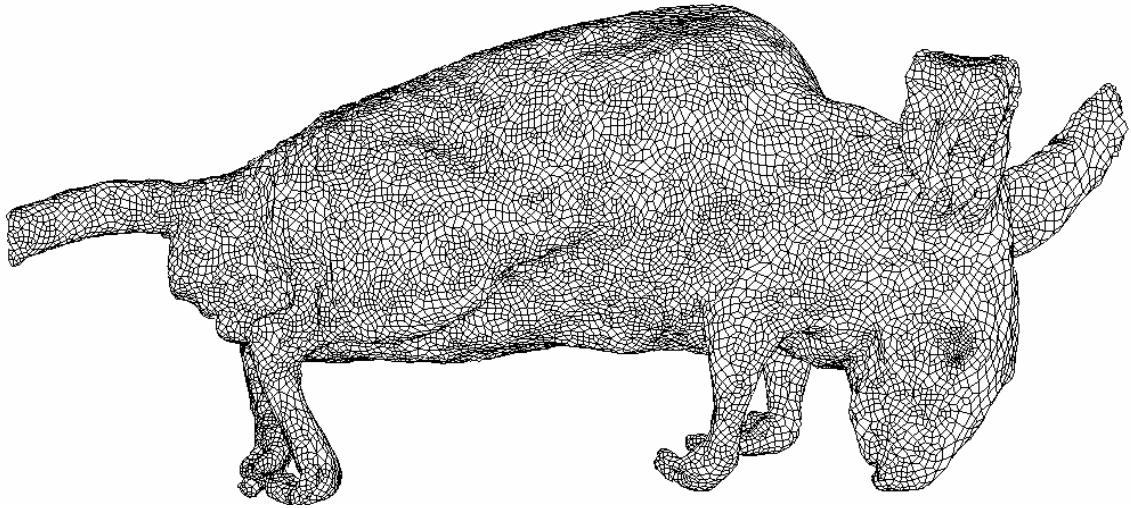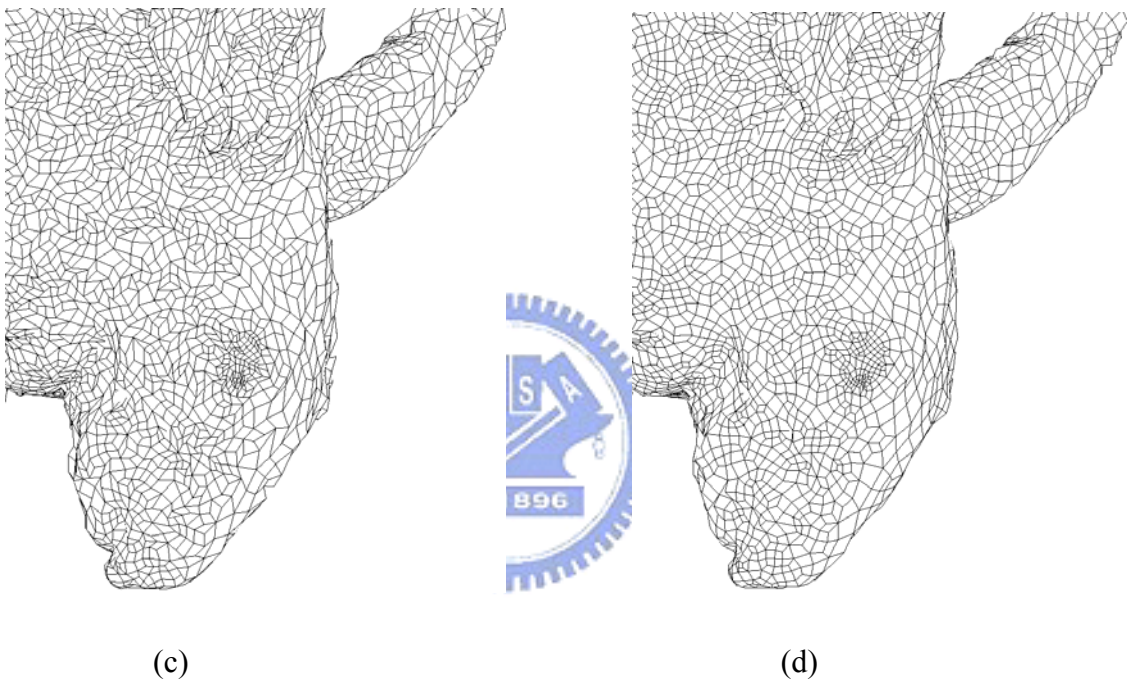
Fig. 4-12 Quadrilateral surface mesh of rat (a) Original surface mesh (b) Surface mesh after smoothing (c) Original surface mesh (enlarged) (d) Surface mesh after smoothing (enlarged).

Chapter 5. Pectus excavatum repairs

5.1 Pectus excavatum repairs

In 1949, Ravitch presented a technique of pectus excavatum repairing by using bilateral costal cartilage resection and sternal osteotomy [29]. It is a classic surgical repair of pecuts excavatum, which involves bilateral costal cartilage resection and sternal osteotomy technique. Fonkalsrud et al. [65] presented a highly modified Ravitch repair (HMRR), which was performed with minimal costal cartilage resection technique. As shown in Fig. 5-1, a transverse inframammary incision with upward curvature was made midway between the nipples, and a short vertical extension in the midline was made to expose the superior sternum. Short cautery incisions (1.0-1.5 cm) were made through the perichondrium of deformed costal cartilages adjacent to the sternum; a 1.0 to 1.5 cm incision was made laterally near or beyond the costochondral junction where the chest wall was at the highest level. Short segments of cartilage (1.0-1.5 cm) were resected medially and laterally from each of the deformed ribs. A transverse wedge osteotomy was made across the anterior table of the sternum at the desired level and then sutures were placed across the osteotomy. Finally, a thin stainless-steel bar was placed under the depressed sternum to elevate the sternum and attached to the appropriate rib on each side with fine wire (Fig. 5-2). Please refer to [25] and [65] for the details of this highly modified Ravitch repair.

In 1998, a minimal invasive pectus excavatum repair (MIRPE or Nuss procedure) was presented by Nuss *et al* [30]. In this procedure, one pre-bent metal bar (pectus bar) was placed under the depressed sternum thorough bilateral thoracic incisions to elevate the depressed sternum. The Nuss procedure performed a PE repair without costal cartilage resection and sternum osteotomy. Because the incisions were small (about 2 cm) [66] and were located on bilateral midaxillary line, the PE patients underwent the Nuss procedure obtained good cosmetic result and the Nuss procedure became an attractive option for PE repair.

5.2 Nuss procedure

In 1987, Dr. Donald Nuss, a pediatric surgeon at Children's Hospital of the King's Daughters in Norfolk, Virginia, developed a new technique for the correction of pectus excavatum, now known as the minimal invasive PE repair or Nuss procedure [30]. The Nuss

procedure performed a PE repair by inserting a pre-bent metal bar under the depressed sternum to correct the anterior deformation. As shown in Fig. 5-3, the pectus bar was bent to match a desired shape, which was decided by surgeon.

In a Nuss procedure, two lateral incisions were made on either side of the chest, which were located on bilateral midaxillary line. A clamp was passed through the bilateral thoracic incisions under the sternum to create a tunnel for the pectus bar. Then the clamp clipped a strand, which was tied to a pectus bar, to guide the pectus bar across the chest through the bilateral thoracic. The pectus bar was placed with the concave side anteriorly and then the bar was forcibly turned over to elevate the depressed sternum to the desired position [Fig. 5-4]. During the operation, a separate, small lateral incision was made to allow for a thoracoscope for direct visualization as the clamp and the bar were passed under the sternum. A lateral stabilizer plate was routinely placed on the left hand side of the pectus bar to secure to ribs [Fig. 5-5], and the right hand side of the pectus bar was secured to the lateral chest wall muscles. Finally, the incisions were closed and dressed, and the bar was hidden from the outside. The bar was left after 2 or more years, depending on the severity of the deformity and the age of the patients.

Complications of the Nuss procedure are uncommon. One of the frequent complications of the postoperative of this procedure is air in the chest (pneumothorax) and it usually requires no treatment besides some serious symptoms. The benefits of this procedure are shorter operating time (less than 90 minutes), low blood loss (less than 80ml), short hospitalization stay (4-5 days) and low rate of complications [65]. The inconvenience is that it need reoperation to leave the pectus bar after 2 or more years
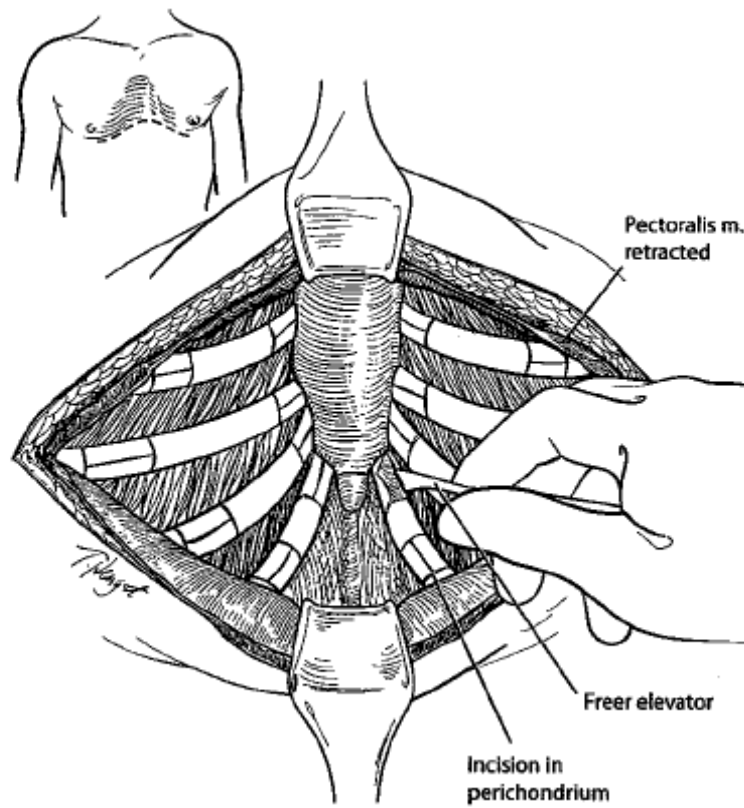
Fig. 5-1 A transverse inframammary incision with upward curvature was made midway between the nipples, and a short vertical extension in the midline was made to expose the superior sternum [65].
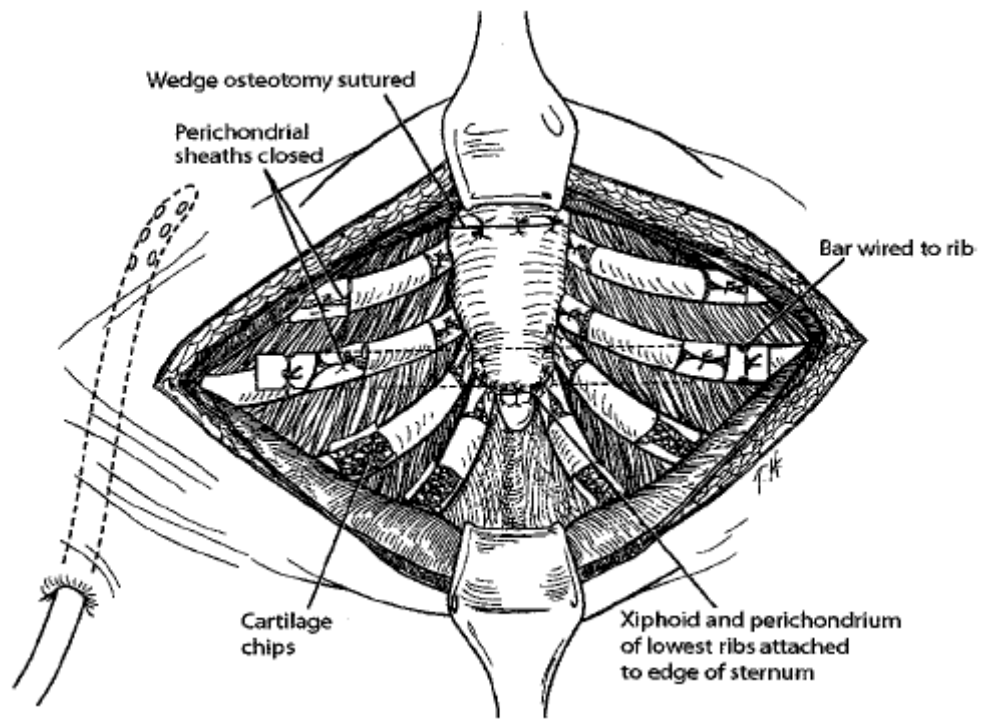
Fig. 5-2 A thin stainless-steel bar was placed under the sternum to elevate the sternum and attached to the appropriate rib on each side with fine wire [65].

Fig. 5-3 The pectus bar is pre-bent to match a desired shape [66].
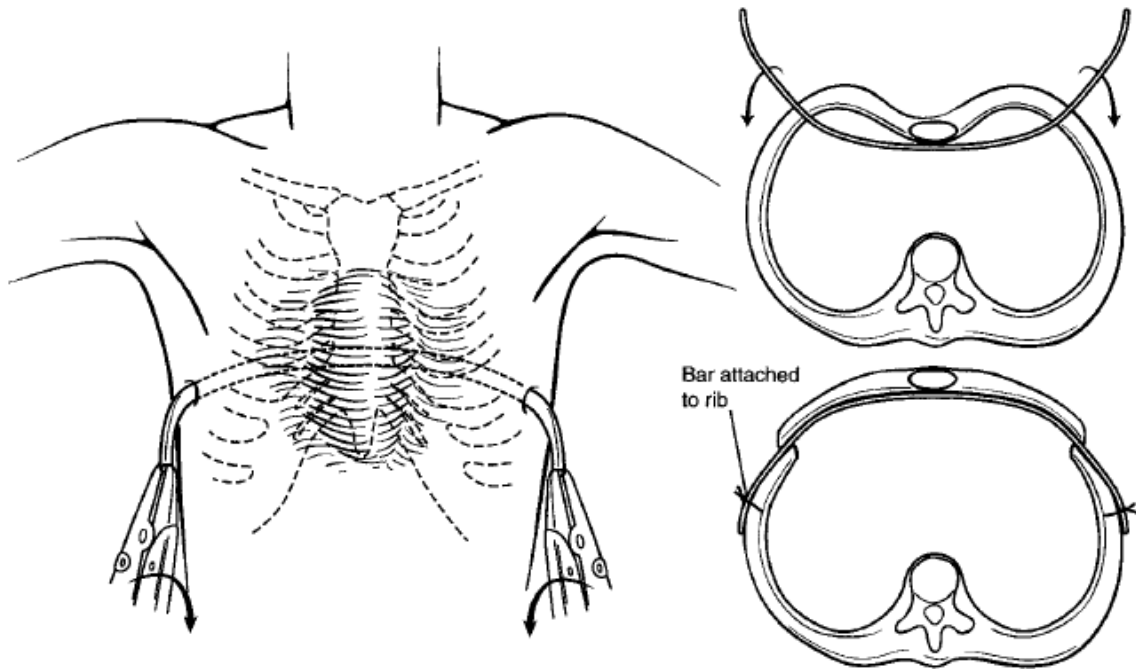
Fig. 5-4 Nuss procedure [25].
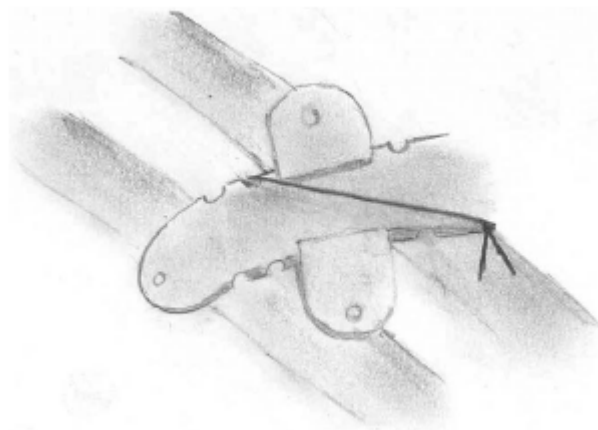
Fig. 5-5 Pectus bar is secured to ribs with a stabilizer plate [67].

Chapter 6 Finite element analysis and thoracic volume measurement

6.1 Patient-specific finite element models

Awrejcewicz and Łuczak presented a simplified finite element model, which contained rib, sternum, costal cartilage and Nuss implant, to investigate stress distributions on the human thorax for an impact load [37]. In their research, a force of 5000 N, which was generated by a car-to-car frontal collision, was applied to the center of sternum. However, according to the ref. [39], the force requirement to raise the sternum of pectus excavatum, who were males and aged 5-17 years, was only 181±48.3 N. The impact force applied to the sternum was 27.62 times the force to raise the sternum of pectus excavatum. Moreover, since the biomechanical analysis of the PE patients after the Nuss procedure was not been presented before, there did not exist confirmed simplified finite element model can be used to perform this FEA work. In order to confirm the simulation results, we developed the finite element biomechanical analysis with five patient-specific finite element models and the simulated results showed that their biomechanical changes after the Nuss procedure were similar.

Five symmetric type of PE patients [34] were carefully chosen to eliminate the factors due to asymmetric configuration of the chest wall for our analysis. Their personal information was shown in Table 5-1. In the previous work [42], the rib cage model contained sternum, ribs, costal cartilages and vertebral column. According to the clinical observation, the vertebral column was not immediate deformation after the Nuss procedure. In order to reduce the computational loading, the created rib cage model contained the ribs, costal cartilages and sternum, and the vertebral column was not considered here, which was similar to ref. [37].

For the reconstruction of the rib cage model, there is one serious problem occurred that the image of costal cartilage was indistinct on CT slices. As shown in Fig. 6-1 (a), the automatic segmentation results, which were segmented by the AMIRA [62], contained many islands and the segments of costal cartilage were incomplete. In order to overcome this, a semiautomatic procedure was developed to reconstruct the rib cage model. First, the CT slices were imported into AMIRA and the original segments of the rib, sternum, and costal cartilage were labeled automatically by assigning respective grayscale values. Then, the islands were eliminated and the segments of costal cartilage were modified manually (Fig. 6-1(b)). Since the image of costal cartilage was indistinct, the modifications of segments relied on

professional experience of researchers. Therefore, it is not suitable to perform a great cases simulation and we will keep on working to overcome this problem. After the segment modification, the rib cage model was reconstructed by connecting these segments and the finite element models were generated with tetrahedral element by employing the AMIRA. Due to the surface mesh of the rib cage model was coarse, the surface function, which was reconstructed based on the triangular surface elements, was not suitable to perform a surface mesh smoothing. The MGA surface mesh smoothing procedure [3] was not adopted to improve the surface mesh quality of rib cage model.

A convergence test was performed to confirm the simulated accuracy of mesh by comparing the simulated results of six rib cage meshes (Table 6-2). The convergence criterion is that the difference of the corrected displacement of the end of the sternum was less than 1%. The convergence test curve was shown in Fig. 6-2, and the final choice was that the finite element model consisted of approximately 320,000 tetrahedral elements.

6.2 Finite element analysis

Five FEA models were created to perform the biomechanical analysis of the PE patients after the Nuss procedure. The material properties of bone and cartilage were based on the work of Yang and Wang [68]. An elastic modulus of 11.5GPa was chosen for the ribs and sternum, while 12.25 MPa was assumed for the pectus costal cartilages, which is about half of the value for normal cartilage, as suggested by Feng *et al.* [69].

For the Nuss procedure, the concave side of the pectus bar was placed under the sternum through bilateral thoracic incisions and then forcibly turned around to raise the depressed sternum. After the sternum was raised, several forces were generated on the chest wall and on the pectus bar. As shown in Fig. 6-3, the pectus bar provided an elevating force (Fe) to raise the depressed sternum and a reaction force (Fr) was generated on the contact area of pectus bar. Simultaneously, two support forces (Fs) were applied to the pectus bar around the two intercostals exits to preserve the equilibrium of forces generated on the pectus bar. Furthermore, the intercostals muscle, located on the two exits, supplied support forces (Fs) to the pectus bar and the forces were transmitted to the ribs above and below the exits, called rib support forces (Fsr). Although these forces can not be measured directly from the operative patient during a Nuss procedure, it is reasonable to assume that they are equally distributed and the total of the rib supporting forces should be equivalent to the elevating force, i.e. Fe = 2 Fs = 4Fsr. The locations of Fe and Fsr were observed during the operation. As shown in Fig.

6-4, the forces Fe and Fsr were applied to the corresponding positions and the displacement of the joints (head and tubercle of rib [70]) between the ribs and the spine was assumed to be rigid. Moreover, the actual upward displacements of the end of the sternum were measured from each patient's CT scan which was taken before the Nuss procedure and chest X-ray films after the Nuss procedure. These displacements of the five PE patients were shown in Table 6-1.

Based on these assumptions, the FEA procedure was developed using ANSYS 9.0 software (ANSYS Inc.) and the finite element models were meshed with ANSYS solid 185 tetrahedral element. The large displacement static solver on ANSYS was adopted due to the large correcting displacements of the finite element models. Since the forces of Fe and Fsr can not be measured directly, each finite element model was analyzed several times with different force sets to obtain the equivalent correcting displacement of the end of sternum.

6.3 Thoracic volume measurement

Lung volume increase of PE patients after the implant of Nuss procedure is an interesting problem. According to clinical observation, the lung volumes of PE patients are increased after a Nuss procedure. However, it is difficult to estimate the lung volume variation due to that the pectus bar will seriously degrades image quality of CT, particularly near the surface of the bar. In order to investigate the pulmonary function improvement of PE patients after a Nuss procedure, the lung thoracic volume change is a significant index.

In this thesis, we created five simplified rib cage models, which consisted of ribs, sternum and costal cartilages, to perform the finite element biomechanical analysis of PE patients. Since these simplified models did not contain the lung model, the lung volume could not be measure directly. In order to treat this, we provided an alternative way to estimate the lung volume by measuring the intrathoracic volume or the thoracic volume. According to human anatomy, the lungs are located on the lateral sides of the thoracic cavity, above the intrathoracic (Fig. 6-5) [71]. It is reasonable to assume that the increased intrathoracic volume is filled principally with lung. Therefore, the increase of lung volume can be estimated by measuring the increase of intrathoracic volume.

In this thesis we present two methods to measure the intrathoracic volume and thoracic volume. The first method is intersection method and the other is surface approximation method. The intersection method was used to measure the intrathoracic volume and the surface approximation method was used to measure the thoracic volume.

6.3.1 Method 1: intersection method

As shown in Fig. 6-4, the finite element models presented here were constituted only ribs, sternum and costal cartilage, the intrathoracic volume can not be measured directly from this model. To overcome this problem, we developed a program to compute the intersection between a set of planes and the finite element model. These planes are parallel and with equidistance (about 2.6mm) along the longitudinal axis of the model (Fig. 6-6), from the apex of the lung to the dome of the diaphragm. The intersection points in the plane were drawn in a picture (512×512 pixels). Fig. 6-7 shows the intersection points between the plane and the pre- and post-operation finite element models. These pictures were then imported into AMIRA to establish the intrathoracic volume. Finally the volume difference between the two models was calculated. The calculated volume difference is estimation to the final total difference of the intrathoracic volume.

6.3.2 Method 2: surface approximation method

Surface approximation is a common procedure to generate a surface to approximate a set of sampling points [72-80] and there is a brief introduced by Fasshauer and Schumaker [78]. Generally, surface approximation is used to generate a surface to approximate all of the given point set. In this thesis, we present a particular application that the approximated surface is like the skin envelope to lay on the outside of a human rib cage model, which is constituted with the ribs, sternum, costal cartilages and vertebral column. The approximated surface was constructed by employing the C^1 continuous Ferguson's bicubic surface [81].

In this surface approximation procedure, a cylinder surface, which was consisted of $n\times m$ Ferguson's bicubic patches, was first constructed to surround the rib cage model along the longitudinal axis of this model (Fig. 6-8). The parameters n and m represented the number of patches along the longitudinal axis and along the circle of this model respectively, and the total number of the key-points was $(n+1)\times m$. Then the cylinder surface was converged by moving the key-pints along the radial line toward the central axis to approximate the rib cage model. The flow chart of the surface approximation procedure was shown in Fig. 6-9.

As shown in Fig. 6-9, the surface approximation procedure was an iterative process that each key-point was moved with a decided step along the radial line toward the central axis. As the rib cage model was cut in by the approximated surface, this key-point was returned to the

preceding position and held. After all of the key-points were held, the step was reduced and then the convergence procedure was restart again until converged. During the surface approximation procedure, a distance detecting process was used to detect the distances between the approximated surface and the sampling points. In this process, the sampling points were projected to the approximated surface along the radial line and the intersected points of the radial line and the approximated surface were calculated by adopting the Newton-Raphson method [82].
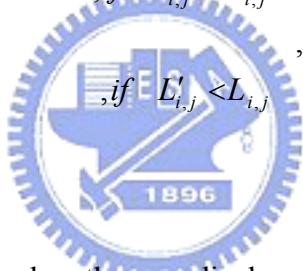
As shown in Fig. 6-4, the gapes between the ribs and the hole near the abdominal cavity were large and there was not sampling point located there. This status resulted in a serious concave shape of approximated surface. According to the observation of a human body, the surface near the abdominal cavity is flat or convex. In order to generate a skin envelope-like approximated surface, several additional treatments were applied to overcome these problems. For some key-points located outside the abdominal cavity, there was not sampling point to bound them during the surface approximation procedure. To treat this problem, an additional treatment was applied as following: To detect these singular key-points, each surface patch was divided into four regions uniformly. As shown in Fig. 6-10, there was not sampling point located in the regions surrounded the key-point I and the key-point I was marked to be a singular key-point. Then a connection was created between the key-point I and its closest key-point ($I - 1$), which was not marked, along the circle. As the key-point $I - 1$ was bounded during the surface approximation procedure, the key-point I was bounded simultaneously. The approximated results showed that this treatment can avoid the concaves generated on the abdominal cavity.

Moreover, the number of patches plays a crucial role in surface approximation. In general, larger number of patches relates to higher accuracy of approximated result. However, since the gapes between the ribs and the hole near the abdominal cavity were large, the number of patch should be carefully chosen to avoid the generation of an inappropriate approximated surface. According to our approximated results, the dense patches will result in a skinny surface and the sparse patches will induce a poor accuracy of the approximated surface. Figure 6-11(a) showed a skinny surface consisted of 26×28 Ferguson's patches and Fig. 6-11(b) showed an approximated surface consisted of 6×10 Ferguson's patches.

As described above, a denser surface patches will result in a skinny surface. The causes were that some key-points were located on the gapes of intercostal, and they were fallen into the intercostals during the surface approximation procedure. Even the number of patches was reduced to 16×16, there were several incorrect concaves generated on the approximated

surface (Fig. 6-12(a)). According to the clinical observation on the PE patients, the concave shape was appeared on the anterior chest wall (around the end of sternum) and the shape near the intercostals was flat along the longitudinal axis. Therefore, we applied a smoothing process to adjust the radial distance between the key-points and the central axis.

For this smoothing process, all of the key-points were smoothed excepte the key-points located on the upper plane, lower plane and around the end of the sternum. The smoothed key-points called selected key-points were smoothed with their neighbor key-points along the longitudinal axis, and their height (z-coordinate) was not varied during the smoothing process. The smoothing process was performed as following: Let $L_{i,j}$ be the perpendicular distance between the original position of $P_{i,j}(x,y)$ and the central axis ($O(x,y)$). The new distance $L'_{i,j}$ between the central axis and the new position $P'_{i,j}(x,y)$ was calculated as

$$L'_{i,j} = \begin{cases} \dfrac{\displaystyle\sum_{I=i-1}^{i+1}\left|P_{I,j}(x,y)-O(x,y)\right|}{3} & ,if \quad L'_{i,j} > L_{i,j} \\[4mm] L_{i,j} & ,if \quad L'_{i,j} < L_{i,j} \end{cases} \quad , i = 2, \text{n and } j = 1, \text{m} \qquad (6\text{-}1)$$

The key-point $P_{i,j}$ was shifted when the new displacement $L'_{i,j}$ was longer than the original displacement $L_{i,j}$ to avoid the approximated surface to cut in the rib cage model. Since the smoothing process was applied before the surface approximation procedure, this adjustment will not affect the accuracy of the approximated result. Figure 6-12(b) showed that the smoothing process was beneficial to reduce the generation of incorrect concaves on the approximated surface.

After the approximated surface was generated, the following process was to measure the thoracic volume. According to Mckinley and O'Loughlin [70], the lungs are located on the lateral sides of the thoracic cavity and ranged from the intrathoracic to the apex. The apex is located near the first thoracic vertebra and the intrathoracic is near the end of the sternum. Therefore, the measurement of thoracic volume was ranged from the end of sternum to the first thoracic vertebra.

For the measurement of thoracic volume, the upper and lower bound of the measurement range were assumed to be a plane. According to Faux and Pratt [81], the volume of a closed

parametric surface can be calculated as a volume of pyramid. As shown in Fig. 6-13, the surface area of the element *ABCD* can be calculated as

$$A = \iint \left(\frac{\partial r}{\partial u} \times \frac{\partial r}{\partial v} \right) du dv \qquad (6\text{-}2)$$

Since the volume of the pyramid is equal to one third of the surface area times the height, the volume *V* subtended by *ABCD* at the origin *O* is approximately

$$V = \frac{1}{3} \iint_R r \cdot \left(\frac{\partial r}{\partial u} \times \frac{\partial r}{\partial v} \right) du dv \qquad (6\text{-}3)$$

where *R* is the region of the *u, v* plane. Moreover, the upper and lower planes were divided into several triangular elements and the volume subtended by each element at the origin *O* was calculated as a pyramid directly.

6.4 Results

6.4.1 Finite element analysis results

Five finite element models of PE patients were analyzed by employing the ANSYS. Since the elevating force and support forces can not be measured from the operative PE patients directly, each model was simulated several times with different force sets. The first set of elevating force was 20 N and increased with 20 N per time until the displacement of the end of sternum was equivalent to the corrected displacement. The simulation results were shown in Table 6-1 and Fig. 6-14 shows the relationship between elevating force and the displacement of the end of sternum. Fonkalsrud et al. [38] reported that 4 children with pectus who are younger than 11 years old will require a force about 15.3 pounds (68.058 Newtons) to raise the sternum to the normal position. The force required in correction of Pectus excavatum was also measured by Weber et al. [39]. For male patients, aged 5-17 years, the force was 181 ±48.3Newtons. The amount of force in our simulation is quite similar to these two studies.

As shown in Fig. 6-14, the increasing of displacements are alleviative after the elevating forces are greater than 60N. It may be an import information for the surgeon to weigh the correcting displacement for the PE repair. Figure 6-15 shows the deformation with different

elevating force (patient one). Figure 6-16 shows the stress distribution of the first model under a load of 140 N. It is apparent that there are greater stresses generated on the back and concentrated on the third through seventh ribs, near the vertebral column. It is an import phenomenon that it may be the cause of some complications for the PE patients underwent a Nuss procedure, such as back pain [67,83] and thoracic scoliosis [32].

Figure 6-17 shows the simulation result of the strain of the first model. The greater strain was focused on the third to seventh cartilages, especially at the junction with the sternum and ribs, bilaterally. Figure 6-18 shows the variations of strain along the right fifth costal cartilage and rib. In Fig. 6-18, the position is represented the sidelong distance from the center of sternum to the right fifth rib. The measured points were selected from the sternum (0~0.95 cm), the right fifth costal cartilage (0.95~6.35cm) and part of the right fifth rib (6.35~7.46cm). According to the measured data, the maximum strain occurred on sternum and rib is 0.0005 and the minimum strain occurred on costal cartilage is 0.034. It is apparent that the variation of strain on the two joints (sternocostal joint and costochondral joint [70]) present severe variations. The simulation results of the stress and strain distribution were similar in other patients, as presented in Table 6-1.

Since there is no removal of any costal cartilage during a Nuss procedure, the elevating force applied to the sternum will generate a corresponding stress that is conducted through the sternum, cartilage, and ribs to the entire chest wall. As shown in Fig. 6-17, the greater strain is occurred on the costal cartilage and focused on the joints of the cartilage with the corresponding bony rib and sternum. This result matched our expectations. However, as shown in Fig. 6-16, there are greater stresses generated on the back and concentrated on the third through seventh ribs bilaterally, near the vertebral column. It is important that the strain of costal cartilage was greater than the strain of ribs, but the generated stress on the ribs was greater than costal cartilage. In Fig. 6-17, the greatest strain on the costal cartilage was 0.93, while the strain on the bony rib was about 0.01. Thus, the strain on the costal cartilage was 93 times higher than that on the rib. The elastic modulus of a rib and costal cartilage are 11.5 GPa and 12.25 MPa, respectively, *i.e.*, the elastic modulus of the rib is 938 times higher than that of the costal cartilage. Based on the fundamental elasticity equation $\sigma = E\varepsilon$, where σ, E, and ε are the stress, modulus of elasticity, and strain of the mechanical parts under study respectively [84], it makes sense that greater stress was generated on the rib of the patients than on the cartilage.

Moreover, the generated stress on the chest wall of postoperative PE patients may induce some complications. If the transmitted stresses were imbalance, it may be induce some

complications, such as back pain [67,83] and thoracic scoliosis [32]. If the pectus bar was implanted into a wrong position, slipped or flipped, the imbalance state may be occurred.

6.4.2 Thoracic volume measurement results

1. Intersection method

Five finite element models were analyzed to obtain their corrected shapes after the Nuss procedure and the finite element models were employed to measure the variation of lung volume. As described above, the lung volume was estimated by measuring the increase of intrathoracic volume. Figure 6-19(a) shows the intrathoracic volume of the first patient before the Nuss procedure. Table 6-1 and Fig. 6-19(b) shows the intrathoracic volume after the Nuss procedure. Figure 6-20 shows the measured results of the five patients and the intrathoracic volume of the five patients are increased about 2.72% to 8.88%. We believe that the increased volume can relax the pressure of the heart and lung, and improve the PE patients' breath behavior substantially. In Fig. 6-20, the increasing of volumes is alleviative when the elevating forces are great than 60N and it is similar to Fig. 6-14. It may be an import signal for the PE patients repair.
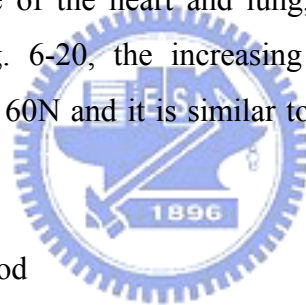
2. Surface approximation method

One 7 years pectus excavatum patient, the second patient on Table 6-1, was used here to measure her thoracic volume changes before and after a Nuss repair. The approximated surface was consisted of 16×16 Ferguson's bicubic patches and the approximated results are shown in Fig. 6-21 and Fig. 6-22. Figure 6-21(a) shows the rib cage model of before the Nuss procedure. In Fig. 6-21(b), the approximated surface of preoperative model, the funnel chest is appeared around the end of sternum and it is similar to the PE patients. The thoracic volume of the preoperative model was measured as Fig. 6-21(c) and the thoracic volume is measured to be 1885.809cm3. Figure 6-22(b) shows the approximated surface of postoperative model (Fig. 6-22(a)) and the thoracic volume of the postoperative mode was estimated to be 2129.294cm3 (Fig. 6-22(c)). Therefore the thoracic volume of the postoperative PE patient is increased about 12.91%.

As shown in Fig. 6-21(b) and Fig. 6-22(b), the approximated surfaces are smooth but there are several incorrect concaves appeared near the top and the foot of the models. The

generation of the incorrect concaves is due to the great holes around the abdominal cavity and above the sternum. The approximated results indicate that it needs more treatments to improve the approximated results.

In this thesis, we present two methods to measure the intrathoracic volume and thoracic volume of pre- and postoperative PE patients. According to the measurement results, the intrathoracic volume and thoracic volume of the second patient were increased about 5.05% and 12.91% respectively. It is a huge difference between the measured results. The cause of this error is that the approximated surface does not fit the rib cage model very well. It has room to improve.

Table 6-1 Five pectus excavatum patients information.

	Case 1	Case 2	Case 3	Case 4	Case 5
Sex/Age	*M/8	*F/7	M/7	M/6	M/5
Pectus Index	5.3	4.7	5.2	3.7	3.6
Elevation of the end of sternum (cm)	4.47	3.40	3.99	3.54	3.75
Simulation results:					
1.simulation displacement of the end of sternum (cm)	4.49	3.43	4.00	3.55	3.79
2.Loading force at sternum end (N)	140	120	190	80	70
3. **Max. stress (MPa)	43.5	90.6	33.25	37.7	54.5
4. Max. strain	0.93	1.20	1.04	0.65	0.59
5. Increasing volume of intratoracic (cm^3)	89.98	54.63	29.76	54.24	107.04
6. Increasing volume of intrathoracic (%)	6.09	5.05	2.72	4.43	8.88

*M:male F:female

** Max.: Maximum

(a)

(b)

Fig. 6-1 Segment on AMIRE: (a) automatic segments and (b) modified segments.

Table 6-2 Corrected displacement of six rib cage meshes.

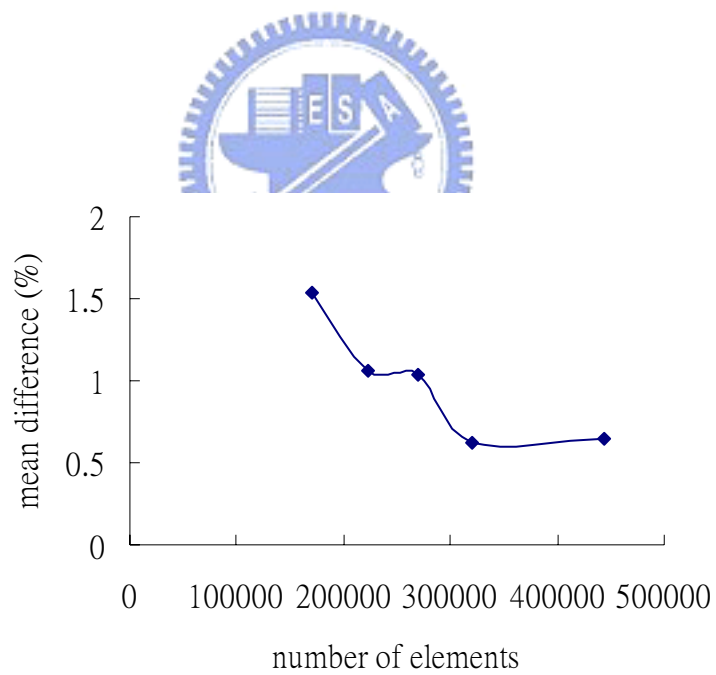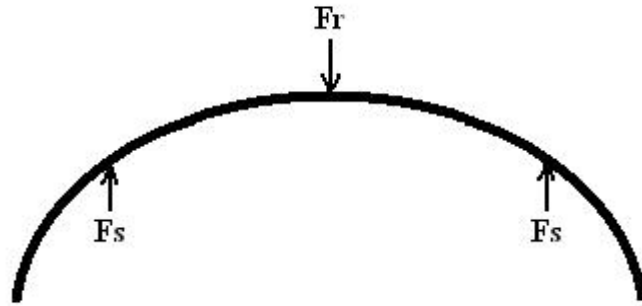| Number of elements	97939	170660	223522	269163	320519	443470
Corrected displacement	4.304	4.370	4.417	4.462	4.490	4.519
Mean difference (%)		1.5381	1.064	1.035	0.619	0.649

Fig. 6-2 Convergence test.

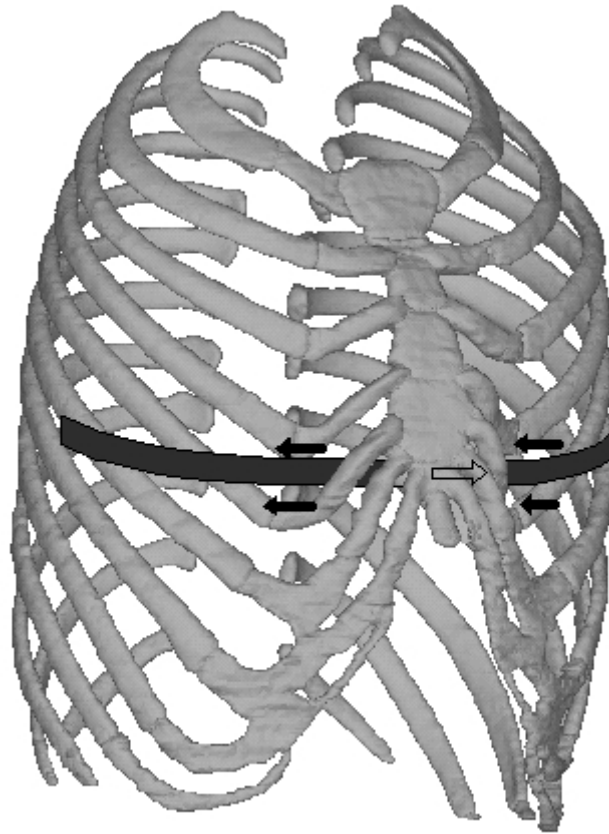Fig. 6-3 Reaction forces applied to a pectus bar.

Fig. 6-4 Boundary conditions of a FEA model.

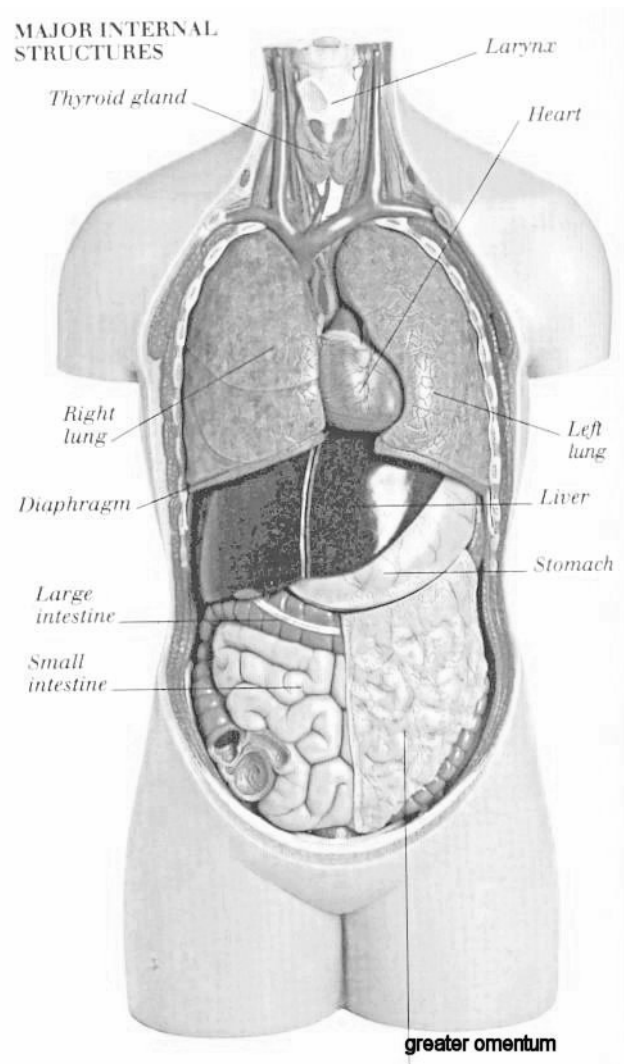Fig. 6-5 Major internal structures of human [71].
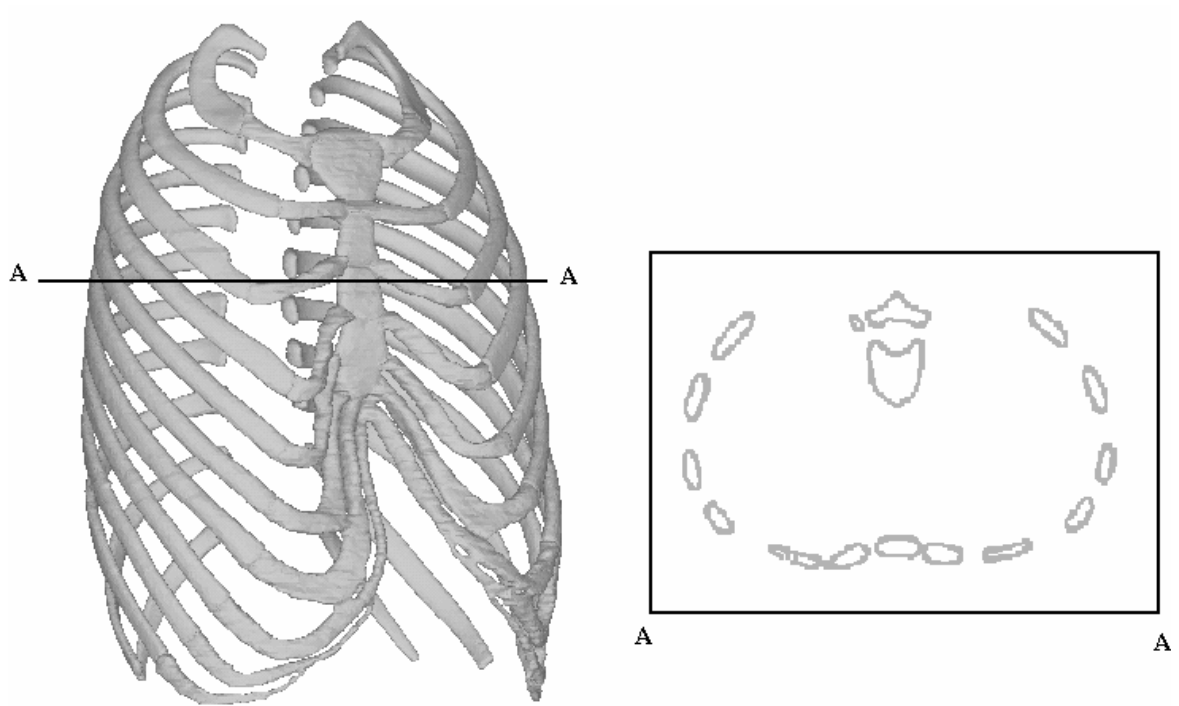
Fig. 6-6 Cutting plane.

(a)

(b)
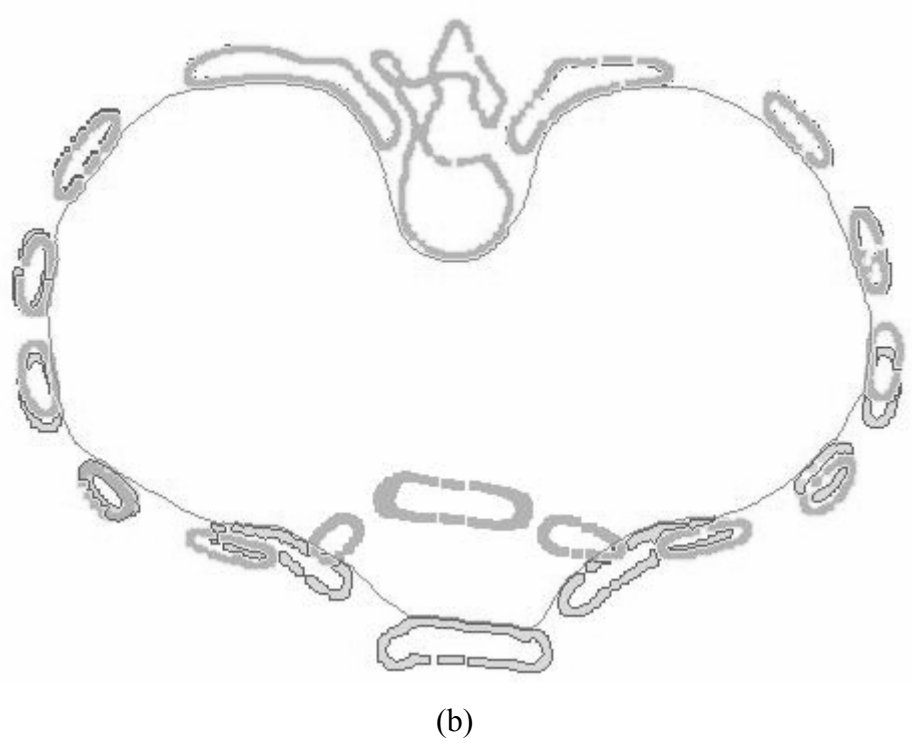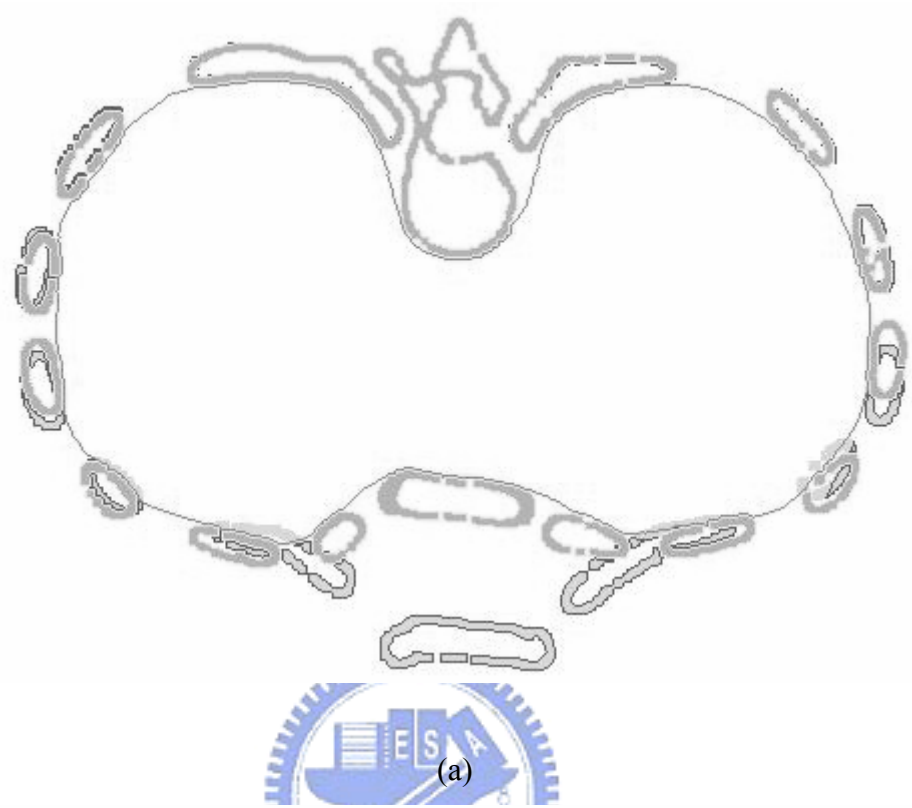
Fig. 6-7 Segment of intratoracic volume: (a) original and (b) deformed.

Fig. 6-8 Original cylinder.
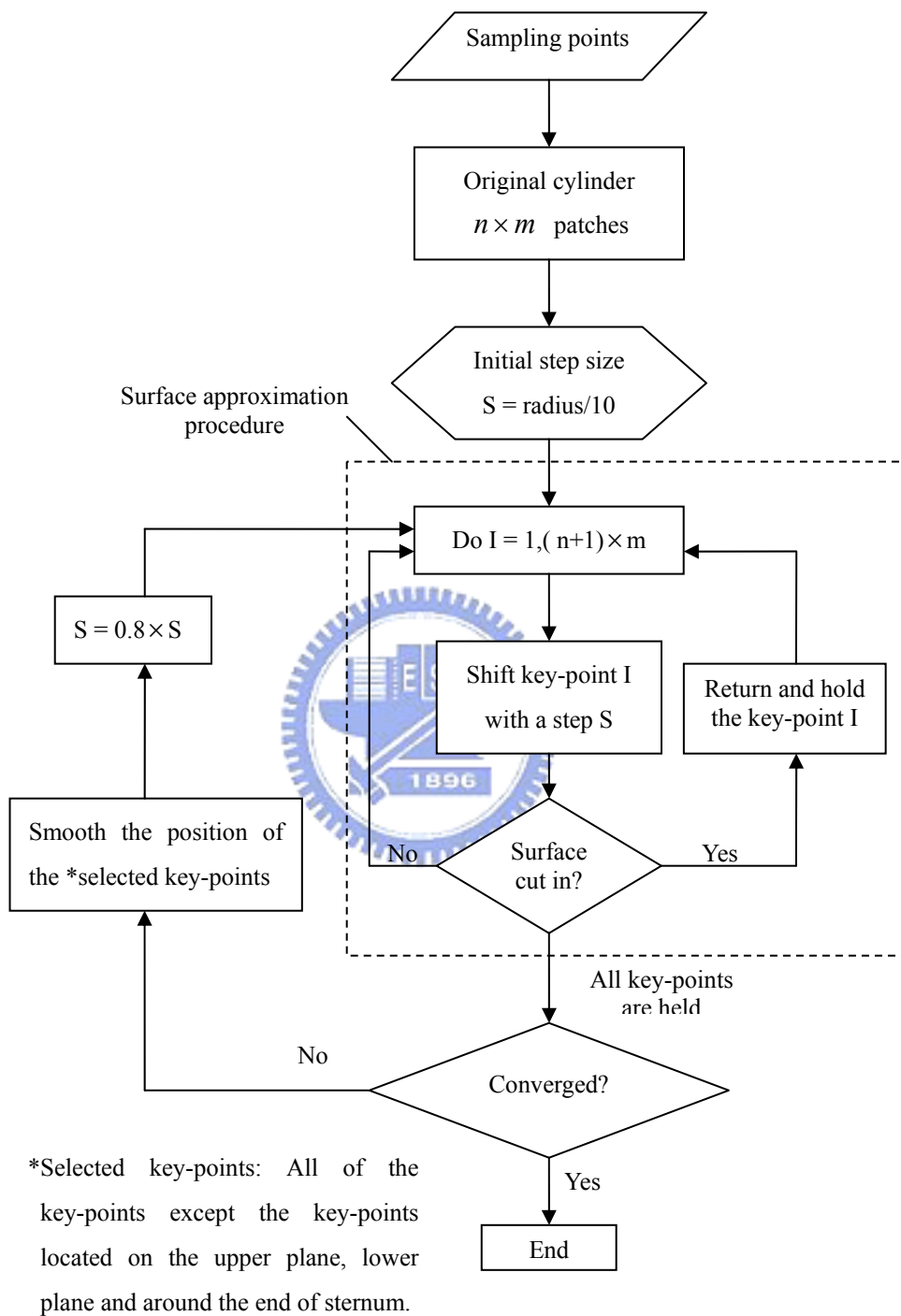
Fig. 6-9 Flow chart of surface approximation procedure.

The flowchart contains the following elements:

Sampling points

Original cylinder
$n \times m$ patches

Initial step size
S = radius/10

Surface approximation procedure

Do I = 1,(n+1)$\times$m

S = 0.8$\times$S

Shift key-point I with a step S

Return and hold the key-point I

Smooth the position of the *selected key-points

Surface cut in?

No   Yes

All key-points are held

Converged?

No   Yes

*Selected key-points: All of the key-points except the key-points located on the upper plane, lower plane and around the end of sternum.

End

Fig.6-10 Singular key-point identification.
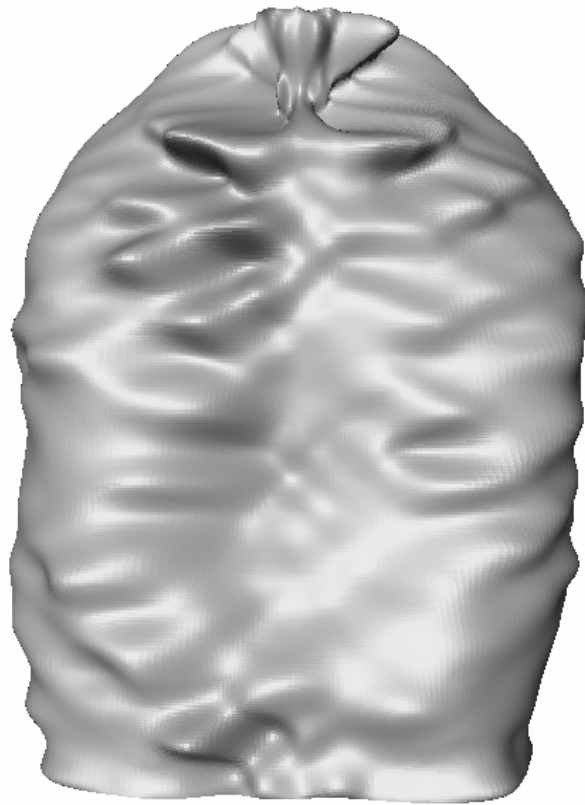
(a)
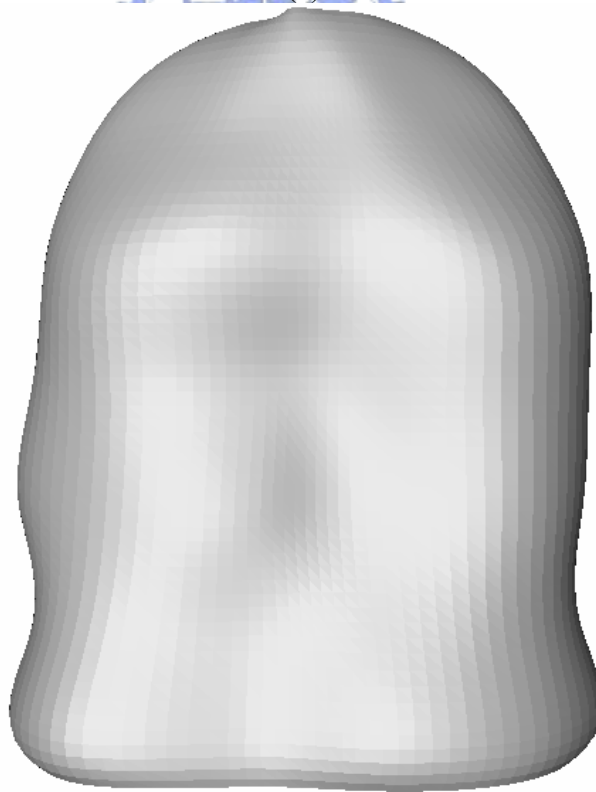
(b)

Fig. 6-11 (a) Skinny surface with 26×28 patches (b) 6×12 patches.
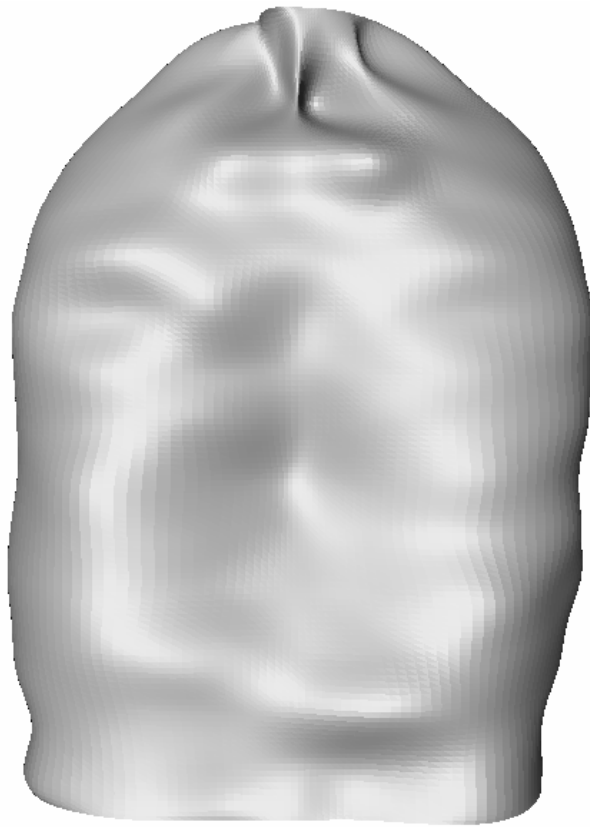
(a)
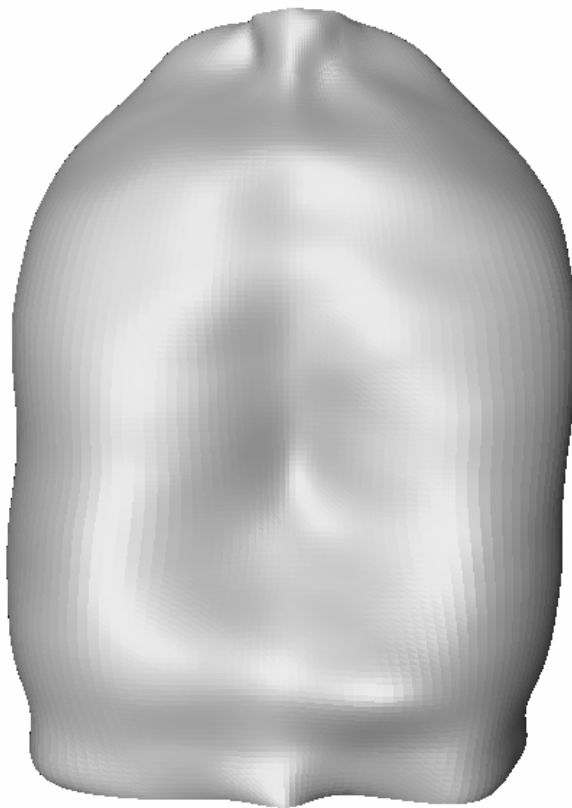
(b)

Fig. 6-12 Approximated surface consisted of 16×16 Ferguson's bicubic patches
(a) without smoothing (b) smoothing.
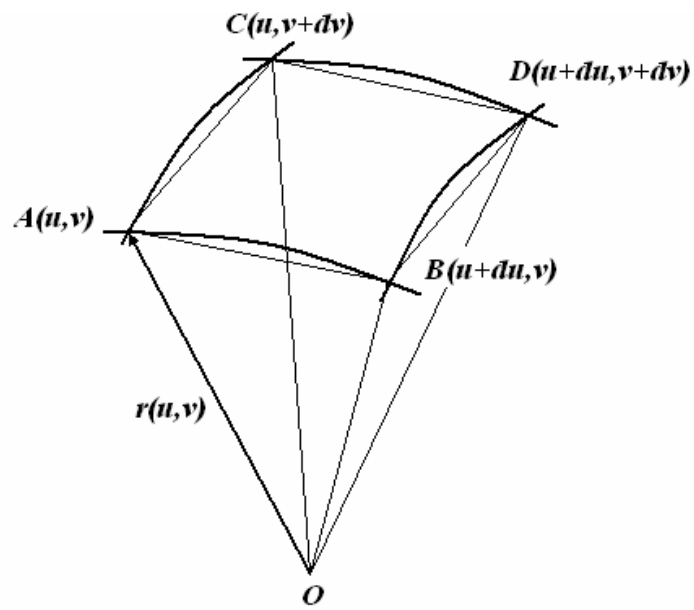
Fig. 6-13 Volume calculation of a pyramid.
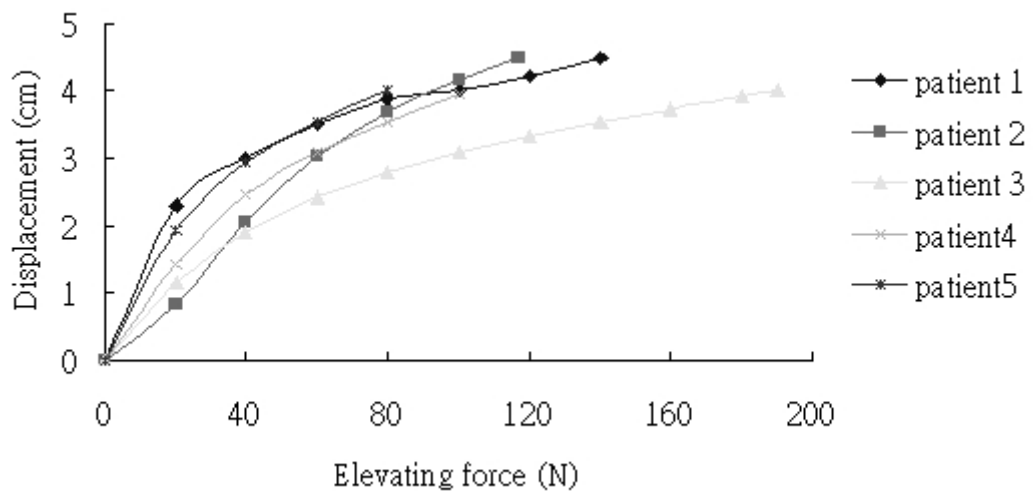
Fig. 6-14 The relationship between elevating force and the

displacement of the end of sternum.

Force:	40N	80N	120N	140N
Max. dis.:	2.30cm	3.50cm	4.21cm	4.49cm
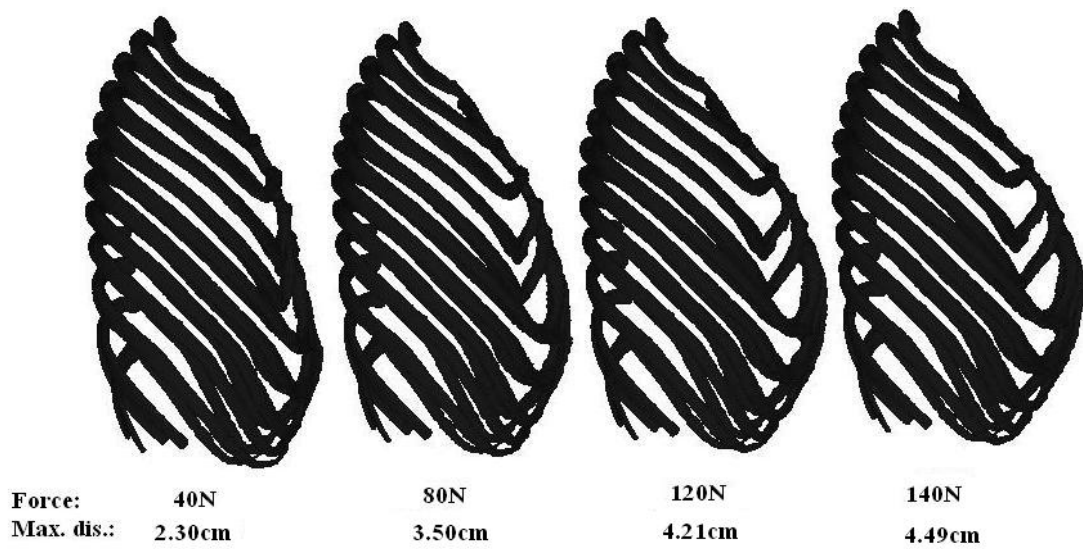
Fig. 6-15 Deformation with different elevating force (patient one).
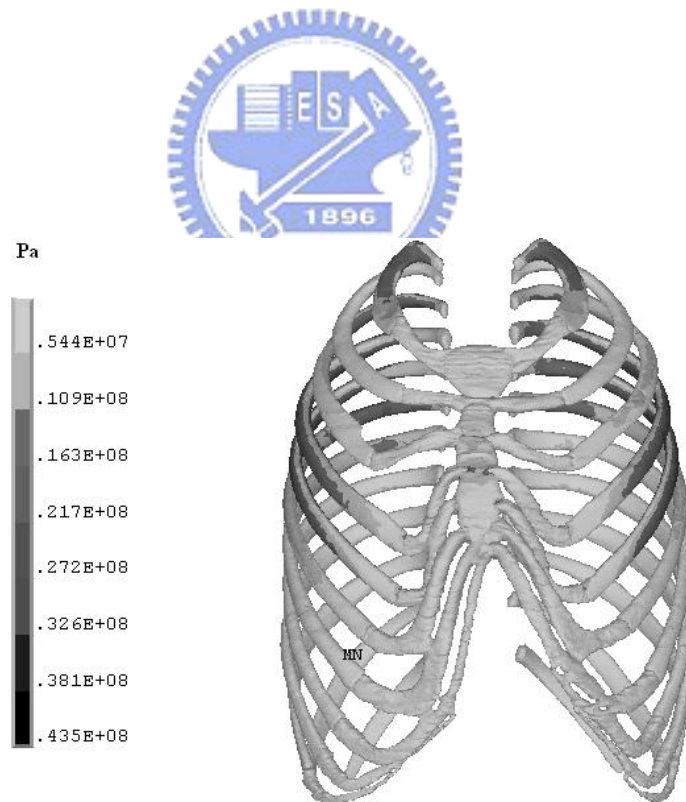
Fig. 6-16 Stress distribution of patient one with an elevating force 140N.
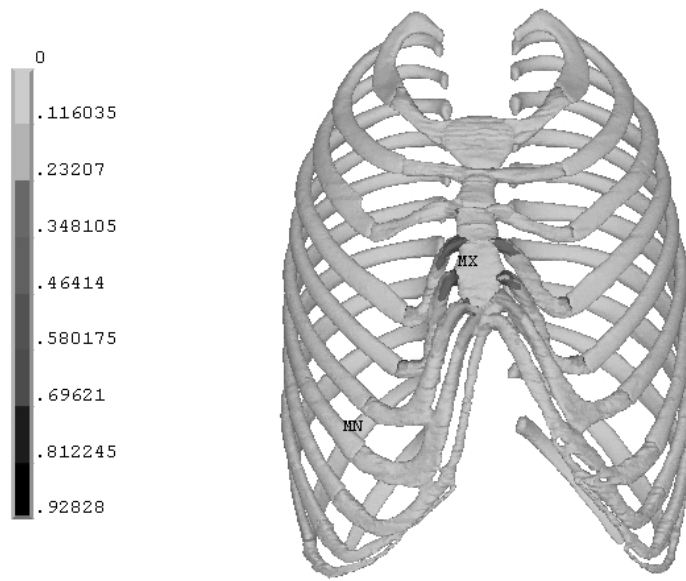
Fig. 6-17 Strain distribution of patient one with an elevating force 140N.
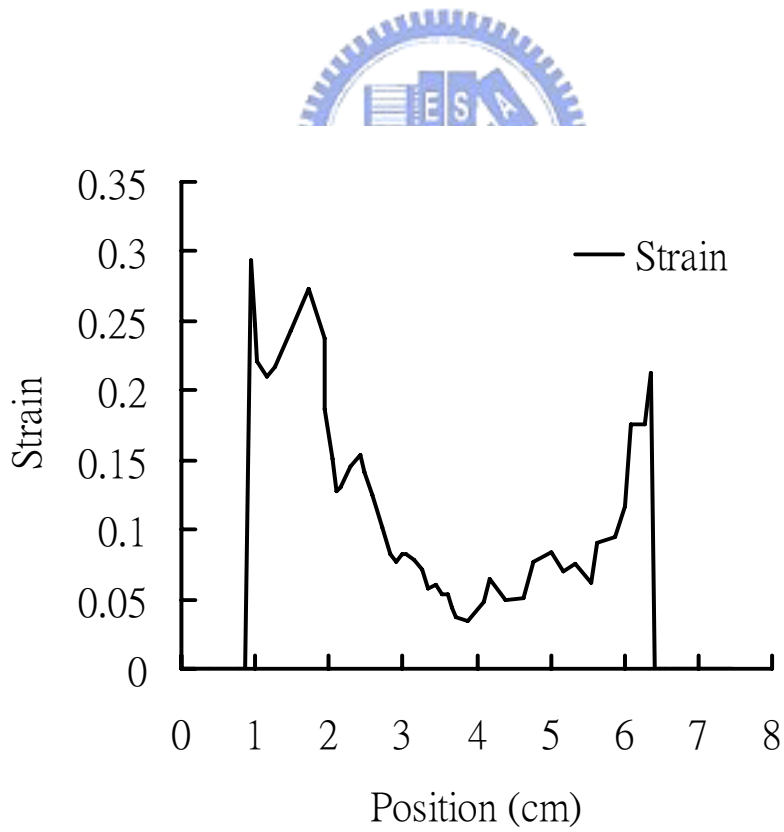
Fig. 6-18 Variation of strain of patient one along the right fifth costal cartilage
and rib with an elevating force 140N.

<div align="center">(a)   (b)</div>
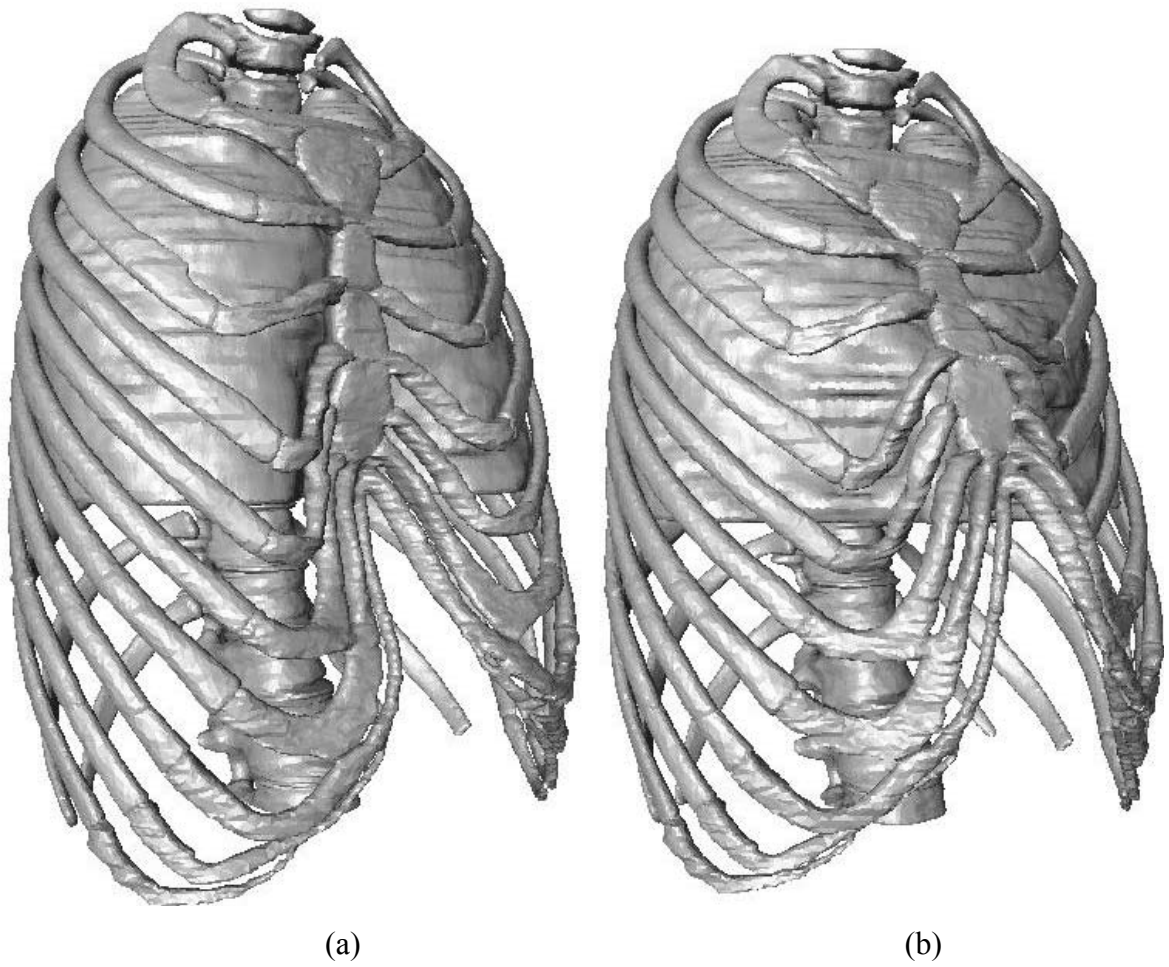
Fig. 6-19 Intrathoracic volume (a) original and (b) after Nuss procedure.
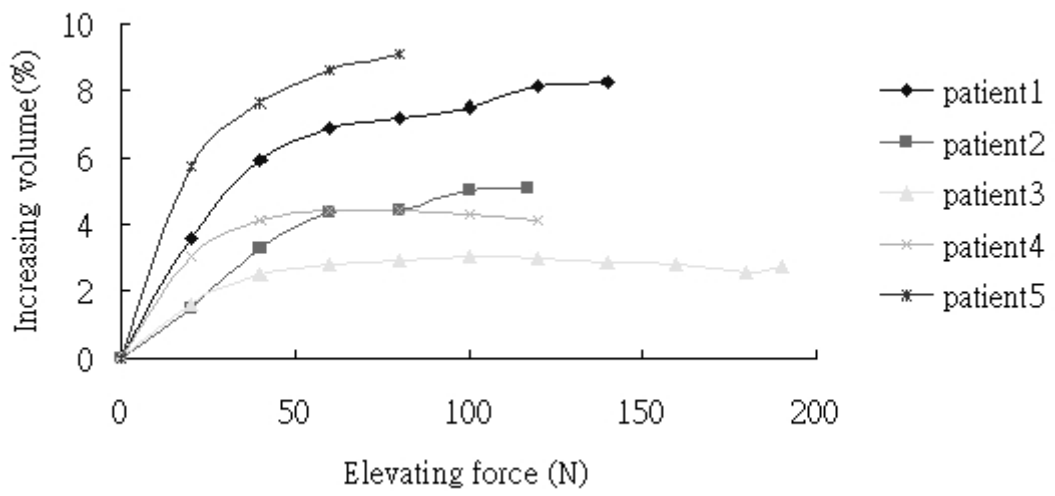
Fig. 6-20 The relationship between elevating force and the
increasing volume of intrathoracic.
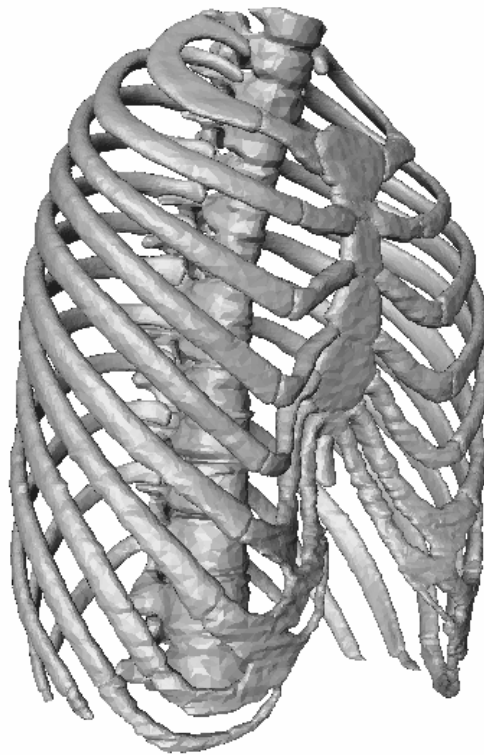
(a)
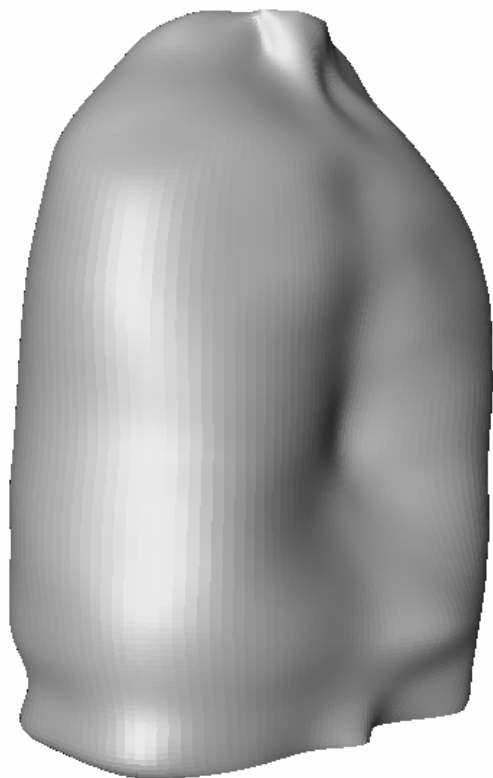
(b)
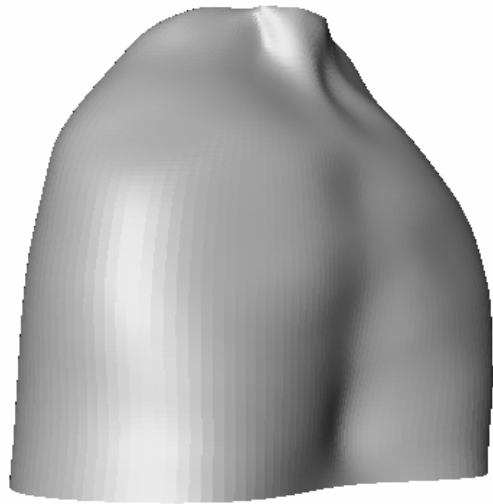
(c)

Fig. 6-21 (a) rib cage model of pre-operative PE patient (b) approximated surface
(c) thoracic volume measurement($1885.809cm^3$).

(a)

(b)

82

(c)
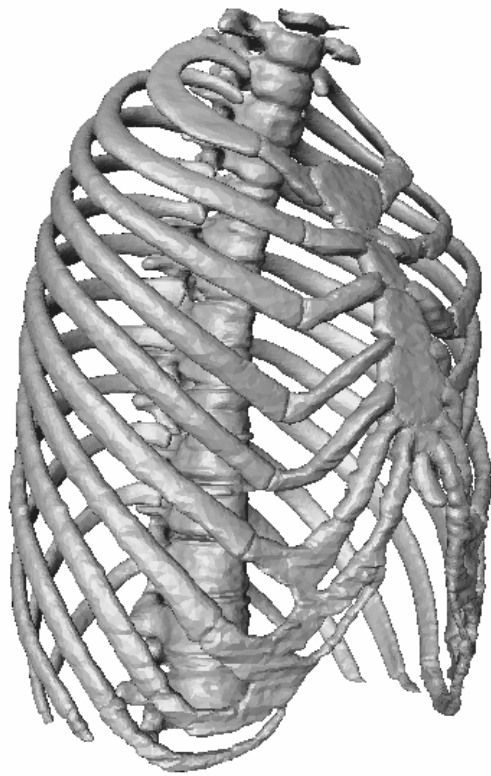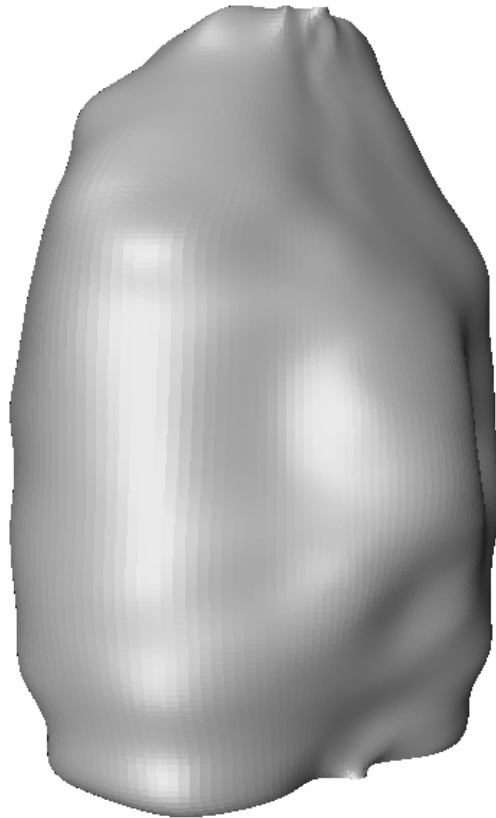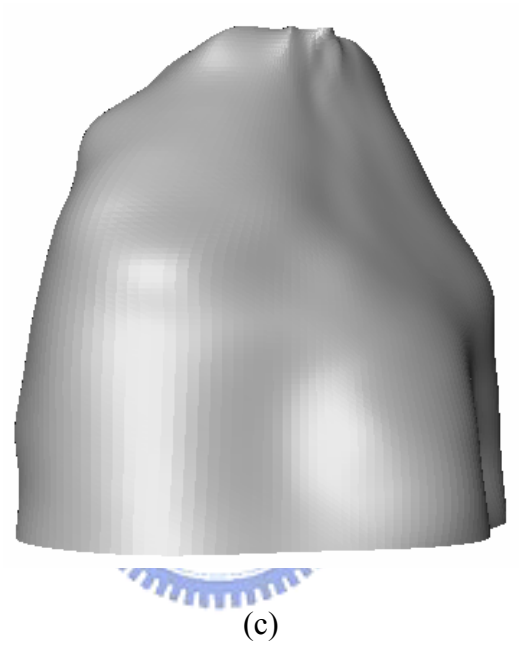
Fig. 6-22 (a) rib cage model of postoperative PE patient (b) approximated surface
(c) thoracic volume measurement($2129.294cm^3$).

Chapter 7 Conclusions

The purposes of this thesis are focused on the finite element biomechanical analysis, which contains surface mesh optimization and biomechanical analysis of Nuss pectus excavatum repair. We present an evolutionary procedure, which integrates the micro genetic algorithm and a C^1 surface function interpolation method, applied to surface meshing on a set of unorganized points. Original surface meshes are generated based on Delaunay triangulation or reduced from the original models. Quadrilateral meshes are generated via the conversion of the triangular meshes and elementarily modified by the mesh structure modification operators. A C^1 interpolation function is constructed using the primary local elements to ensure the surface geometrical feature is preserved. The meshes are then smoothed using the micro-genetic algorithm on the reconstructed high order surface elements. The procedure is then tested in complicated and large-scale point datasets. The results show that the procedure successfully achieves better surface meshing with mesh quality significantly enhanced for different kinds of practical applications.

Generally, the generation of surface mesh is based on a pre-defined surface function, either in parametric patches or in algebraic form. In this study, the given data of model is just a set of unorganized points. In this situation, the major problem of surface mesh generation is of the mesh smoothing. As mention above, the given points are first triangulated to form a triangular mesh and/or converted them into quadrilateral mesh, and then surface mesh smoothing procedure is applied to improve the mesh quality. A MGA mesh smoothing procedure is adopted in this study, which allows us to avoid the calculation of search direction and step size and to enable a global search for optimum. Furthermore, a C^1 surface function interpolation method is integrated into the MGA mesh smoothing procedure to ensure the geometrical accuracy of models during the surface mesh smoothing.

The extensions of the proposed method are to enhance the efficiency of MGA and the accuracy of the reconstructed surface functions. The MGA as one of the GA methods is by nature well suited to parallelization. Therefore, our further enhancement will be in performance issues of parallelism. The accuracy of the reconstructed local interpolation functions on surfaces determines the baseline of the accuracy of the entire model. Higher order interpolation methods can be further developed to serve the purpose.

For the biomechanical analysis of the pectus excavatum repair, the simulation results indicated the stress and strain distributions on the chest wall for PE patients after a Nuss

procedure. It is considerable that the generated stress may induce some complications. In Fig. 6-15, the anterior chest wall is a plane with 40N elevating force and the shape with 80N is similar to normal shape. However, the corrected displacement of this patient is 4.47 cm and the shape is like a pectus carinatum. We consider that it is over correction. Since the shape of the pectus bar was decided by surgeon based on personal experience and made in the surgery directly. The shape of pectus bar was made without any scientific computation and sometimes the corrected results do not fit the surgeon's expectation. Therefore, over or under correction is periodically occurred during the Nuss procedure. This thesis presents a procedure not only to estimate the distribution of stress and strain but also to predict the corrected shape of PE repair. The simulation results can be used to design an optimal shape of pectus bar for PE repairing.

For the measurement of lung volume, we present two thoracic volume measurement methods to estimate the lung volume changes of the pre- and post-operation PE patients. The presented methods are preliminary investigation to measure the intrathoracic volume and thoracic volume. The cause of the huge difference between the measured results is that the approximated surface does not fit the rib cage model very well. It need more modifications to improve the accuracy of the surface approximation procedure.

Moreover, this finite element biomechanical analysis of PE patients under a Nuss procedure was performed with many simplified assumptions, such as simplified rib cage model and the applied load of elevating and reaction forces. These assumptions may influence the accuracy of simulated results. The complexity of the interaction of the spine, the muscles, and the skin all should be considered to provide a more precise calculation. After perfecting the FEA model, we expect that our simulation will help to customize the Nuss procedure preoperatively, *i.e.*, by designing the optimal pectus bar shape that gives the best shape correction, while minimizing the stress and strain. The point of the best elevation for the pectus bar, and whether two bars should be chosen instead of one, can also be estimated preoperatively.

Reference

[1] Zannoni C., Mantovani R., Viceconti M., "Material properties assignment to finite element models of bone structures: a new method", Medical Engineering & Physics, 20(10), 735-740, 1998.

[2] Viceconti M., Davinelli M., Taddei F., Cappello A., "Automatic generation of accurate subject-specific bone finite element models to be used in clinical studies", Journal of Biomechanics, 37(10), 1597-1605, 2004.

[3] Chen D. P., Hsu Z. Y., Lin F. P., "Micro-genetic approach for surface meshing on a set of unorganized points", Computer Methods in Applied Mechanics and Engineering, 196, 1997-2008, 2007.

[4] Canann S. A., Liu Y. C., Mobley A. V., "Automatic 3D surface meshing to address today's industrial needs", Finite Elements in Analysis and Design, 25, 185-198, 1997.

[5] Okabe A., Boots B., Suqihara K., Spatial tessellations: concepts and applications of Voronoi diagrams, John Wiley & Sons, New York, 1992.

[6] George P. L., Automatic mesh generation, Application to finite element methods, John Wiley & Sons, New York, 1991.

[7] Weimer H., Warren J., "Fast approximating triangulation of large scattered datasets", Advances in Engineering Software, 30(6), 389-400, 1999.

[8] Zhao H. K., Osher S., Fedkiw R., "Fast surface reconstruction using the level set method", in: 1st IEEE Workshop on Variational and Level Set Methods, in conjunction with the 8th international Conference on Computer Vision (ICCV), (Vancouver, Canada) 194-202, 2001.

[9] Park H., Kim K., "Applications: An adaptive method for smooth surface approximation to scattered 3d points", Computer-Aided Design, 27, 929-939, 1995.

[10] Edelsbrunner H., Mücke E. P., "Three-dimensional Alpha Shapes", ACM

Transactions on Graphics, 13 (1), 43-72, 1994.

[11] Field D. A., "Laplacian smoothing and Delaunay triangulations", Communications and Applied Numerical Methods, 4, 709-712, 1988.

[12] Freitag L., "On combining Laplacian and optimization-based mesh smoothing techniques", AMD Trends in Unstructured Mesh Generation, ASME, 220, 37-43, 1997.

[13] Knupp P. M., "Achieving finite element mesh quality via optimization of the Jacobian matrix norm and associated quantities. Part I — a framework for surface mesh optimization", International journal for Numerical Methods in Engineering, 48, 401-420, 2000.

[14] Garimella R. V., Shashkov M. J., Knupp P. M., "Triangular and quadrilateral surface mesh quality optimization using local parametrization", Computer methods in applied mechanics and engineering, 193, 913-928,2004.

[15] Canann S. A., Tristano J. R., Staten M. L., "An approach to Combined Laplacian and Optimization-Based Smoothing for Triangular, Quadrilateral, and Quad-Dominant Meshes", Proceedings, 7th International Meshing Roundtable, 479-494, 1998.

[16] Arora J. S., Introduction to optimum design, McGraw-Hill Book Company, 1989.

[17] Krishnakumar K., "Micro-genetic algorithms for stationary and non-stationary function optimization", SPIE: Intelligent Control and Adaptive System, 289-296, Philadelphia, PA, 1989.

[18] Bedwani W. A., Ismail O. M., "Genetic optimization of variable structure PID control systems", ACS/IEEE International Conference on Computer Systems and Applications (AICCSA'01), Beirut, Lebanon, 27-30, June, 2001.

[19] Chen S., Wu Y., McLaughlin S., "Genetic algorithm optimization for blind channel identification with higher order cumulant fitting", IEEE transactions on evolutionary computation, 1 (4), 259-265, 1997.

[20] Chakravarty S., Mittra R., Fellow L., Williams N. R., "Application of a microgenetic

algorithm (MGA) to the design of broad-band microwave absorbers using multiple frequency selective surface screens buried in dielectrics", IEEE transactions on antennas and propagation, 50 (3), 284-296, 2002.

[21] Goldberg D. E., Genetic Algorithms in Search, Optimization and Machine Learning, Addison-Wesley Longman Publishing Co., Inc., Boston, MA, 1989.

[22] Gen M., Cheng R., Genetic algorithms and engineering optimization, New York: John Wiley & Sons, 2000.

[23] Goodman T. N. T., Said H. B., "A C^1 triangular interpolant suitable for scattered data interpolation", Communications in Applied Numerical Methods, 17, 479-485, 1991.

[24] Gordon V. S., Whitley D., "Serial and parallel genetic algorithms as function optimizers", Proceedings of the 5th International Conference on Genetic Algorithms (IGGA5), 177-183, 1993.

[25] Fonkalsrud E. W., "Current management of pectus excavatum", World Journal of Surgery, 27(5), 502–508, 2003.

[26] Molik K. A., Engum S. A., Rescorla F. J., West K. W., Scherer L. R. and Grosfeld J. L., "Pectus excavatum repair: Experience with standard and minimal invasive techniques", Journal of Pediatric Surgery, 36(2), 324-328, 2001.

[27] Länsman S., Serlo W., Linna O., Pohjonen T., Törmälä P., Waris T. and Ashammakhi N., 2002, "Treatment of pectus excavatum with bioabsorbable polylactide plates: Preliminary results", Journal of Pediatric Surgery, 37(9), 1281–1286, 2002.

[28] Haller J. A., Kramer S. S. and Lietman S. A., "Use of CT scans in selection of patients for pectus excavatum surgery: a preliminary report", Journal of Pediatric Surgery, 22, 904-906, 1987.

[29] Ravitch M. M., "The operative treatment of pectus excavatum", Annals of Surgery, 129(4), 429-444, 1949.

[30] Nuss D., Kelly R. E. Jr., Croitoru D. P. and Katz M. E., "A 10-year review of a minimally

invasive technique for the correction of pectus excavatum", <u>Journal of Pediatric Surgery</u>, 33(4), 545-552, 1998.

[31] Croitoru D. P., Kelly R. E., Goretsky M. J., Gustin T., Keever R. and Nuss D., "The minimally invasive Nuss technique for recurrent or failed pectus excavatum repair in 50 patients", <u>Journal of Pediatric Surgery</u>, 40(1), 181–187, 2005.

[32] Niedbala A., Adams M., Boswell W. C. and Considine J. M., "Acquired thoracic scoliosis following minimally invasive repair of pectus excavatum", <u>American Surgeon</u>, 69(6), 530–533, 2003.

[33] Park H. J., Lee S. Y., Lee C. S., Youm W. and Lee K. R., "The Nuss procedure for pectus excavatum: evolution of techniques and early results on 322 patients", <u>The Annals of Thoracic Surgery</u>, 77(1), 289–295, 2004.

[34] Croitoru D. P., Kelly R. E. Jr., Goretsky M. J., Lawson M. L., Swoveland B. and Nuss D., "Experience and modification update for the minimally invasive Nuss technique for pectus excavatum repair in 303 patients", <u>Journal of Pediatric Surgery</u>, 37(3), 437–445, 2002.

[35] Hebra A., Swoveland B., Egbert M., Tagge E. P., Georgeson K., Othersen H. B. Jr. and Nuss D., "Outcome analysis of minimally invasive repair of pectus excavatum: Review of 251 cases", <u>Journal of Pediatric Surgery</u>, 35(2), 252–258, 2000.

[36] Park H. J., Lee S. Y. and Lee C. S., "Complications associated with the Nuss procedure: analysis of risk factors and suggested measures for prevention of complications", <u>Journal of Pediatric Surgery</u>, 39(3), 391–395, 2004.

[37] Awrejcewicz J. and Łuczak B., "The finite element model of the human rib cage", <u>Journal of Theoretical and Applied Mechanics</u>, 45(1), 25-32, 2007.

[38] Fonkalsrud E. W. and Reemtsen B., "Force required to elevate the sternum of pectus excavatum patients", <u>Journal of the American College Surgeons</u>, 195(4), 575–577, 2002.

[39] Weber P. G., Huemmer H. P. and Reingruber B., "Forces to be overcome in correction of

pectus excavatum", <u>The Journal of Thoracic and Cardiovascular Surgery</u>, 132(6), 1369–1373, 2006.

[40] Perillo-Marcone A. and Taylor M., "Effect of varus/valgus malalignment on bone strains in the proximal tibia after TKR: an explicit finite element study", <u>Journal of Biomechanical Engineering</u>, 129(1), 1-11, 2007.

[41] Papini M., Zdero R., Schemitsch E. H. and Zalzal P., "The biomechanics of human femurs in axial and torsional loading: comparison of finite element analysis, human cadaveric femurs, and synthetic femurs", <u>Journal of Biomechanical Engineering</u>, 129(1), 12-19, 2007.

[42] Gréalou L., Aubin C. É. and Labelle H., "Rib cage surgery for the treatment of scoliosis: a biomechanical study of correction mechanisms", <u>Journal of Orthopaedic Research</u>, 20(5), 1121-1128, 2002.

[43] Holland J. H., <u>Adaptation in Natural and Artificial Systems: an introductory analysis with applications to biology, control, and artificial intelligence</u>, University of Michigan Press, Ann Arbor, 1990.

[44] Rahmat-Samii Y. and Michielssen E., <u>Electromagnetic Optimization by Genetic Algorithms</u>, Wiley, New York, 1999

[45] Lau T. S., Lo S. H. and Lee C. K., "Generation of quadrilateral mesh over analytical curved surfaces", <u>Finite Elements in Analysis and Design</u>, 27, 251-272, 1997.

[46] Whelan T., "A representation of a C^2 interpolant over triangles", <u>Computer Aided Geometric Design</u>, 3, 53-66, 1986.

[47] Sheffer A. and de Sturler E., "Surface parameterization for meshing by triangulation flattening", Proceedings, 9th International Meshing Roundtable, 161-172, 2000.

[48] Gotsman C., Gu X. and Sheffer A., "Fundamentals of spherical parameterization for 3D meshes", ACM Transactions on Graphics (Proc. SIGGRAPH 2003), 22(3), 358-363, 2003.

[49] Lee S., Wolberg G. and Shin S. Y., "Scattered data interpolation with multilevel B-splines", <u>IEEE Transactions on visualization and computer graphics</u>, 3 (3), 228-244, 1997.

[50] Costantini P. and Manni C., "A local shape-preserving interpolation scheme for scattered data", <u>Computer Aided Geometrical Design</u>, 16, 385-405, 1999.

[51] Lai M. J., "Convex preserving scattered data interpolation using bivariate C^1 cubic splines", <u>Journal of Computational and Applied Mathematics</u>, 119, 249-258, 2000.

[52] Goodman T. N. T., Said H. B. and Chang L. H. T., "Local derivative estimation for scattered data interpolation", <u>Applied mathematics and computation</u>, 68, 41-50, 1995.

[53] Canann S. A., Muthukrishnan S. N. and Phillips R. K., "Topological refinement procedures for triangular finite element meshes", <u>Engineering with Computers</u>, 12, 243-255, 1996.

[54] Cheng B. and Topping B. H. V., "Improved adaptive quadrilateral mesh generation using fission elements", <u>Advances in Engineering Software</u>, 29 (7-9), 733-744, 1998.

[55] Maza S., Noel F., Leon J. C., "Generation of quadrilateral meshes on free-form surfaces", <u>Computers and Structures</u>, 71, 505-524, 1999.

[56] Johnston B. P., Sullivan J. M., Kwasnik A., "Automatic conversion of triangular finite element meshes to quadrilateral elements", <u>International Journal for Numerical Methods in Engineering</u>, 31, 67-84, 1991.

[57] Canann S. A., Muthukrishnan S. N., Phillips R. K., "Topological improvement procedures for quadrilateral finite element meshes", <u>Engineering with Computers</u>, 14, 168-177, 1998.

[58] Kinney P., "CleanUp: improving quadrilateral finite element meshes", Proceedings, 6th International Meshing Roundtable, 437-447, 1997.

[59] Knupp P. M., "Algebraic mesh quality metrics for unstructured initial meshes", <u>Finite Elements in Analysis and Design</u>, 39, 217-241, 2003.

[60] Guy G., Medioni G., "Inference of surfaces, 3D curves, and junctions from sparse, noisy, 3D data", <u>IEEE Transactions on Pattern analysis and Machine Intelligence</u>, 19 (11), 1265-1277, 1997.

[61] Sheu D. L., et al, National Cheng Kung University Islanders 101, Technical Report, Department of Aeronautics and Astronautics, National Cheng Kung University, Taiwan ROC.

[62] Template Graphics Inc. (TGS)

[63] Polhemus FastSCAN Cobra, http://fastscan3d.com/download/samples/

[64] Private communication.

[65] Fonkalsrud E. W., DeUgarte D. and Choi E., "Repair of pectus excavatum and carinatum deformities in 116 adults", <u>Annals of Surgery</u>, 236(3), 304-314, 2002.

[66] Jacobs J. P., Quintessenza J. A., Morell V. O., Botero L. M., van Gelder H. M. and Tchervenkov C. I., "Minimally invasive endoscopic repair of pectus excavatum", <u>European Journal of Cardio-thoracic Surgery</u>, 21, 869-873, 2002.

[67] Schalamon J., Pokall S., Windhaber J. and Hoellwarth M. E., "Minimally invasive correction of pectus excavatum in adult patients", <u>The Journal of Thoracic and Cardiovascular Surgery</u>, 132(3), 524-529, 2006.

[68] Yang K. H. and Wang, K. H., "Finite element modeling of the human thorax", Presented at the second visible human project conference, Bethesda, Maryland, USA, October, 1998.

[69] Feng J., Hu T., Liu W., Zhang S., Tang Y., Chen R., Jiang X. and Wei F., "The biomechanical, morphologic, and histochemical properties of the costal cartilages in children with pectus excavatum", <u>Journal of Pediatric Surgery</u>, 36(12), 1770–1776, 2001.

[70] Mckinley M. and O'Loughlin V. D., <u>Human anatomy</u>, McGraw-Hill, New York, USA, 2006.

[71] A Review of the Universe - Structures, Evolutions, Observations, and Theories,

http://universe-review.ca/F10-multicell.htm

[72]Arge E., Daehlen M. and Tveito A., "Approximation of scattered data using smooth grid functions", Journal of Computational and Applied Mathematics, 59, 191-205, 1995.

[73]Besl P. J. and McKay N. D., "A method for registration of 3-D shapes", IEEE Transactions on Pattern Analysis and Machine Intelligence, 14, 239-256, 1992.

[74]Davydov O. and Zeilfelder F., "Scattered data fitting by direct extension of local polynomials to bivariate splines", Advances in Computational Mathematics, 21, 223-271, 2004.

[75]Mederos B., Velho L. and Figueiredo L. H., "Moving least squares multiresolution surface approximation", SIBGRAPI, 19-26, 2003.

[76]Ohtake Y., Belyaev A. and Seidel H.P., "3D scattered data interpolation and approximation with multilevel compactly supported RBFs", Graphical Models, 67, 150-165, 2005.

[77]Pereyra V. and Scherer G., "Least squares scattered data fitting by truncated SVDs", Applied Numerical Mathematics, 40, 73-86, 2002.

[78]Fasshauer G. E. and Schumaker L. L., "Minimal energy surfaces using parametric splines", Computer Aided Geometric Design, 13, 45-79, 1996.

[79]Lai M. J., "Scattered data interpolation and approximation using bivariate C^1 piecewise cubic polynomials", Computer Aided Geometric Design, 13, 81-88, 1996.

[80]Pottmann H., Huang Q. X., Yang Y. L. and Hu, S. M., "Geometry and convergence analysis of algorithms for registration of 3D shapes", International Journal of Computer Vision, 67, 277-296, 2006.

[81]Faux I. D. and Pratt M. J., Computational geometry for design and manufacture, John Wiley & Sons, New York, 1979.

[82]Faires J. D. and Burden R. L., Numerical methods, PWS Publishing Company, Boston, 1993.

[83] Inge T. H., Owings E., Blewett C. J., Baldwin C. E., Cain W. S., Hardin W. and Georgeson K. E., "Reduced hospitalization cost for patients with pectus excavatum treated using minimally invasive surgery", Surgical Endoscopy, 17(10), 1609-1613, 2003.

[84] Shigley J. E. and Mischke C. R., Mechanical engineering design, McGraw-Hill, New York, USA, 2001.

Publication List

A. Journal Paper

1. Chen D. P., <u>Hsu Z. Y.</u>, Lin F. P., "Micro-genetic approach for surface meshing on a set of unorganized points", *Computer Methods in Applied Mechanics and Engineering*, 196, 1997-2008, 2007.

2. Chang P. Y., <u>Hsu Z. Y.</u>, Chen D. P., Lai J. Y. and Wang C. J., "The stress and strain generation on thoracic cage of pectus excavatum patients after Nuss procedure-a finite element analysis model", *Clinical biomechanics*, 2007. (**Revised**)

3. Chen D. P., <u>Hsu Z. Y.</u> and Chang P. Y., "An enveloping surface for thoracic volume evaluation", *Computer Aided Geometric Design*, 2007. (**Submitted**)

B. Conference Paper

1. Chang P. Y., <u>Hsu Z. Y.</u>, Chen D. P., Lai J. Y. and Wang C. J., "A biomechanical study on pectus excavatum after the Nuss procedure", *PAPS 40ᵗʰ Annual Meeting - AAPS Annual Scientific Meeting*, Queenstown, New Zealand, 15-19 April, 2007.

2. Chang P. Y., <u>Hsu Z. Y.</u>, Chen D. P., Lai J. Y. and Wang C. J., "Finite element analysis of thoracic cage changes on pectus excavatum patient after Nuss procedure", *The American Academy of Pediatrics (AAP) 2007 National Conference & Exhibition,* San Francisco, USA, 27-30 October, 2007.

C. Patent

1. 廖俊仁, <u>徐華均</u>, 許克群, 陳大潘, 林玟嬌, ”組織切碎裝置”, 中華民國專利證書, 發明第I255738號, 公告日期：2006/06/01.